

DOT/FAA/TC-21/22

Federal Aviation Administration
William J. Hughes Technical Center
Aviation Research Division
Atlantic City International Airport
New Jersey 08405

Progressive Damage Growth of Composites under Variable- Amplitude Fatigue Testing

November 2024

Final report



U.S. Department of Transportation
Federal Aviation Administration

NOTICE

This document is disseminated under the sponsorship of the U.S. Department of Transportation in the interest of information exchange. The U.S. Government assumes no liability for the contents or use thereof. The U.S. Government does not endorse products or manufacturers. Trade or manufacturers' names appear herein solely because they are considered essential to the objective of this report. The findings and conclusions in this report are those of the author(s) and do not necessarily represent the views of the funding agency. This document does not constitute FAA policy. Consult the FAA sponsoring organization listed on the Technical Documentation page as to its use.

This report is available at the Federal Aviation Administration William J. Hughes Technical Center's Full-Text Technical Reports page: actlibrary.tc.faa.gov in Adobe Acrobat portable document format (PDF).

Form DOT F 1700.7 (8-72)

Reproduction of completed page authorized

1. Report No. DOT/FAA/TC-21/22	2. Government Accession No.	3. Recipient's Catalog No.	
4. Title and Subtitle Progressive Damage Growth of Composites under Variable-Amplitude Fatigue		5. Report Date April 2022	
		6. Performing Organization Code	
7. Author(s) Waruna Seneviratne, John Tomblin, Supun Kariyawasam, and Vishnu Saseendran		8. Performing Organization Report No.	
9. Performing Organization Name and Address National Institute for Aviation Research (NIAR) Wichita State University 1845 Fairmount, Wichita, KS 67260-0093		10. Work Unit No. (TRAIS)	
		11. Contract or Grant No.	
12. Sponsoring Agency Name and Address U.S Department of Transportation, Federal Aviation Administration (FAA) Air Traffic Organization NextGen & Operations Planning Office of Research and Technology Development, Washington, DC 20591		13. Type of Report and Period Covered Final Report	
		14. Sponsoring Agency Code	
15. Supplementary Notes The Federal Aviation Administration William J. Hughes Technical Center Research Division COR was Lynn Pham.			
16. Abstract Anisotropic heterogeneous characteristics and changes in failure modes over the fatigue life as well as multiple failure mechanisms that interact with each other make it challenging to predict damage growth in composite structures. Therefore, overly conservative assumptions (e.g. load and life factors based on lower-level building block testing) are made for fatigue life assessment without taking full advantage of the fatigue capabilities of composites. To design efficient composite structures, a greater understanding of the fundamentals of fatigue damage initiation and growth characteristics is needed. A significant body of work on monotonic fatigue loading has been performed, and significant milestones in predicting the damage extent of specific failure modes, such as transverse cracking in cross-ply laminates and delamination, have been reached. The interaction of matrix cracking and delamination under monotonic fatigue loading has also been addressed. First, damage accumulation based on constant-amplitude (monotonic) fatigue was studied in detail with high-fidelity inspection methods. Then, several block-spectrum configurations, sequencing various high-, medium-, and low-load blocks were investigated for determining the sequencing effects. These block spectra included cases with a constant stress ratio across the spectrum as well as cases with variable stress ratios. Several key findings concerning damage initiation progression are reported for several combinations of block spectra. For the open-hole specimen configuration, it was noted that a high load at the beginning resulted in the least damaging scenario. Supplementary studies on load-sequencing effects by altering laminate configurations, varying stress levels, and mixed stress ratio are also included.			
17. Key Words Fatigue; Spectrum; Sequencing; Damage; Open Hole; Load Block; Stress-Ratio		18. Distribution Statement This document is available to the U.S. public through the National Technical Information Service (NTIS), Springfield, Virginia 22161. This document is also available from the Federal Aviation Administration William J. Hughes Technical Center at actlibrary.tc.faa.gov .	
19. Security Classif. (of this report) Unclassified	20. Security Classif. (of this page) Unclassified	21. No. of Pages 141	22. Price

Contents

1	Introduction.....	1
1.1	Background and overview	5
1.2	Research objective	6
2	Experimental procedures	7
2.1	Materials and methods	7
2.1.1	Specimen design and fabrication	8
2.1.2	Test matrix	9
2.1.3	Open-hole static and fatigue testing.....	10
2.2	Fatigue load spectra for load sequencing.....	11
3	Results and discussion	14
3.1	Constant amplitude fatigue damage characterization	14
3.1.1	Tension-tension fatigue ($R = 0.1$)	16
3.1.2	Compression-compression fatigue ($R = 5$)	23
3.1.3	Fully reversed fatigue ($R = -1$).....	28
3.1.4	Influence of tensile fatigue on residual strength	36
3.2	Sequencing effects—spectrum fatigue damage characterization	43
3.2.1	Effect of 24-ply laminate configuration UNI-QI	43
3.3	Supplementary studies on sequencing effects.....	61
3.3.1	Effect of 16-ply laminate configuration PW-QI	62
3.3.2	Effect of stress levels: constant R-ratio spectra	68
3.3.3	Effect of stress levels: variable R-ratio spectra.....	75
3.3.4	Evaluation of service loads	81
4	Conclusions and outlook	82
4.1	Pilot study on compression after impact coupons.....	83
4.2	Recommendations.....	85
5	References.....	87

A	High-fidelity X-CT summary of constant amplitude Fatigue testing	A-1
B	Fatigue and high-fidelity X-CT summary of spectrum fatigue profiles	B-1
C	High-fidelity X-CT summary of constant and variable R-ratio spectra.....	C-1

Figures

Figure 1. Material overview in Boeing 787 Dreamliner.....	1
Figure 2. Building block schematic of certification process (Wanhill, 2017)	2
Figure 3. Development of block spectrums: random spectrum (a), block spectrum (b), and within one block (c)	4
Figure 4. Progressive damage growth of 24-Ply IM7/5320-1 QI OH specimen ($R = 0.1$ at one million cycles).....	4
Figure 5. Effect of load sequencing on damage mechanics illustrated by initial low-medium-high- (left) and high-low-medium- (right) load occurrences	6
Figure 6. OH specimen dimensions and tolerances	9
Figure 7. OH test setups.....	11
Figure 8. X-DR scans of 24-Ply UNI-QI OH specimen showing characteristic damage modes (55% SL, $R = -1$ at 325,000 cycles)	15
Figure 9. Delamination between plies and 45° fiber splitting of OHF specimen ($R = 0.1$ at one million cycles).....	17
Figure 10. Examples of Fiber Splitting (matrix cracks) in various ply orientations.....	19
Figure 11. Cross-sectional (thickness direction) views of X-CT of OHF specimen ($R = 0.1$ at 25,000 to one million cycles).....	20
Figure 12. 0° Ply #6 and 90° Ply #21 of UNI-QI CA (90% SL, $R = 0.1$ at one million cycles) ..	21
Figure 13. Apparent Stiffness degradation of UNI-QI CA (90% SL, $R = 0.1$); damage in critical plies for Specimen #21.....	22
Figure 14. Predominant micro-buckling modes in compression	23
Figure 15. Kink band with kink orientations (α , β) and boundaries	24
Figure 16. (a) Schematic illustration of kink band and (b) X-CT of fatigue specimen ($R = 5$)....	25
Figure 17. Fiber breaks and splitting of OHF specimen ($R = 5$ at 45,000 cycles)	25
Figure 18. Stiffness degradation in UNI-QI CA specimen (75% SL, $R = 5$); damage accumulation in critical plies for Specimen #8.....	26
Figure 19. CA tension vs. compression failure mechanisms in each ply of UNI-QI ($R = 0.1$ and $R = 5$ at one million cycles).....	27
Figure 20. Fiber breaks and splitting on outer 45° ply and delamination at CA of OHF specimen ($R = -1$)	28
Figure 21. Primary failure modes detected during constant amplitude (55% SL, $R = -1$).....	31
Figure 22. Failure mechanism in each ply of CA UNI-QI Specimen #17 (55% SL, $R = -1$ at 250,000 and 730,000 cycles)	32

Figure 23. Stiffness degradation damage progression in multiple plies of CA OHF UNI-QI Specimen #8 (55% SL, $R = -1$)	33
Figure 24. Static notch sensitivity in composites.....	36
Figure 25. SN data for T650/5320-1 24-Ply UNI-QI OH ($R = 0.1$)	38
Figure 26. SN plot with tension/compression residual strength for IM7/5250-4 28-ply hard layup ($R = 0.1$).....	40
Figure 27. Schematic illustration of increase in residual strength due to localized reduction in stress concentration from fatigue exposure.....	41
Figure 28. Fatigue spectrum for Profile #3 (<i>low-medium-high-medium-low</i>)	45
Figure 29. X-CT images showing damage progression in selected plies at end of each load block for spectrum Profile #3	47
Figure 30. Stiffness degradation vs. number of cycles for UNI-QI OH spectrum Profile #3 with damage progression in multiple plies ($R = -1$).....	48
Figure 31. TTU C-Scan and thermal images for 24-Ply UNI-QI OH at end of each load block for spectrum Profile #3	49
Figure 32. Fatigue spectrum for Profile #5 (<i>high-low-medium-low-medium</i>)	50
Figure 33. X-CT images showing damage progression in selected plies at end of each load block for spectrum Profile #5	52
Figure 34. Stiffness degradation vs. number of cycles for UNI-QI OH spectrum Profile #5 with damage progression in multiple plies ($R = -1$).....	53
Figure 35. TTU C-Scan and thermal images for 24-Ply UNI-QI OH at end of each load block for spectrum Profile #5	54
Figure 36. Fatigue spectrum for Profile #6 (<i>low-medium-low-medium-high</i>)	55
Figure 37. X-CT images showing damage progression in selected plies at end of each load block for spectrum Profile #6	56
Figure 38. Stiffness degradation vs. number of cycles for UNI-QI OH spectrum Profile #6 with damage progression in multiple plies ($R = -1$).....	57
Figure 39. TTU C-Scan and thermal images for 24-Ply UNI-QI OH at end of each load block for spectrum Profile #6	58
Figure 40. TTU C-Scan and thermal images for 16-Ply PW-QI OH at end of each load block for spectrum Profile #5-A.....	64
Figure 41. TTU C-Scan and thermal images for 16-Ply PW-QI OH at end of each load block for spectrum Profile #6-A.....	64
Figure 42. Stiffness degradation vs. number of cycles for spectrum Profile #5-A with DIC and C-Scan for 16-Ply PW-QI OH ($R = -1$)	66

Figure 43. Stiffness degradation vs. number of cycles for spectrum Profile #6-A with DIC and C-Scan for 16-Ply PW-QI OH ($R = -1$)	67
Figure 44. Fatigue spectrum profiles for load-sequencing effects under varying stress levels for constant R-ratio	70
Figure 45. Stiffness degradation vs. number of cycles for UNI-QI OH with damage progression in critical plies ($R = 5$ spectrum)	72
Figure 46. Stiffness degradation vs. number of cycles for UNI-QI OH with damage progression in critical plies ($R = -1$ spectrum)	73
Figure 47. Critical damage mechanisms at the end of each load block for 24-Ply UNI-QI OH (constant R-Ratio spectra)	74
Figure 48. Fatigue spectrum profiles for load-sequencing effects under varying R-ratios	76
Figure 49. Stiffness degradation vs. number of cycles for UNI-QI OH with damage progression in critical plies ($R = 5$ and -1 spectra)	78
Figure 50. Stiffness degradation vs. number of cycles for UNI-QI OH with damage progression in critical plies ($R = -1$ and 5 spectra)	79
Figure 51. Critical damage mechanisms at the end of each load block for 24-Ply UNI-QI OH (variable R-Ratio spectra)	80
Figure 52. Damage growth in composites at realistic stress levels	81
Figure 53. TTU C-Scan images for 16-Ply PW-QI CAI at the end of each load block for spectrum Profile #5-B	84
Figure 54. TTU C-Scan images for 16-Ply PW-QI CAI at the end of each load block for spectrum Profile #6-A	85

Tables

Table 1. Laminate configurations	7
Table 2. OH test methods.....	8
Table 3. UNI-QI OH (24-Ply) Test matrix	10
Table 4. Block spectra used to investigate Sequencing Effects on UNI-QI OH specimens.....	13
Table 5. Dominant failure mechanisms in CA fatigue tests ($R = 0.1$, 5, and -1)	34
Table 6. Fatigue summary with tension/compression residual strength for IM7/5250-4 28-ply hard layup ($R = 0.1$)	39
Table 7. Increase in strength after one million cycles for IM7/5250-4 28-Ply Hard layup.....	39
Table 8. Fatigue profiles for sequencing study for 24-Ply UNI-QI OH ($R = -1$)	44
Table 9. Summary of damage initiation and final damage state in critical plies for Profiles #3, #5, and #6.....	60
Table 10. UNI-QI (24-Ply) OH test matrix.....	61
Table 11. PW-QI (16-Ply) OH test matrix.....	61
Table 12. Profiles of sequencing study for 16-Ply PW-QI OH ($R = -1$).....	62
Table 13. Fatigue profiles for sequencing study of 24-Ply UNI-QI OH with varying SL for compression and fully reversed cases	68
Table 14. Fatigue profiles for sequencing study for 24-Ply UNI-QI OH with varying R-ratios..	75

Acronyms

Acronym	Definition
ACEE	Aircraft Energy Efficiency
ACT	Advanced Composites Technology
ASTM	American Society for Testing and Materials
BVID	Barely visible impact damage
CA	Constant amplitude
CAI	Compression after impact
CFRP	Carbon fiber-reinforced polymer
DARPA	Defense Advanced Research Projects Agency
DIC	Digital image correlation
DLL	Design limit load
FAA	Federal Aviation Administration
GA	General aviation
HSR	High-Speed Research
IR	Infrared
LB	Load block
LVDT	Linear variable displacement transducer
MRCC	Manufacturer-recommended cure cycle
MTS	MTS Systems Corporation
NASA	National Aeronautics and Space Administration
NDI	Non-destructive inspection
NIAR	National Institute for Aviation Research
OH	Open hole
OHC	Open-hole compression
OHF	Open-hole fatigue
OHT	Open-hole tension
OoA	Out-of-autoclave
PW	Plain-weave (fabric)
QI	Quasi-isotropic
R	Stress-ratio
RS	Residual strength
SATS	Small Aircraft Transportation System
SD	Stiffness degradation

SL	Stress level
SN	Stress to number of cycles
ST	Strength-tracking
TTU	Through-transmission ultrasonic
UNI	Unidirectional tape
VA	Variable amplitude
WSU	Wichita State University
X-CT	X-ray computed tomography
X-DR	X-ray digital radiography

Executive summary

A lack of a clear understanding of damage growth mechanics under the influence of load sequencing makes the certification process of composite structures challenging and costly. Low-, medium-, and high-stress profiles, when stacked together in their likelihood of occurrence, lead to different damage initiation and progression scenarios. In this research, efforts were made to perform damage characterization under variable-amplitude (VA) fatigue loading. Two material configurations were chosen and then fatigued with three unique fatigue profiles comprised of altering the occurrence of low-, medium-, and high-stress levels (SLs). The identified critical damage initiation modes and final damage states indicate the influence of load-sequencing effects. For open-hole (OH) tests, a high load block (LB) at the beginning of the spectrum was found not to cause significant damage growth, in contrast to having the high LB in the middle or at the end. This may be attributed to the creation of damage such as isolated weak fiber breaks that are not easily detectable and microcracks reducing the stress concentration near the hole. Constant-amplitude (CA) fatigue testing on tension, compression, and fully reversed load scenarios were carried out, and the prominent failure mechanisms were thoroughly documented. These findings were then used to characterize the observed failure mechanisms under VA fatigue-loading scenarios. Supplementary studies on load-sequencing effects by altering the SLs and employing mixed stress-ratio (R-ratio) fatigue profiles were also conducted. In addition, the effect of a laminate configuration was also investigated. Damage growth in composites under VA loading was investigated by employing an OH specimen. In addition, a pilot study on compression after impact (CAI) specimens was also conducted to extend the load-sequencing study and to showcase the need to comprehend such damage characteristics during an impact event.

1 Introduction

During the past few decades, advanced composites have emerged as the structural materials of choice for many aerospace applications because of their superior specific strength and stiffness properties. Over the past 40 years, general aviation (GA) and the Small Aircraft Transportation System (SATS) of the National Aeronautics and Space Administration (NASA) have steadily increased the number of applications of advanced composite materials in primary and secondary airframe structures for that product type. Some notable programs of NASA which aided in early adoption of composite materials to GA include Aircraft Energy Efficiency (ACEE), Advanced Composites Technology (ACT), and High-Speed Research (HSR) programs. Through rigorous analysis and testing, these programs developed technology readiness for transport aircraft (subsonic and supersonic) and were successful in deploying composite structures in general aviation (GA) structures. The Defense Advanced Research Projects Agency (DARPA)-led programs also had impact of the development of advanced structural fibers and manufacturing.

Advanced composite materials have revolutionized the commercial aviation industry; a prime example is the Boeing 787 Dreamliner, which is comprised of more than 50% composite materials; see Figure 1 (Aly, 2017). The primary motive for employing composite materials is driven by the demand for higher fuel efficiency. Lower weight, higher stiffness, higher strength, fatigue durability, and corrosion resistance capabilities of composite materials have made them a better candidate than conventional metals.

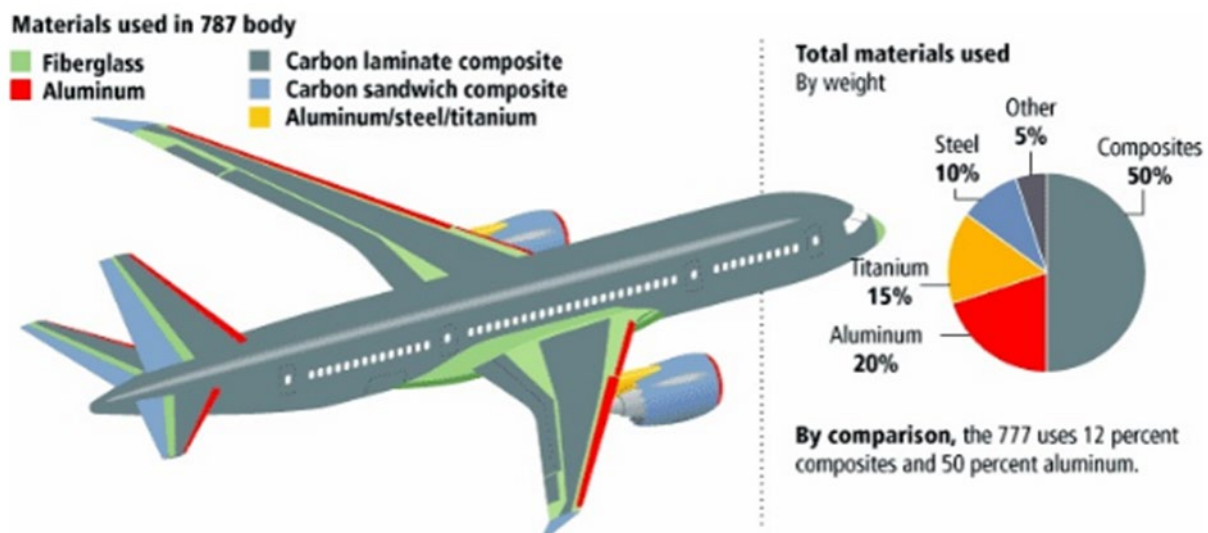


Figure 1. Material overview in Boeing 787 Dreamliner

In the aviation industry, it is a common challenge to design aircraft structures to withstand fatigue loading for both conventional metals and composites. Damage tolerance procedures are well established for metallic airframes, and there exist standard methods for structural analysis and inspection techniques. In addition, supporting databases are widely available to detect damage, forecast crack growth, and predict residual strength (RS). For metallic structures, damage growth under spectrum loading (realistic loading—variable-amplitude (VA) fatigue with multiple stress ratios) is commonly approximated using the Palmgren-Miner's rule (Miner, 1945; Palmgren, 1924). Damage growth mechanics and load spectrums for composite structures are significantly different compared to their metallic counterparts which make the certification of composite-metal hybrid structures challenging, expensive, and time-consuming. The stress ratio (commonly referred to as R-ratio) is a key term in fatigue discussions and is defined as the minimum applied stress over the maximum applied stress during cyclic loading.

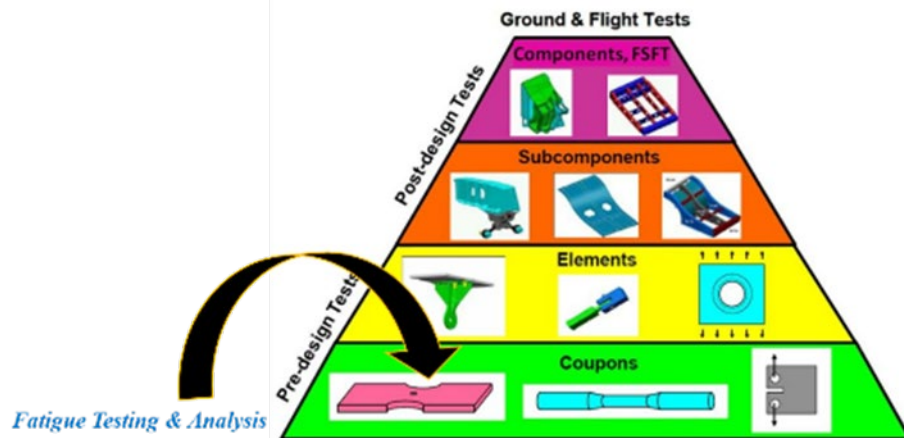


Figure 2. Building block schematic of certification process (Wanhill, 2017)

Current fatigue-life assessment techniques for composite structures are based on empirical or semi-empirical data. It is common for composite materials to have high data scatter in static and fatigue studies due to batch variability, process variability, and environmental effects. Previous research (Tomblin & Seneviratne, 2011) utilized individual Weibull, joint Weibull, and Sendecyk equivalent static strength (wearout) analysis (Sendecyk, 1981) techniques to compare the data scatter (reliability) of constant-amplitude (CA) fatigue data (SN curves) for various failure modes (Halpin, Jerina, & Johnson, 1973). It is evident in the literature that the most common technique to characterize fatigue behavior of composites is with the aid of SN curves.

In lower levels of the building block certification process, as shown in Figure 2 (Wanhill, 2017), generally, fatigue-life assessments rely on CA fatigue data or SN data (Whitehead, Kan,

Cordero, & Saether, 1986). SN curves represent the number of cycles to failure (on a log scale) with respect to CA cyclic stress levels (SLs), along with the initial static strength, runouts, and residual strength data. Although most fatigue-life assessment studies are established around CA fatigue data, it is very rare to experience only this type of fatigue loading in real-life applications. Therefore, fatigue-life assessment methodologies tend to use an overly conservative assumption for evaluating fatigue life under realistic VA or spectrum loading. It must also be noted here that the failure strength invariably depends on the specimen size (volume averaged strengths). In particular, for laminated composites, as damage tends to initiate from defects or other weak points in the material, the failure strength is governed by the coupon size; hence, scaling effects are pertinent in understanding failure mechanisms. Furthermore, from a pragmatic point of view, understanding scaling effects will enable in correctly interpreting results of scaled model tests, as material strength values employed in common design analysis are normally performed on small specimens. The scaling effects depends on failure mechanisms: fiber failure in tensile and compressive loading and matrix-dominated failure, with matrix failure showing the largest effect (Wisnom, 1999).

Several composite aircraft structures are reaching the twilight of their design lifetime. In the case of most military applications, life-extension efforts are underway. These applications provide an opportunity to assess the conservatism built into the original design criteria and to evaluate how well the composite structures withstand operational loads and environmental conditions. Thus, there is a need for fatigue assessments involving VA fatigue loading to understand the underlying damage mechanisms. In order to simplify flight spectrum loads, similar loadings can be grouped (blocked) together, and multiple CA fatigue blocks referred to as block-loading spectrum can be performed; see Figure 3 (Seneviratne & Tomblin, 2017). In this program, the block-loading method was adopted to investigate the influence of VA fatigue on the fatigue life of composite structures. Block loading will be referred to as VA fatigue loading or spectrum loading throughout this report.

Due to the inherent differences between composites and metals in terms of critical damage modes, there is a need to fully understand the damage-growth mechanics in composite materials. More importantly, the damage accumulation and growth in composites need to be fully characterized to aid in certification as well as establishing damage tolerance testing and analysis protocols. Progressive damage growth of a quasi-isotropic (QI) carbon fiber-reinforced polymer (CFRP) composite open-hole (OH) specimen under tension fatigue loading is shown in Figure 4 (Seneviratne & Tomblin, 2021), wherein detailed damage accumulation observed over one million cycles is reported for a selected few plies. Clearly evident is the complexity of damage

accumulation at each ply, as well as the interaction of multiple failure modes that require a detailed investigation, especially for specimens under VA fatigue loading.

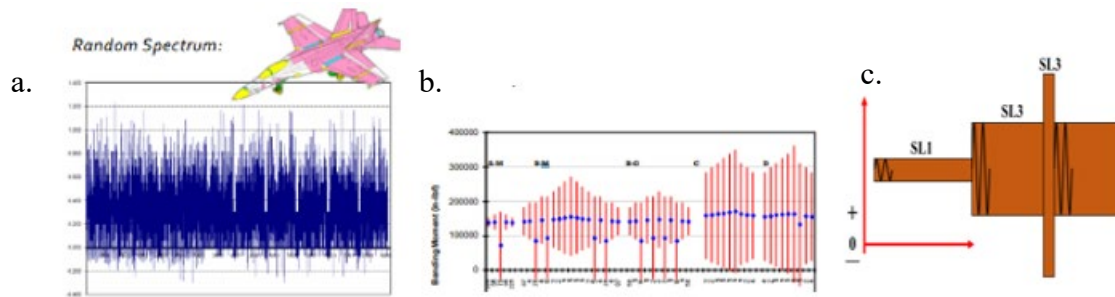


Figure 3. Development of block spectra: random spectrum (a), block spectrum (b), and within one block (c)

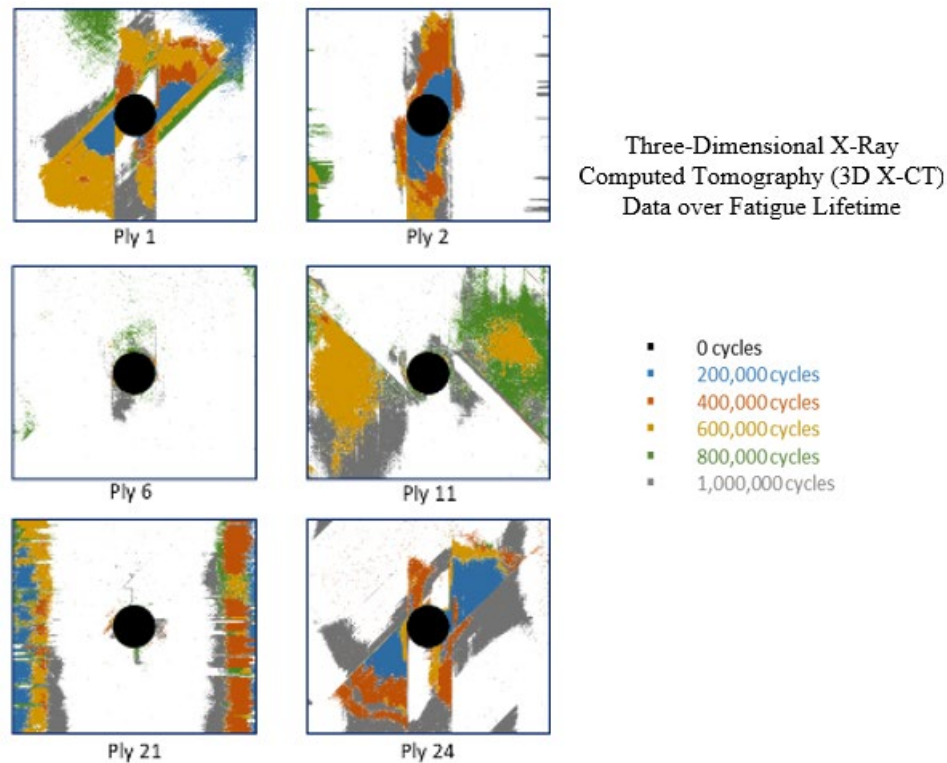


Figure 4. Progressive damage growth of 24-Ply IM7/5320-1 QI OH specimen ($R = 0.1$ at one million cycles)

1.1 Background and overview

Due to the anisotropic and heterogeneous nature of composites, the fatigue damage-growth characteristics of composites are complex. In addition, multiple failure mechanisms that interact with each other make it challenging to predict damage growth in composite structures.

Therefore, in current aviation applications, overly conservative assumptions are employed during fatigue-life assessment, which does not take full advantage of the superior fatigue capabilities of composites. This leads to heavier aviation structures. In a block spectrum, varying constant-amplitude fatigue stress profiles are combined according to a specific sequence. The damage accumulation differs within each block and depends on the SL, stress ratio, and damage state at the beginning of each block. In some instances, load sequencing also influences the damage growth under spectrum loading. The progressive damage accumulation is investigated by performing several block-loading spectra comprised of high, medium, and low SLs arranged in different sequences. Such differences in damage accumulation based on the arrangement of load levels in spectrum loading are commonly referred to as *load-sequencing effects*. The load spectrum of a typical flight mission includes taxi-climb-cruise-approach-taxi or ground-air-ground cycles, as well as various maneuvers and gust loads. Note that a realistic flight spectrum includes several complex block spectra with varying R-ratios and SLs. However, for this study, simple block spectra were used.

In the literature, for simplicity, the load-sequencing effect is typically investigated using block-loading experiments. Additionally, damage mechanics in composites due to high-low and low-high load sequencing in the literature lead to mixed conclusions, which are briefly discussed here. In cross-ply specimens, Broutman and Sahu (1972) reported that a low-high loading condition yielded more damage accumulation than a high-low loading sequence. Similarly, Bartley-Cho et al. (1998) performed both high-low and low-high block-spectra fatigue experiments on a QI laminate and found that a low-high loading sequence imparts more damage than a high-low sequence. On the other hand, Han and Hamdi (1983) observed that low-high load-sequencing tests led to less damage accumulation than the high-low block-spectrum tension fatigue tests in glass fiber composites. Gamstedt and Sjögren (2002) also made similar observations on a cross-ply carbon/epoxy material system and found that high-low amplitude block spectrums result in shorter lifetimes than a low-high sequence order.

Due to the variety of structural details, materials, layups, and other variables, damage mechanisms associated with sequencing effects presented in the literature are strongly divided. Hence, it is tedious to standardize findings from various studies in the literature. However, it is crucial to understand the effect of load sequencing on damage mechanics. Fatigue life, damage

initiation, and damage progression rates are highly influenced by the high- and low-load sequence of occurrence (sequencing effects).

1.2 Research objective

Fatigue life and damage accumulation of composite structures are governed by the sequence of variable-amplitude load occurrence, also known as the sequencing effect. As discussed previously, a clear understanding of load-sequencing effects on the fatigue life of composite materials is lacking. In most of the reported studies, only high-low and low-high sequences were evaluated. Some of the literature indicates that high-low specimens survive longer, while other studies conclude otherwise. Hence, it is difficult to standardize findings from the literature and arrive at a clear conclusion on the effects that load sequencing has on damage mechanics. A lack of clear understanding on damage-growth mechanics under the influence of load sequencing makes the certification process of composite structures challenging and costly. Low-, medium-, and high-stress profiles when stacked together in their likelihood of occurrence lead to different damage initiation and progression scenarios. A schematic illustration of this challenge is shown in Figure 5.

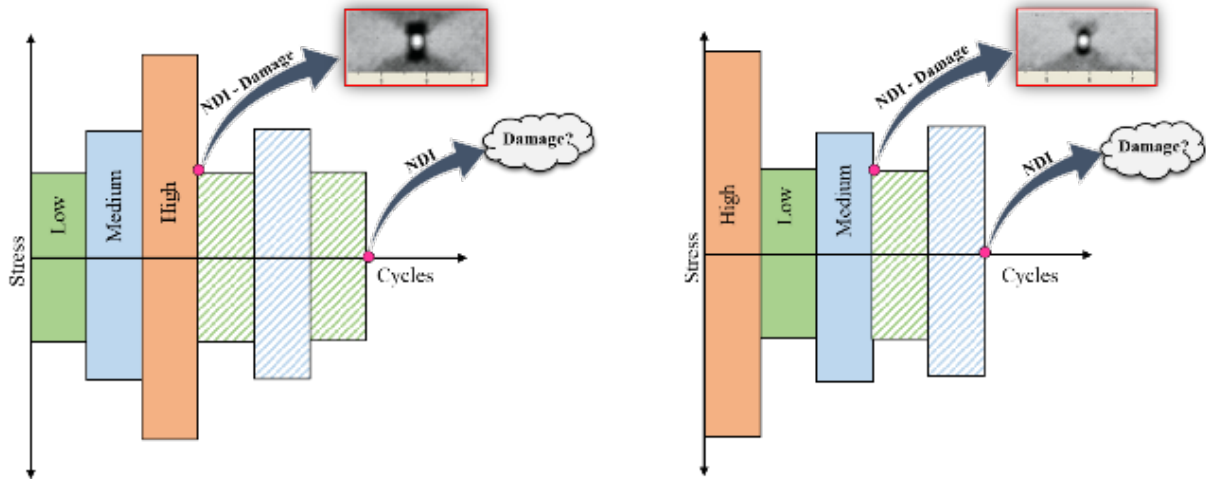


Figure 5. Effect of load sequencing on damage mechanics illustrated by initial low-medium-high- (left) and high-low-medium- (right) load occurrences

The primary goal of this research is to perform a detailed study to investigate underlying damage mechanisms under the influence of sequencing effects. Spectrum loading comprising of high-, medium-, and low-fatigue profiles were chosen. Several material systems and failure modes were evaluated under this investigation. Holes, impact damage, and delamination are common flaws in aircraft structures that contribute to failure progression under various loading conditions. The

OH specimen configuration was selected to simulate a notched specimen scenario, because holes are commonly found in aerospace applications. Damage characterization under constant-amplitude fatigue loading was conducted first in order to thoroughly document the findings. Then, the efforts were extended to block-spectrum loading.

Moreover, understanding these competing failure mechanisms and subsequent damage progression will better contribute to residual strength degradation models that are currently being developed. Methods for predicting the fatigue life of a composite structure under VA fatigue loading are in the early stages of development. Most VA fatigue analysis methods discussed in the literature cannot capture the effect of load sequencing.

2 Experimental procedures

Damage characterization under the influence of load sequencing was investigated using an OH specimen, which is akin to a notched specimen. The specimen design, materials, fatigue test methodology, test matrix, and corresponding fatigue spectra considered are discussed in this section.

2.1 Materials and methods

Out-of-autoclave (OoA) prepreg materials have demonstrated efficient production of integrated stiffened structures in aircraft with low-cost tooling. Despite the absence of high autoclave pressures, OoA materials have demonstrated comparable mechanical performance and low porosity levels compared to autoclave-cured composite materials (Dang, Bernetich, Carter, & Butler, 2011). Two material systems, OoA processed T650/5320 unidirectional tape (UNI) and plain-weave fabric (PW), were considered in this research. Specimens with QI layup configurations were utilized for this research. Table 1 summarizes the laminate configurations used in this study. All panels were fabricated using the manufacturer-recommended cure cycle (MRCC) (Solvay, 2017). Moreover, all stacking sequences satisfied the minimum post-cured part thickness requirements according to the American Society for Testing and Material (ASTM) standards.

Table 1. Laminate configurations

Laminate Description	Layup Percent 0°/45°/90°	Stacking Sequence	Total Plies
UNI-QI	25/50/25	[45/0/-45/90] _{3s}	24
PW-QI	25/50/25	[45/0/-45/90] _{2s}	16

2.1.1 Specimen design and fabrication

In accordance with the test matrices, the panel size and required numbers of panels were designated for each laminate configuration. Panels were manufactured in a contaminant-controlled clean room of the Composites Laboratory at the National Institute for Aviation Research (NIAR). Standard manufacturing and machining procedures were followed for panel manufacturing, specimen cutting, drilling, and grinding. Specimens were machined in the NIAR composite research machine shop. Upon completion of specimen machining, detailed quality checks and dimensioning were performed to ensure the ASTM standard test specimen specifications and tolerances were satisfied. ASTM standards for OH test configurations are shown in Table 2.

Table 2. OH test methods

Test Method	ASTM Standard	Evaluation Aspect
Open-hole tension (OHT)	D5766 (1995)	Tensile strength
Open-hole compression (OHC)	D6484 (2014)	Compressive strength
Open-hole fatigue (OHF)	D7615 (2019)	Fatigue response

Note that the respective ASTM standard was referenced for manufacturing, machining, and testing guidance. Figure 6 (ASTM D6484 / D6484M-14, 2014) provides the overall specimen dimensions and tolerances in accordance with the standard. OHT and OHC test methods were used to generate average static strength data to aid in the selection of fatigue SLs.

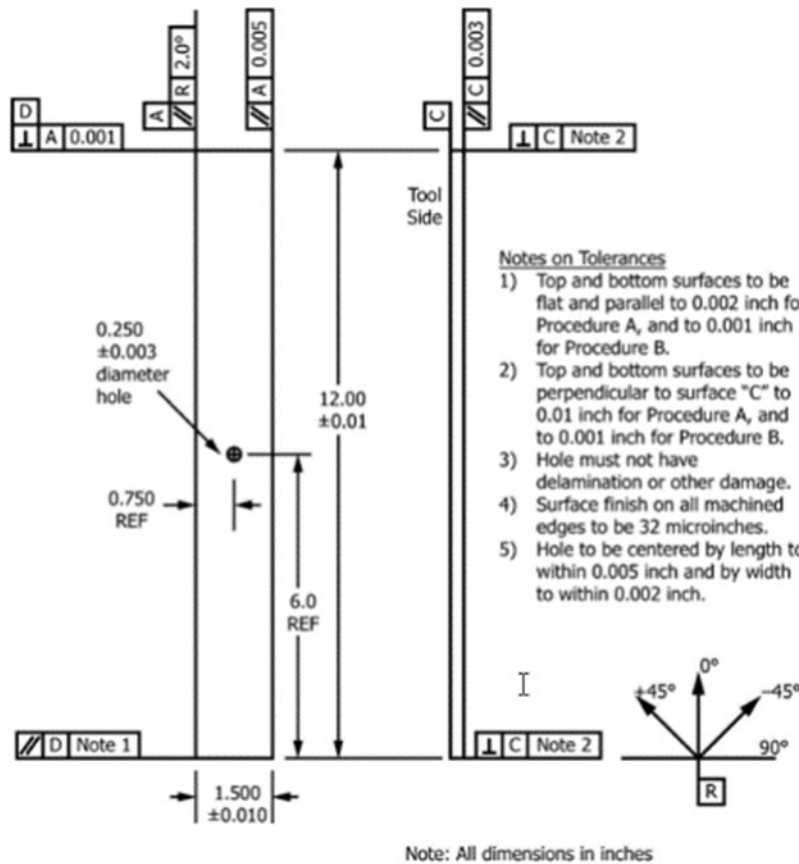


Figure 6. OH specimen dimensions and tolerances

2.1.2 Test matrix

As shown in Table 3, several CAs and block spectra were used for fatigue evaluation of T650/5320-UNI. Several high-fidelity non-destructive inspection (NDI) techniques such as X-ray computed tomography (X-CT) and X-ray digital radiography (X-DR) were employed during fatigue testing to evaluate the damage progression throughout life. In addition, digital image correlation (DIC) technique, infrared (IR) thermography, and through-transmission ultrasonic (TTU) C-Scan were also utilized for inspection of selected configurations. Primarily, X-CT investigations were used to study the governing damage mechanisms, while DIC techniques were used to track surface strains and study the damage-growth influence on outer plies.

Table 3. UNI-QI OH (24-Ply) Test matrix

Material System	Layup	Stress Ratio/ Block Spectrum	Number of Specimens	NDI
T650/5320-UNI	Quasi-Isotropic [45/0/-45/90] _{3s}	R = -1	18	TTU, Thermal, and X-CT
		R = 5	18	
		R = 0.1	18	
		Profile #3*	6	
		Profile #5*	6	
		Profile #6*	6	

*See Table 4 for details

2.1.3 Open-hole static and fatigue testing

All static tension, compression, and residual strength specimens were tested in a MTS servo-hydraulic load frame under ambient laboratory conditions. Static strength data was used for selecting fatigue SLs in order to generate CA SN curves as well as block spectra. Those specimens that encountered runouts (typically, one million cycles for CA tests or end-of-the-block spectra for VA tests) were subjected to RS assessment using standard static strength test procedures. Force and actuator displacement data were recorded from a calibrated load cell and linear variable displacement transducer (LVDT), respectively, at a constant rate of 10 Hz. Note that a load frame alignment verification check was performed prior to testing to ensure that no misalignment occurred in the load path. Since the OHT test method does not require a test fixture, the specimen was gripped directly inside the hydraulic grip assembly. However, the OHC specimens were inserted with the aid of standard anti-buckling compression fixtures. After verifying specimen flushness, the test fixture along with the installed specimen were gripped into the hydraulic grip assembly. The load frame control mode was switched to load-control to prevent the specimen from any unnecessary preloading. Grip pressure was adjusted based on the expected ultimate load of the specimen to eliminate slippage but controlled under a critical value to prevent damage in the gripped region of the specimen. After top and bottom grips were completely engaged, fasteners in the fixture were torqued to their final torque values recommended in the ASTM standard. Subsequently, gripped specimens were loaded to failure at a constant displacement rate of 0.05 in/min. The failure event was defined as either a two-part failure (specimen breaking into two parts) or when the load dropped by 30–70%, as defined in the ASTM standard. Failure modes were thoroughly checked at the completion of each test to ensure that specimen failure was an acceptable mode according to ASTM standards. The OHT and OHC test setups, outlined in ASTM D5766 (1995) and ASTM D6484 (2014), respectively, are shown in Figure 7.

The ASTM D7615 (2019) standard was used as the guide for the open-hole fatigue testing. Multiple fatigue tests were conducted with various stress ratios (see test matrix in Table 3); anti-buckling fixtures used for the stress ratios included compression loading or load reversal. Mechanical cycling was performed in force control mode, and a cosine-loading function form with a frequency of 5 Hz was chosen. Stiffness degradation (SD) was monitored throughout the mechanical cycling to corroborate damage progression findings. Any change in the specimen temperature was also monitored for selected specimens during fatigue testing to ensure that this change was within the bounds specified in the respective ASTM standards. Grip pressure was adjusted to ensure that there was no slippage throughout the fatigue test. Similar to static tests, failure modes were thoroughly investigated after every test to ensure that acceptable failure modes were achieved.

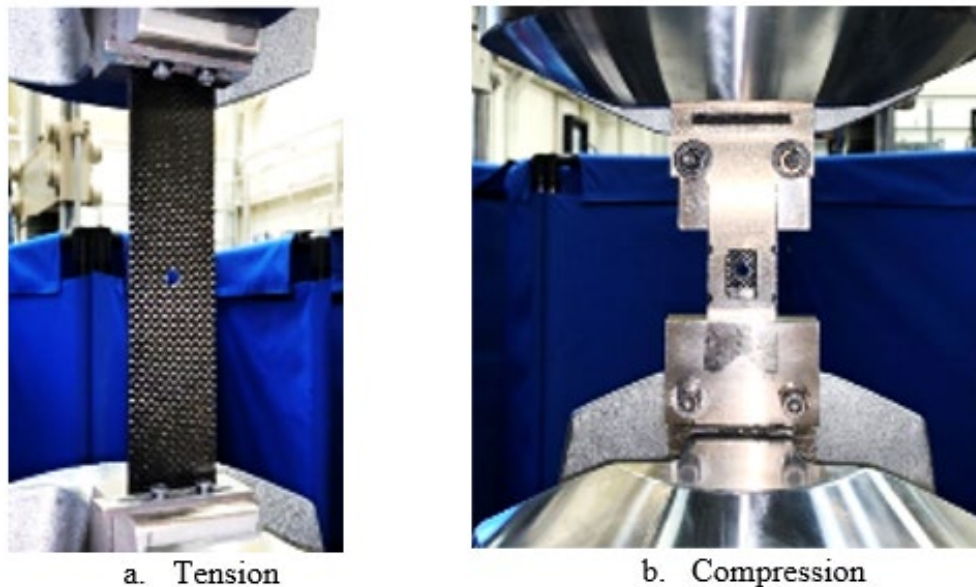


Figure 7. OH test setups

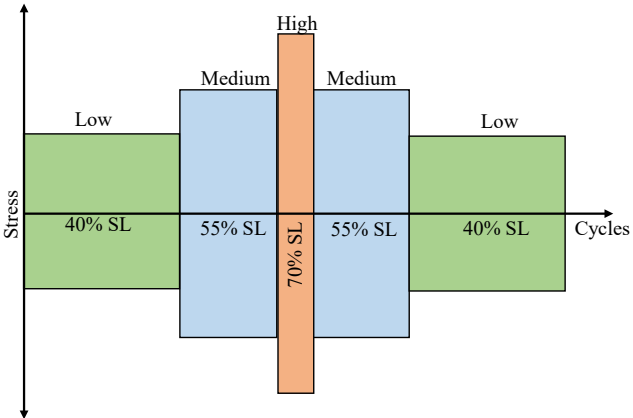
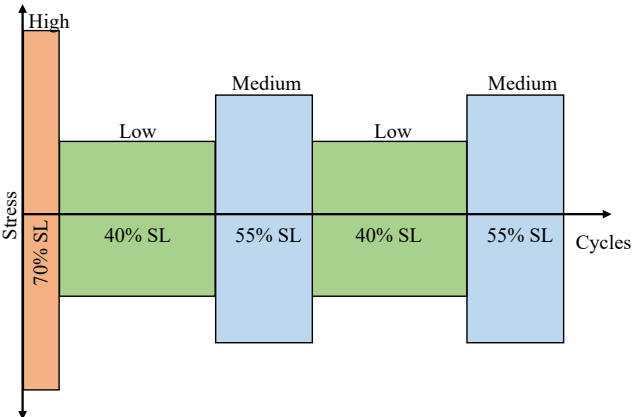
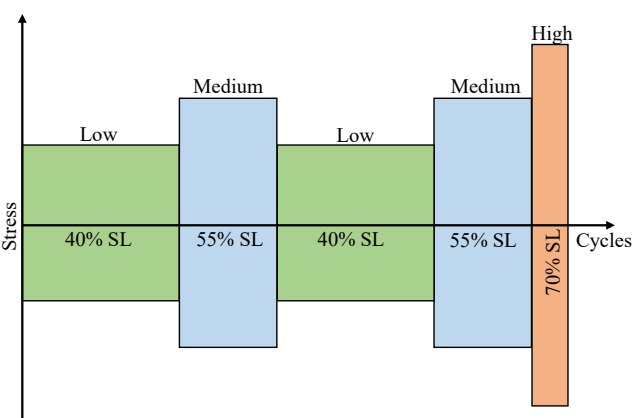
2.2 Fatigue load spectra for load sequencing

A typical flight spectrum is comprised of several stress ratios with varying amplitudes. In order to simplify testing, the flight-by-flight spectrum is converted and sequenced as multiple constant-amplitude fatigue blocks that produce equivalent damage severity. The block spectra used for this investigation are further simplified, primarily to investigate the sequencing effects; thus, they have no direct correlation to a specific flight spectrum. Block-spectrum fatigue invokes unique damage characteristics, because it is inherently comprised of several CA fatigue profiles. Note that a block spectrum may consist of a single R-ratio with multiple amplitudes, or varying R-

ratios. Prior to performing studies to consider sequencing effects, a thorough damage characterization under CA fatigue loading was performed. The CA tests considered three unique stress ratios: $R = 0.1$ (tension-tension), $R = 5$ (compression-compression), and $R = -1$ (fully reversed tension-compression).

Multiple instances of low, medium, and high LBs were arranged in different orders for investigating the sequencing effects (Table 4). Low, medium, and high LBs for UNI were chosen as 40, 55, and 70% of the average static strength, respectively. The typical once-per-lifetime load, or design limit load (DLL), is less than the selected 55% SL. Hence, the chosen 70% SL was significantly higher than typical aircraft operational loads. Also, note that the spectra presented here to study the sequencing effects all have a constant stress ratio of $R = -1$. Additional studies were conducted with stress ratios of $R = 5$ and $R = -1$ at other SLs (50, 60, 70, and 80%). Furthermore, several tests were conducted with variable R-ratios. Block spectra selected for these additional studies are discussed in section 3.3.3. The number of cycles for each stress level of block spectra was determined as the 20% of average failure number of cycles for the corresponding stress level using SN data for the UNI-QI configuration.

Table 4. Block spectra used to investigate Sequencing Effects on UNI-QI OH specimens

	Block Spectrum	Notes
Profile #3		<p>Low-Medium-High-Medium-Low Stress Level</p> <p>Low: 40% Medium: 55% High: 70%</p> <p>Cycles for each block: n = (400,008; 116,330; 3,000; 116,330; 400,008)</p>
Profile #5		<p>High-Low-Medium- Low-Medium Stress Level</p> <p>Low: 40% Medium: 55% High: 70%</p> <p>Cycles for each block: n = (3,000; 400,008; 116,330; 400,008; 116,330)</p>
Profile #6		<p>Low-Medium-Low- Medium-High Stress Level</p> <p>Low: 40% Medium: 55% High: 70%</p> <p>Cycles for each block: n = (400,008; 116,330; 400,008; 116,330; 3,000)</p>

3 Results and discussion

As discussed previously, a block spectrum is realized by grouping several CA loading blocks. In order to evaluate the damage mechanics associated with block spectra loading and thereby the sequencing effects, first, constant-amplitude fatigue testing was performed in order to characterize the damage thoroughly. Subsequently, efforts were focused to study the sequencing effects. For CA tests, only 24-Ply UNI-QI OH specimens were considered. Both UNI and PW specimen configurations were considered to characterize damage from the sequencing effects. Damage characterization under CA and ramifications due to load sequencing (for three load profiles) are discussed in detail in this chapter. Subsequently, supplementary studies to characterize the damage mechanisms on variable-amplitude fatigue with constant and variable stress ratios are also discussed.

3.1 Constant amplitude fatigue damage characterization

The CA tests were performed primarily to investigate the damage progression for a given R-ratio. In order to characterize the failure modes, high-fidelity X-CT NDI was primarily used. High-resolution results generated from X-CT were used to perform comprehensive damage analysis (North Star Imaging). A detailed ply-by-ply analysis from X-CT scans was conducted, and results were examined to investigate the primary damage mechanisms, damage progression, and failure mode interaction in each ply. Results indicate higher damage severity in the outer plies of OH specimens compared to the damage in the inner plies. Findings during the CA failure characterization study were compared against findings in the literature and are also discussed here. Since X-CT data acquisition and image reconstruction are time-consuming, quick X-DR scans, which are essentially projections of internal characteristics onto a two-dimensional plane (C-Scans), were first taken to detect the presence of any damage. If any damage was detected, then X-CT scanning was performed to conduct detailed ply-level analysis. The scan intervals were such that longer interval times were chosen at the beginning of testing, and the interval was reduced significantly with the onset of damage.

Figure 8 illustrates primary failure mechanisms observed using high-fidelity X-DR scans for a 24-Ply UNI-QI OH specimen at 325,000 cycles. The X-DR scan clearly shows fiber breakage in the 0° ply, fiber splitting or matrix cracks along the 0° and 45° plies, and delamination(s). Fiber splitting occurs when the matrix that binds the fibers together becomes weak and fails. Fiber breakage occurs when individual fiber fails in tension/compression. As discussed later, in quasi-isotropic specimens considered here, the failure of 0° fibers is difficult to observe during tensile fatigue since they occur much closer to failure load and cause instantaneous failure. In addition,

the majority of 0° fiber failures will occur closer to the failure load. However, not all fibers have the same strength, and a few of the weaker fibers may break in earlier cycles (or if statically loaded at lower loads). Such early weak fiber failures in tensile loading are difficult to detect. Intralaminar microcracks coalesce and propagate towards the interface and weaken the interface. These intralaminar cracks and fiber breaks weaken or soften the composite layer and cause load shedding to adjacent plies. When there are adjacent dissimilar ply angles, these cracks tend to produce delaminations at the weakened interface.

Delamination in the OH specimen originates near the tangential fiber splitting, noted on the 45° plies (top right-hand side). Subsequent X-CT on this specimen confirmed delamination in this area. Predominant failure mechanisms associated with CA tension, compression, and fully reversed fatigue-loading scenarios are presented in detail in the following sections.

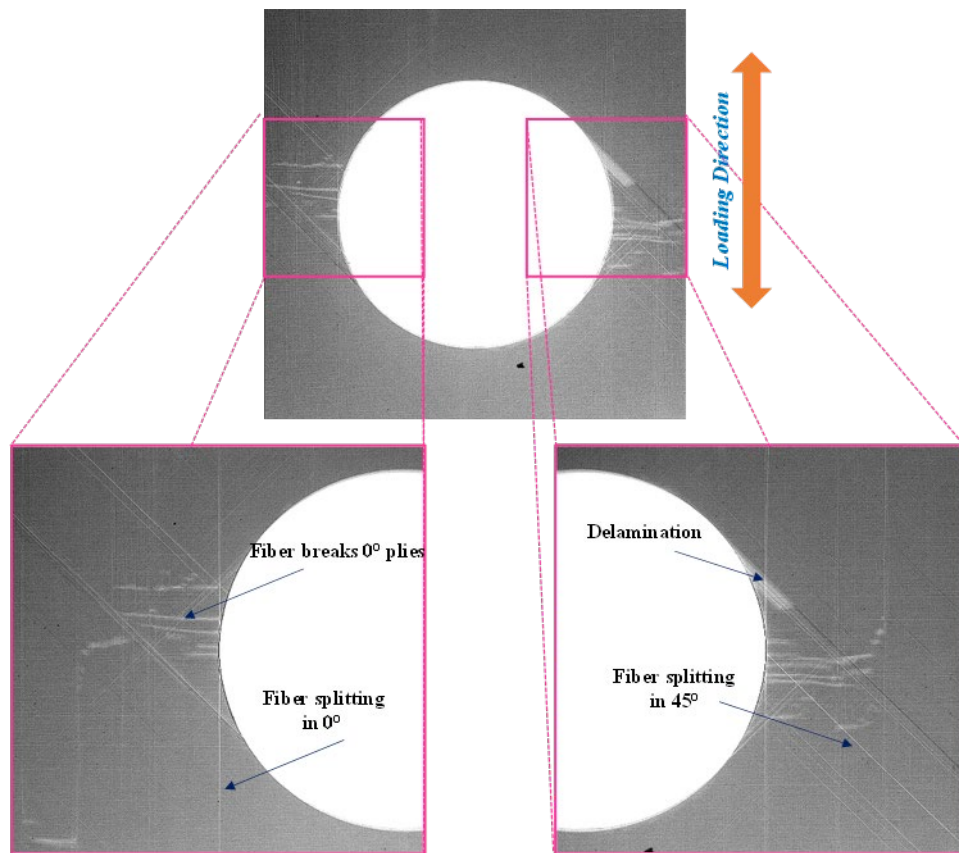


Figure 8. X-DR scans of 24-Ply UNI-QI OH specimen showing characteristic damage modes (55% SL, $R = -1$ at 325,000 cycles)

3.1.1 Tension-tension fatigue ($R = 0.1$)

CA tension fatigue on 24-Ply UNI-QI OH specimens was conducted at higher stress levels (85–90%). At high stress levels, these specimens survived one million cycles (runouts). Despite their survival, the specimens were severely damaged, as shown in Figure 9. As shown, massive delamination and fiber splitting along the 45° fiber angle occurred toward the end of one million cycles. Yan et al. (1999) observed that the primary failure mechanisms during notched tension composite fatigue tests are fiber splitting, delamination, and eventual fiber breakage that led to ultimate fatigue failure. Damage characteristics observed here during CA tension fatigue are similar and were corroborated using a detailed ply-level analysis carried out at intermittent cycles using X-CT.

The matrix region around the 90° plies is the weakest link in the loading direction, and matrix cracking or fiber splitting typically occurs in the very early stages of loading along the 90° plies. As fatigue testing progresses, these cracks grow further into the off-axis plies (45°) due to their lower load-carrying capabilities compared to 0° fibers. Initially, these cracks are not visible, even with high-resolution X-CT scans, and they tend to increase significantly prior to being noticed, as shown in Figure 10(a). Thus, during the initial stages of high-resolution X-CT scans, matrix cracking leading to fiber splitting along the 90° plies was not detected. However, these cracks became more pronounced during the later stages and were picked up by the X-CT scans. Note the following regarding X-CT scans: the high-fidelity scanning was performed at intermittent cycles without any external loading. In order to detect cracks along 90° plies in the initial stages, a small amount of external load, just enough to open up the cracks, is required. This might explain why cracks along the 90° plies remained undetected in the initial stages.

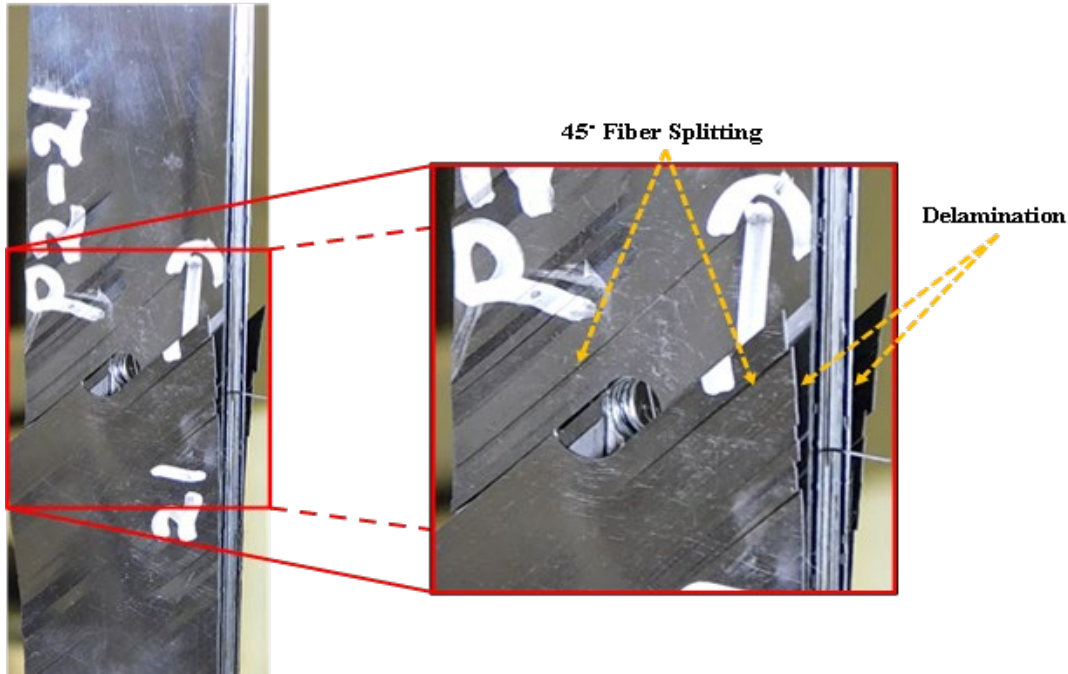


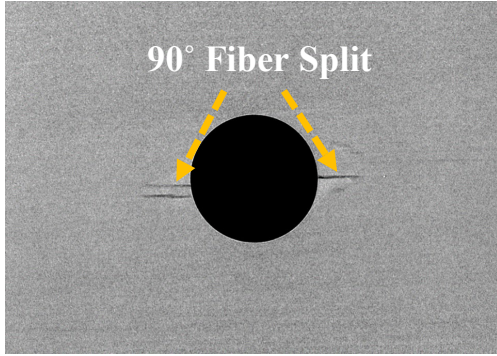
Figure 9. Delamination between plies and 45° fiber splitting of OHF specimen ($R = 0.1$ at one million cycles)

The matrix plays a minor role in the load-bearing capabilities along the fiber direction, but its primary role is to keep the fibers intact (bind them together) and protect them from the surrounding environment. However, matrix cracking influences the matrix-dependent properties such as compressive and transverse properties in composites. As the cycle count increases, the matrix starts to weaken, thus leading to fiber splitting or matrix cracking. At higher loads, a weakened matrix causes strain mismatch between fibers and the matrix and introduces shear, as documented in Spearing & Beaumont (1992). This is common among the off-axis (45°) outer plies, as shown in Figure 10(b). In addition, longitudinal fiber splitting (along 0° fiber direction) is initiated at high-stress concentration areas (notch tips), as shown in Figure 10(c). At the notch tip, fibers are discontinuous, which leads to local stress redistribution, whereby excess loads are transferred to the closest plies. As the load increases, thereby weakening the matrix, fiber splitting initiates at the notch tip. Weakened 90° and 45° plies tend to redistribute the loads onto 0° plies. As the number of cycles increases, continuous matrix cracking complicates boundary conditions, thereby introducing other severe failure mechanisms such as delamination and eventual fiber breakage due to overloaded fibers.

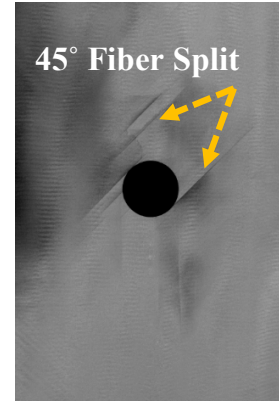
Another prominent failure mode observed in fatigue testing is delamination, as fiber splitting leads to the weakening of ply interfaces, which eventually causes delamination between

neighboring plies. In general, delamination initiates around the free edges or notches. Crack initiation that occurs around notches can generate out-of-plane stresses. In addition, due to the presence of outer 45° plies, free-edge delamination was observed, as corroborated in the work of Whitney and Browning (1972). Note that the “free-edge-effect” is observed in specimens with 45° outer plies, where significant interlaminar normal stresses occur when subjected to uniaxial tensile loading. Delamination between adjacent plies, as well as along the free edges, are clearly marked in the inset of Figure 9 for the damaged coupon. In addition, delaminations are clearly noted in detailed X-CT scans in the through-thickness direction, as shown in Figure 11. Note that when complete delamination between plies occurs (as shown in Figure 9 and at one million cycles in Figure 11), the specimen acts akin to multiple laminates bundled together. Despite excessive delamination at one million cycles, the load-bearing 0° plies remain intact and carry the load until failure.

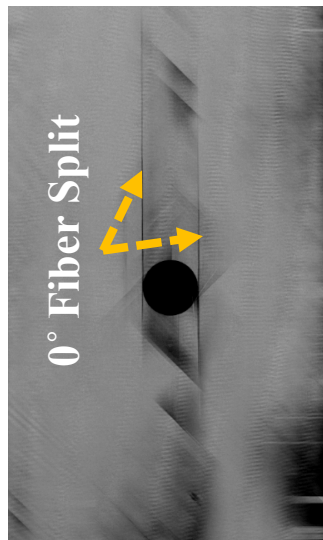
It has been observed that the ultimate failure mode in tension fatigue loading is typically governed by the breakage of fibers (O'Brien, 1985). Fiber breaks are the most critical and catastrophic failure mechanism among all composite damage modes. However, due to high stress levels, the progression of catastrophic fiber breaks appears instantaneous from the point of detectable fiber breakage. Random weaker fiber breaks may occur earlier, affecting the stress concentration. Nonetheless, once there is enough failure to be detectable, failure is abrupt. When multiple fiber breakages occur, the load redistribution initiates fracture in additional fibers, which ultimately compromises the structural integrity. This load redistribution to neighboring plies can also cause a slowdown in damage progression. Throughout the CA tension fatigue study, 0° fiber breaks were not observed until the onset of ultimate specimen failure.



(a) Fiber splitting in 90° ply at one million cycles (closer to failure)



(b) Fiber splitting in 45° outer ply



(c) Fiber splitting at crack tip along 0° ply

Figure 10. Examples of Fiber Splitting (matrix cracks) in various ply orientations

S

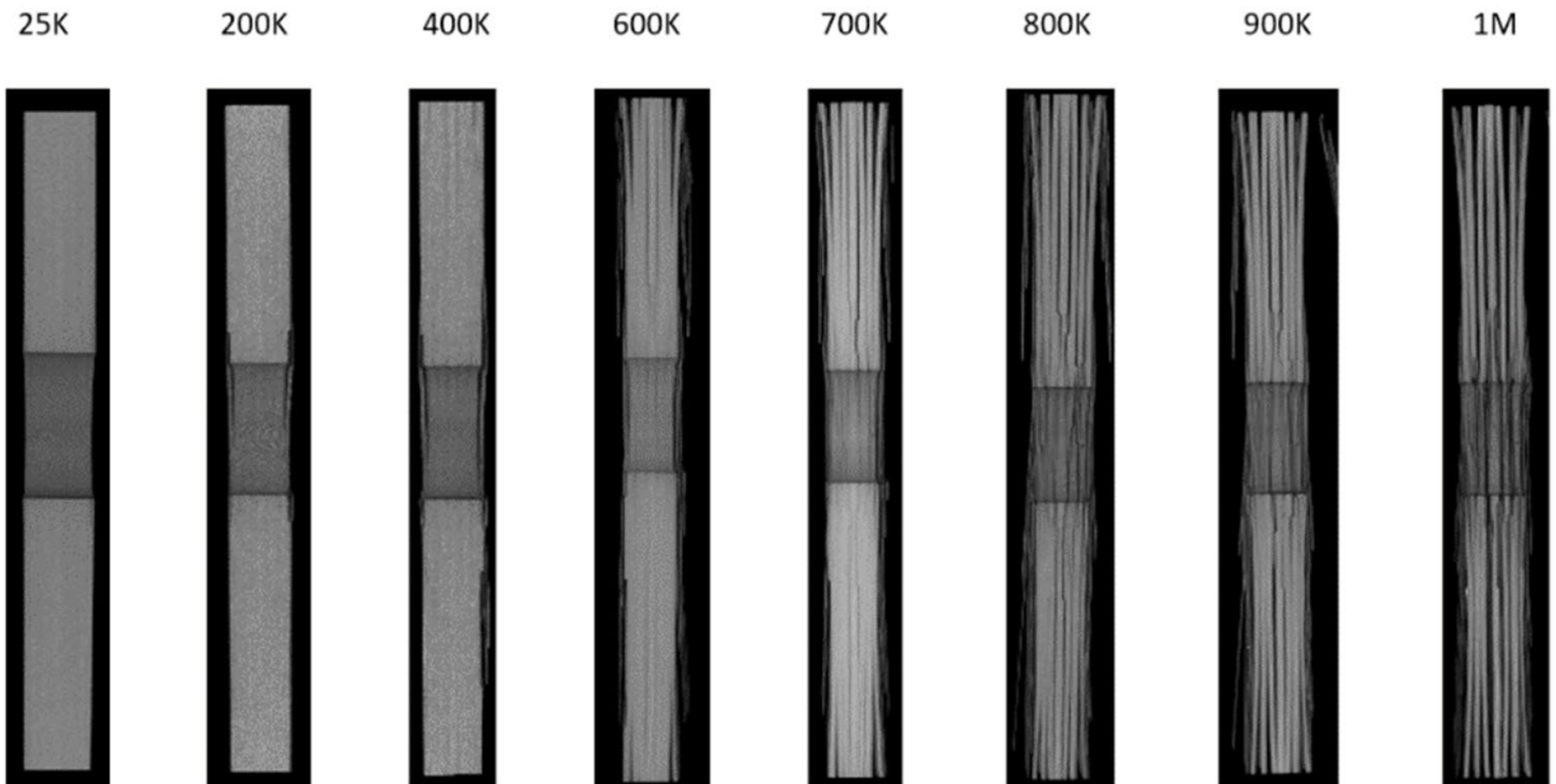


Figure 11. Cross-sectional (thickness direction) views of X-CT of OHF specimen ($R = 0.1$ at 25,000 to one million cycles)

All tension fatigue tests were conducted at high stress levels (85–90% SL); initial fiber break progression leading to ultimate failure was nearly instantaneous, and performing an inspection during fiber-break progression was tedious. This is evidenced by detailed X-CT slices of 0° and 90° plies shown at one million cycles in Figure 12, where no indication of 0° fiber breaks is observed. However, in the case of the 90° ply, both fiber break and fiber splitting are clearly visible. Fiber breaks were noticed in 90° plies during CA tension fatigue (high SL of 90%) due to the transverse compression loading carried by 90° plies (a result of Poisson effect). Moreover, the absence of anti-buckling fixtures during the tension fatigue also increased the severity of the damage (micro-buckling) caused by transverse compression loading in 90° plies, as seen in Figure 12 (b). For a detailed X-CT analysis of CA tension fatigue across various numbers of cycles, refer to Appendix A.

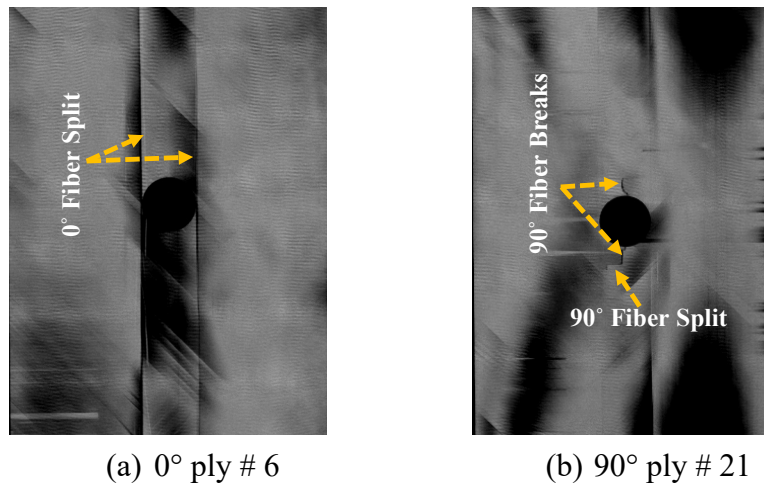


Figure 12. 0° Ply #6 and 90° Ply #21 of UNI-QI CA (90% SL, R = 0.1 at one million cycles)

Throughout fatigue testing, the apparent stiffness degradation of each specimen was monitored in terms of the change in slope of the load vs. displacement curve during fatigue. Although SD is calculated with the aid of a machine load-cell and LVDT, the machine compliance is thought to be of less significance in correlating damage characterization discussions. Hence, X-CT images were also compared against a plot of SD, as shown in Figure 13. Damage accumulation throughout the test and critical failure initiations were investigated on multiple plies. SD on all tested specimens is presented here, and critical damage modes observed across multiples plies are presented here for a chosen specimen. All of the characteristic damage mechanisms discussed above for tension fatigue loading were observed. Note that X-CT images depicting damage profiles beyond $n > 925,000$ cycles are not included in the plot due to excessive delamination. In general, SD was observed with a characteristic kink closely after approximately 44,000 cycles. X-CT scans right after this behavior reveal excessive fiber splitting in the outer plies.

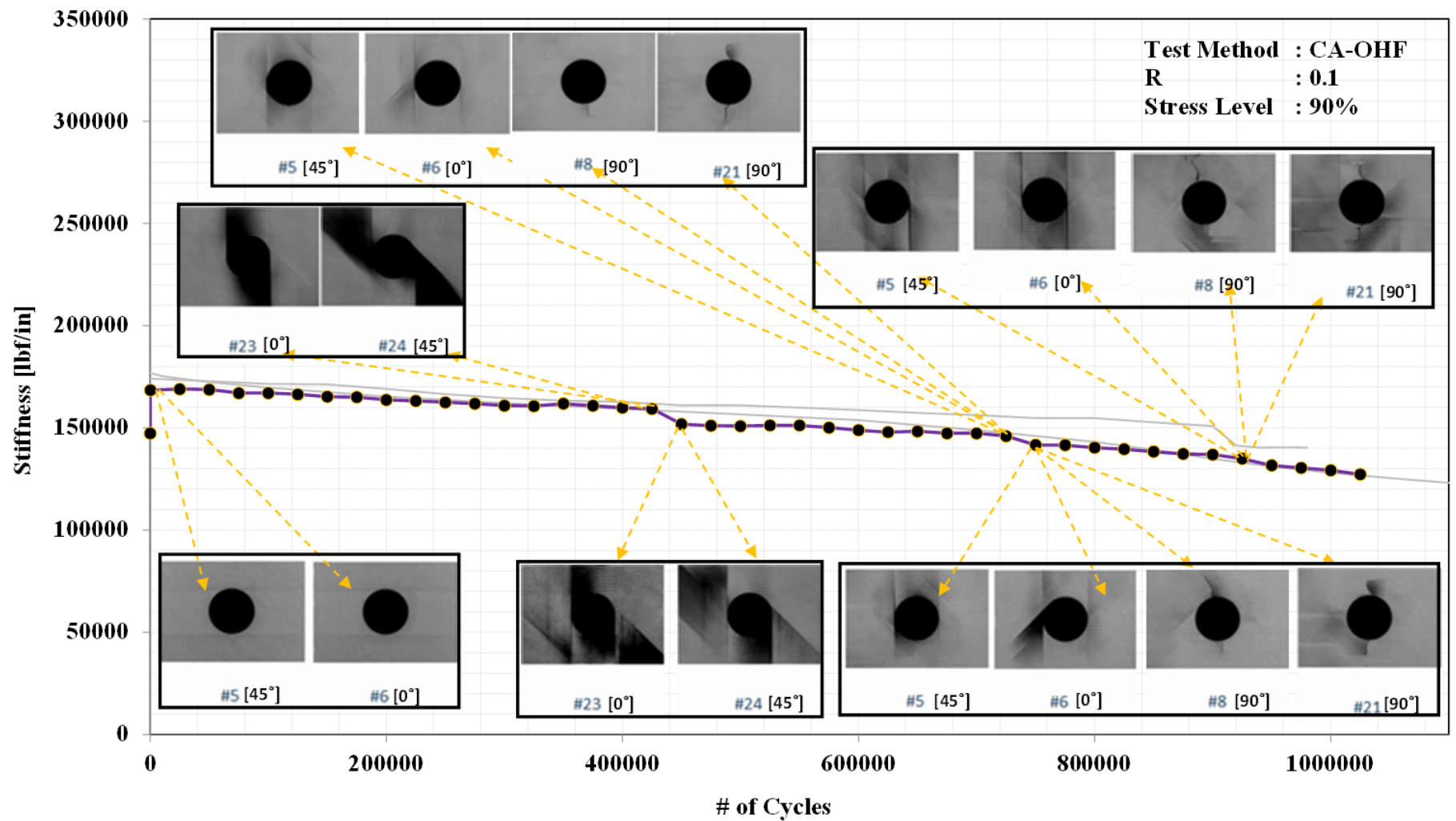


Figure 13. Apparent Stiffness degradation of UNI-QI CA (90% SL, R = 0.1); damage in critical plies for Specimen #21

3.1.2 Compression-compression fatigue ($R = 5$)

In general, composite laminates are weaker under compression loading than tension loading because extra failure mechanisms are involved, which was clearly evident during fatigue testing. In addition to all failure mechanisms discussed previously for tension fatigue loading, buckling is the dominant failure mechanism during compression fatigue. Macro- and micro-buckling are critical failure modes in composite testing (Badaliance & Dill, 1982). Most of the tests and fixtures are designed to prevent macro-buckling of the entire test article. However, micro-buckling is the most critical and driving failure mode under compression loading. Naik and Kumar (1999) discussed two different micro-buckling mechanisms: (a) fibers buckling out of phase in the extension mode and (b) fibers buckling in phase in the shear mode, as shown in Figure 14.

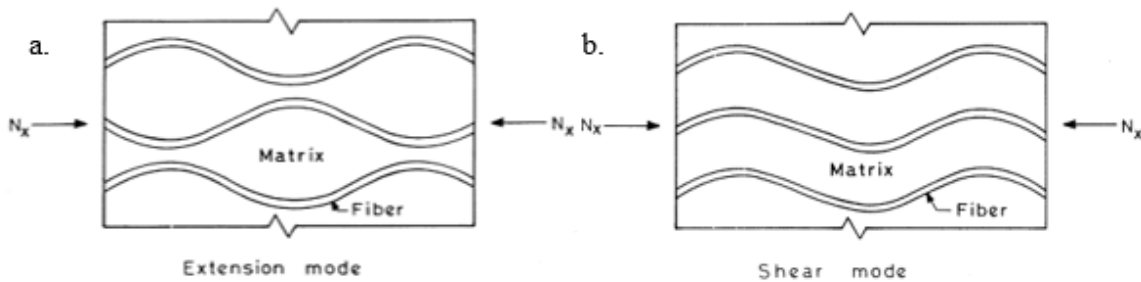


Figure 14. Predominant micro-buckling modes in compression

Extension mode fiber buckling (when fibers buckle individually relative to each other) occurs when the laminate fiber volume fraction is less than 30% (Treasurer, 2006). Typically, laminates in aerospace applications have fiber volume fractions much greater than 30% (Camponeschi, 1991). Therefore, shear mode micro-buckling is the most common buckling mode observed. Micro-buckling ultimately leads to kink bands (kinking), as discussed by Evans and Adler (1978), and a schematic of a plane kink band is shown in Figure 15. This distinct kink band shape is observed during compression and shear as a result of the shear mode micro-buckling (Berg & Salama, 1973). In notched composites, kink bands are highly likely to occur at the crack tip because fibers tend to buckle into the unsupported notch. Eventually, kink bands lead to fiber breaks, as shown in Figure 16 (Evans & Adler, 1978). Kinking promotes an increase of fiber breakage, which significantly increases fiber splitting (matrix cracking) and delamination in the neighboring plies. Fiber breaks and splitting observed on the outer 45° ply is shown in Figure 17 at $n = 45,000$ cycles. In contrast to the tension specimens fatigued at 90% SL, compression fatigue runouts were observed at 65% SL.

In order to achieve a comprehensive understanding of the overall damage progression during fatigue, critical failure initiations and their accumulations in all plies were investigated. The damage accumulation on critical plies using detailed X-CT images was plotted against the SD curve, as shown in Figure 18. The compression failure mechanisms discussed above that lead to fiber breakage are clearly visible in this plot. CA tension and compression fatigue failure mechanisms were compared by performing a side-by-side comparison of detailed ply-by-ply X-CT analysis of runout specimens, as shown in Figure 19. It is clearly evident that the damage mechanics in tension and compression CA fatigue loadings are different. A detailed ply-level analysis of each specimen for CA compression fatigue loading can be found Appendix A. As observed in Figure 19, delamination and fiber splitting are the prime mechanisms for tension that govern failure, whereas fiber breakage and fiber splitting failure modes resulting from shear mode kinking are more dominant in compression.

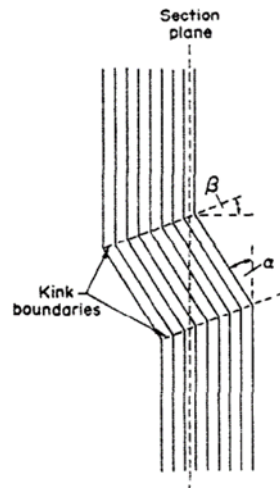
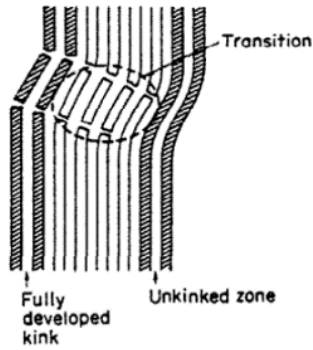
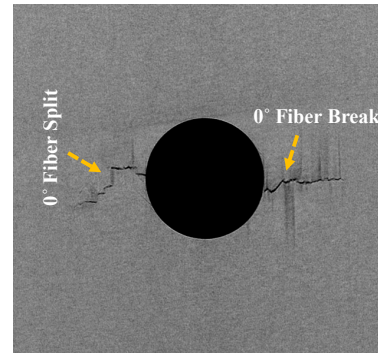


Figure 15. Kink band with kink orientations (α , β) and boundaries



(a) Fully developed kink band



(b) Fiber breaks in 0° ply during compression fatigue at 34,000 cycles

Figure 16. (a) Schematic illustration of kink band and (b) X-CT of fatigue specimen ($R = 5$)

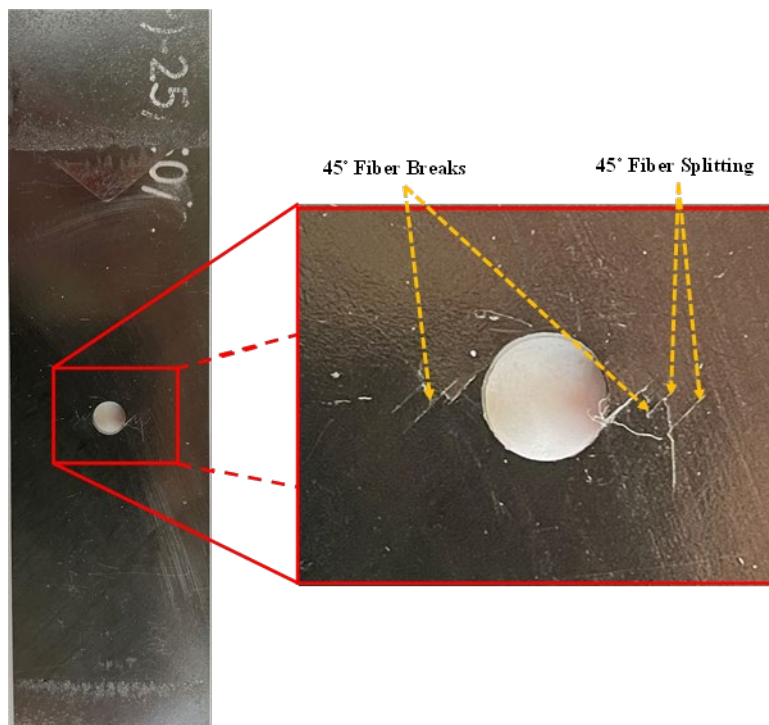


Figure 17. Fiber breaks and splitting of OHF specimen ($R = 5$ at 45,000 cycles)

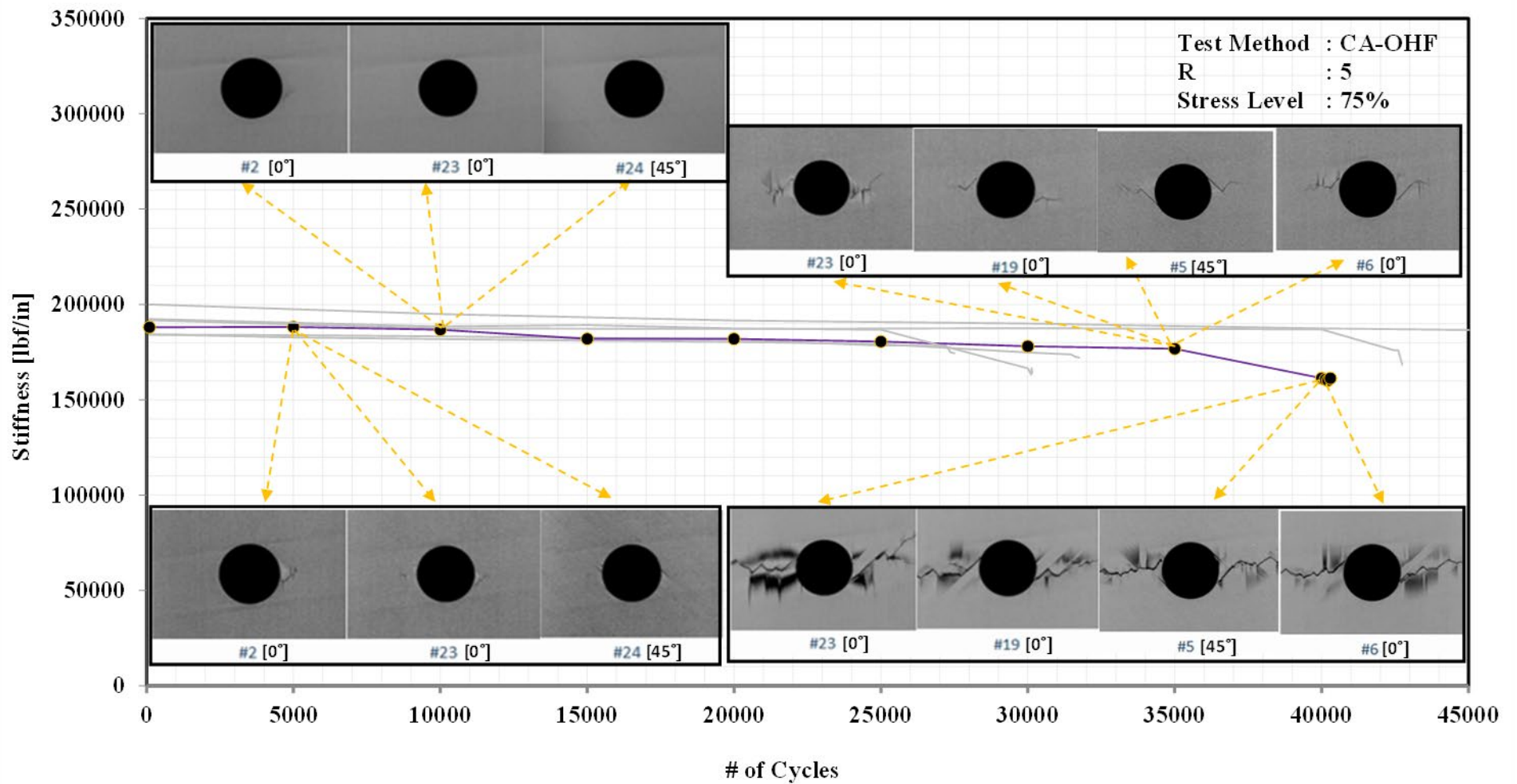
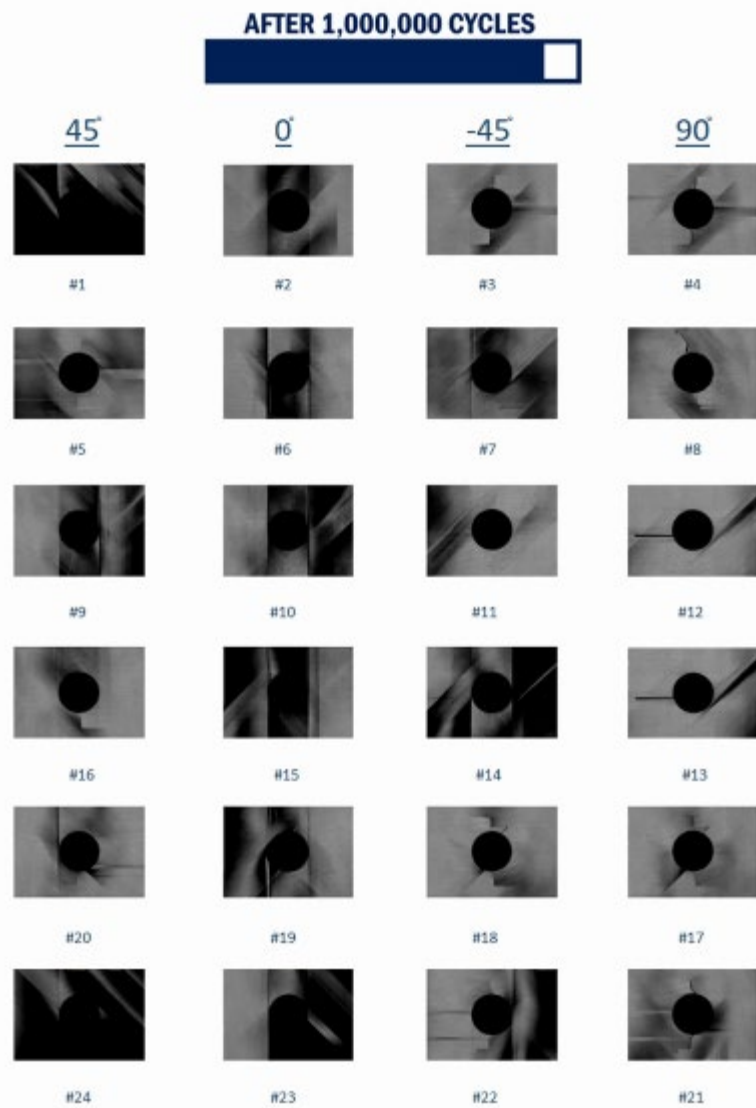
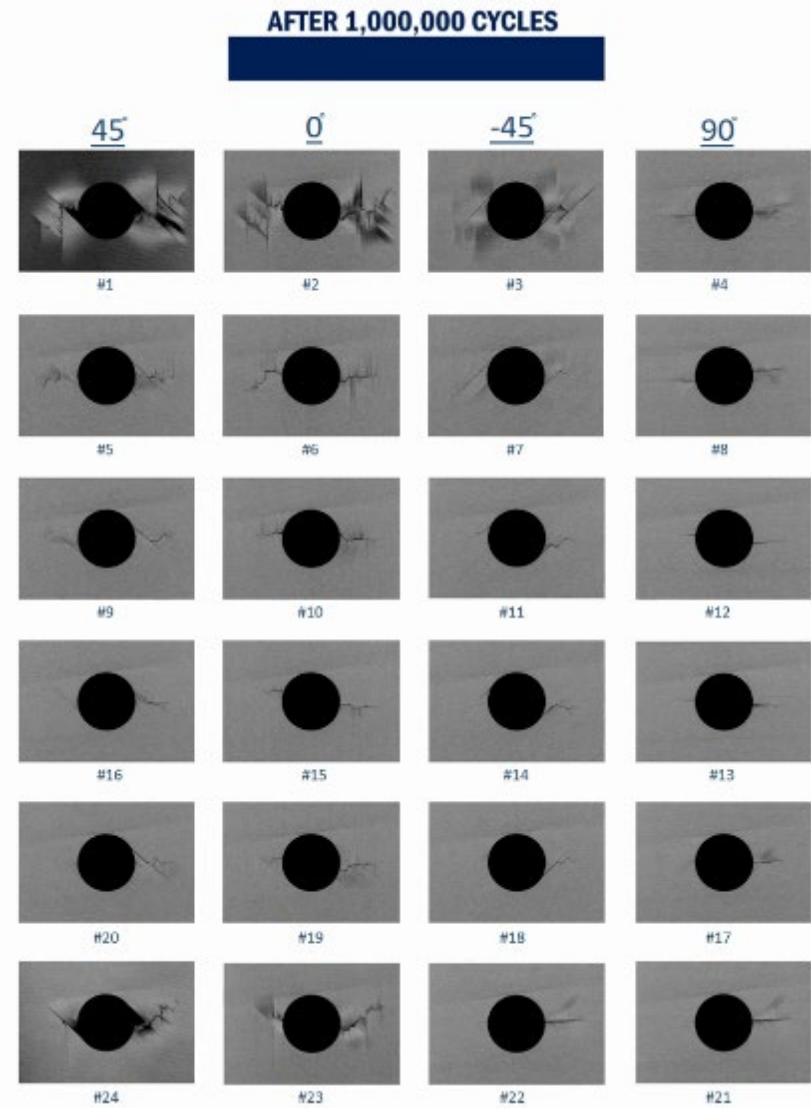


Figure 18. Stiffness degradation in UNI-QI CA specimen (75% SL, R = 5); damage accumulation in critical plies for Specimen #8



(a) X-CT ply-level scan of UNI-QI ($R = 0.1$)



(b) X-CT ply-level scan of UNI-QI ($R = 5$)

Figure 19. CA tension vs. compression failure mechanisms in each ply of UNI-QI ($R = 0.1$ and $R = 5$ at one million cycles)

3.1.3 Fully reversed fatigue ($R = -1$)

Fully reversed fatigue loading is one of the most damaging stress ratios. Fully reversed UNI-QI OH specimens fatigued at 55% SL were monitored in close intervals to identify the presence of major failure mechanisms during fatigue testing. Runouts were observed at 45–50% of the ultimate static strength. In addition, the failure mechanisms, coupled interactions, and progressions were closely monitored using X-CT. All tension and compression dominant failure mechanisms were detectable with X-CT. Isolated weak fiber failures do occur and reduce local stiffness that relieves some critical stress concentrations. However, until their failure becomes dominant approaching the average fiber strength, they do not appear in clusters and remain undetectable with X-CT. The X-CT inspections were performed every 5,000 to 10,000 cycles. During fatigue testing, the first instance of damage was observed around 10,000 cycles in the 45° outer plies, in which only fiber splitting (matrix cracking) occurred along the fiber direction tangential to the hole boundary. Fiber splitting in the outer 45° ply along with delamination for a specimen that underwent 730,000 cycles is shown in Figure 20.

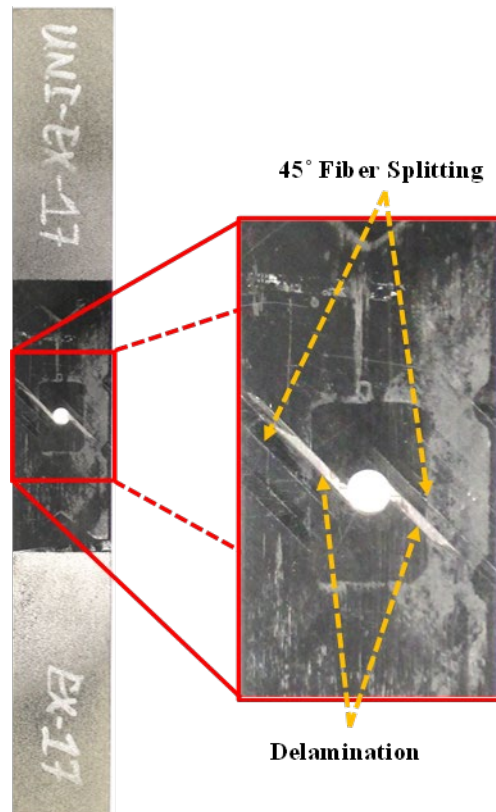


Figure 20. Fiber breaks and splitting on outer 45° ply and delamination at CA of OHF specimen ($R = -1$)

Major fiber splitting began tangentially to the location close to the highest stress concentration regions, as can be seen in Figure 21(a). An extension of this damage occurred subsequently at 15,000 cycles, as shown in Figure 21(b). X-CT performed at 25,000 cycles showed visible fiber matrix splitting in the neighboring 0° plies. Fiber splitting occurred along the fiber direction and tangential to the hole boundary, as shown in Figure 21(c). This was followed by fiber breaks in the same 0° plies around the highest stress concentration region of the hole. The fiber breaks were slightly offset and away from the 45° fiber splitting in the neighboring plies. At the end of each fiber break, fiber splitting was observed along the direction of the fibers, as can be seen in the X-CT scan performed at 35,000 cycles, shown in Figure 21(d). This is yet another cue that isolated “weaker” fiber failure occur, possibly both in tension and compression kink mode, which reduces the peak stress concentration by lowering the local stiffness. Within 30,000 to 35,000 cycles, fiber splitting failure initiated in the neighboring -45° plies. Failure initiated in the direction of the fibers tangential to the hole boundary and was opposite to the failure initiation observed in the -45° plies, as can be seen in Figure 21(e). Indications of delamination were observed at 40,000 cycles. Figure 21(f) shows delamination that initiated between the 45° fiber splitting and fiber breaks. Later inspections revealed multiple fiber splitting occurrences in 0° , 45° , and -45° plies. Delamination often formed around existing failures at the adjacent plies. In addition, new fiber breaks were formed in different locations along the existing 0° fiber splits.

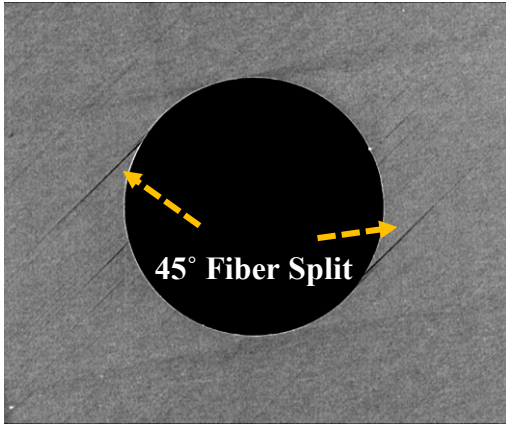
Detailed ply-level analysis using X-CT at inspection intervals of 250,000 cycles (55% SL, $R = -1$) is shown in Figure 22(a). Apart from the observed damage mechanisms and progression, in outer 45° , 0° and -45° plies, the only failure witnessed until 250,000 cycles was fiber breakage in the inner load-bearing 0° plies as shown in Figure 22 (a). In subsequent cycles, matrix cracks, delamination, and fiber splitting started to form around existing fiber breaks in the inner 0° plies. These mechanisms repeated until the ultimate failure of the specimen occurred. A detailed ply-by-ply X-CT scan performed just prior to the ultimate failure at 730,000 cycles (55% SL, $R = -1$) is shown in Figure 22 (b).

The damage extent of a fully reversed fatigue profile ($R = -1$) is significantly greater than what is observed in a comparison of tension-tension (90% SL, $R = 0.1$) and compression-compression (75% SL, $R = 5$) X-CT scans at one million cycles, shown in Figure 19. However, the delaminations observed during fully reversed fatigue were lower compared to tension-tension fatigue but higher compared to compression-compression fatigue. An anti-buckling fixture (similar to $R = 5$ compression fatigue) was employed during fully reversed fatigue, which was influential in reducing the extent of delamination. Figure 22 shows free-edge delamination, and it

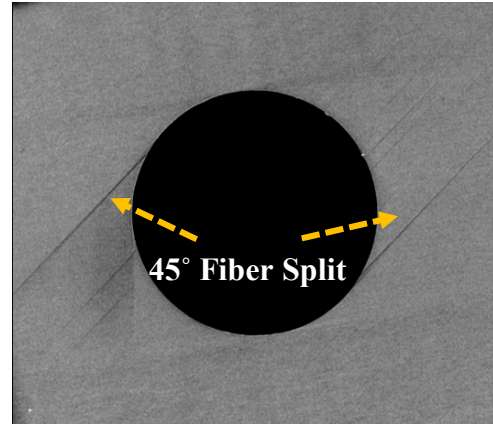
can be noted that they were restricted in both cases (compression and fully reversed fatigue) where the fixtures were used. As noted previously, this can contribute to the size effects in finite width specimen; however, the behavior will be consistent across various loading conditions, as the specimen width chosen here is in accordance with the ASTM standard and remains constant. A significant number of fiber breaks was observed in the 0° load-bearing plies, although there were no such indications of fiber breaks during tension-tension fatigue.

In the compression portion of the fully reversed fatigue, failure mechanisms such as micro-buckling and kinking initiated the fiber breaks. Subsequently, the tension portion of the fatigue loading caused a significant amplification of these fiber breaks when compared to the compression-compression fatigue scenario. The change in severity of the fiber breaks between the two R-ratios is highly noticeable; see Figure 19(b) and Figure 22. In order to achieve comprehensive understanding of overall damage progression during fatigue, critical failure initiations and their accumulations in all plies were investigated and included in the stiffness degradation plot. Important observations on various plies compared with SD are shown in Figure 23. No characteristic kink in the SD plot was observed, and a steady decrease in SD was observed. A comment is made here regarding the weak fiber failures (0° tensile fiber failure) that occur at lower cycles or when loaded under static conditions at lower loads. These failures are hard to detect; however, they contribute to predicting the notch sensitivity parameter. Theories that try to predict notch sensitivity (the effect of hole size on notched strength) often employ fiber strength distribution as an energy parameter for ply failures in order to predict notched strength for a range of hole sizes. In the fully reversed fatigue loading, $R = -1$, fiber breaks are much easier to detect due to the height of the kink band formation.

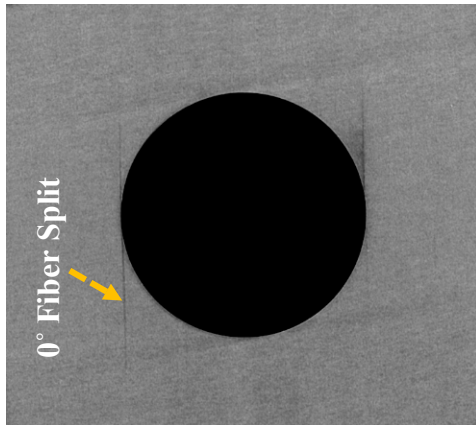
From the CA investigations carried out here, it can be noted that the primary failure mechanisms, including their initiation locations and progression rate, are highly dependent on the material system, layup sequence, and stress levels. All tension/compression failure mechanisms and their interactions captured using detailed X-CT analysis of individual plies at various inspection intervals are provided in detail in Appendix A. In addition, predominant failure mechanisms detected using detailed X-CT scans for the several CA R-ratios here are provided in Table 5.



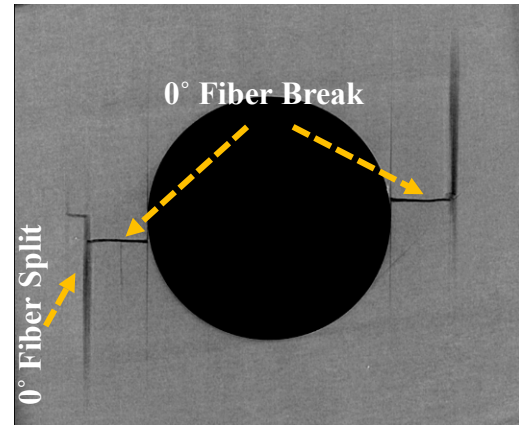
(a) Ply #1 (45°) at 10,000 cycles



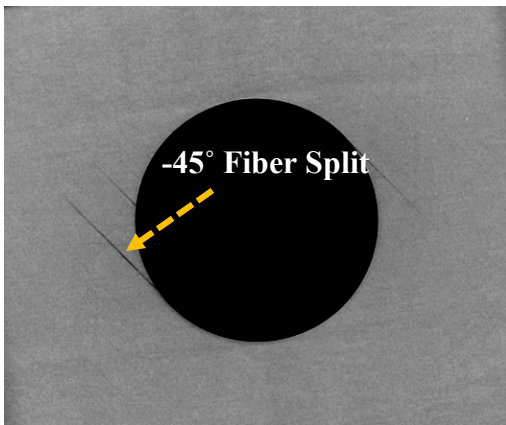
(b) Ply #1 (45°) at 25,000 cycles



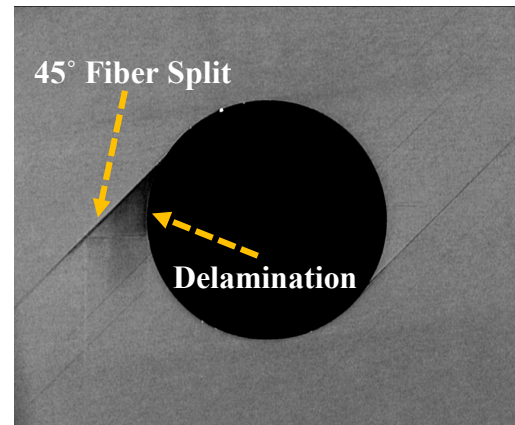
(c) Ply #23 (0°) at 25,000 cycles



(d) Ply #23 (0°) at 35,000 cycles

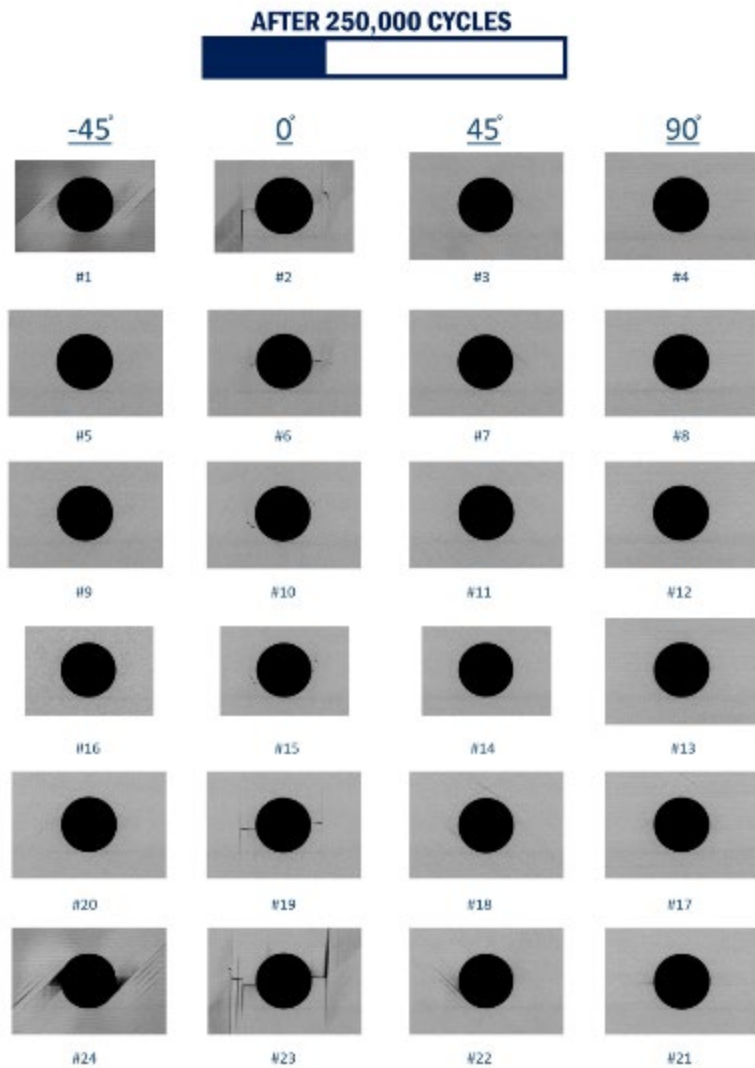


(e) Ply #22 (-45°) at 35,000 cycles

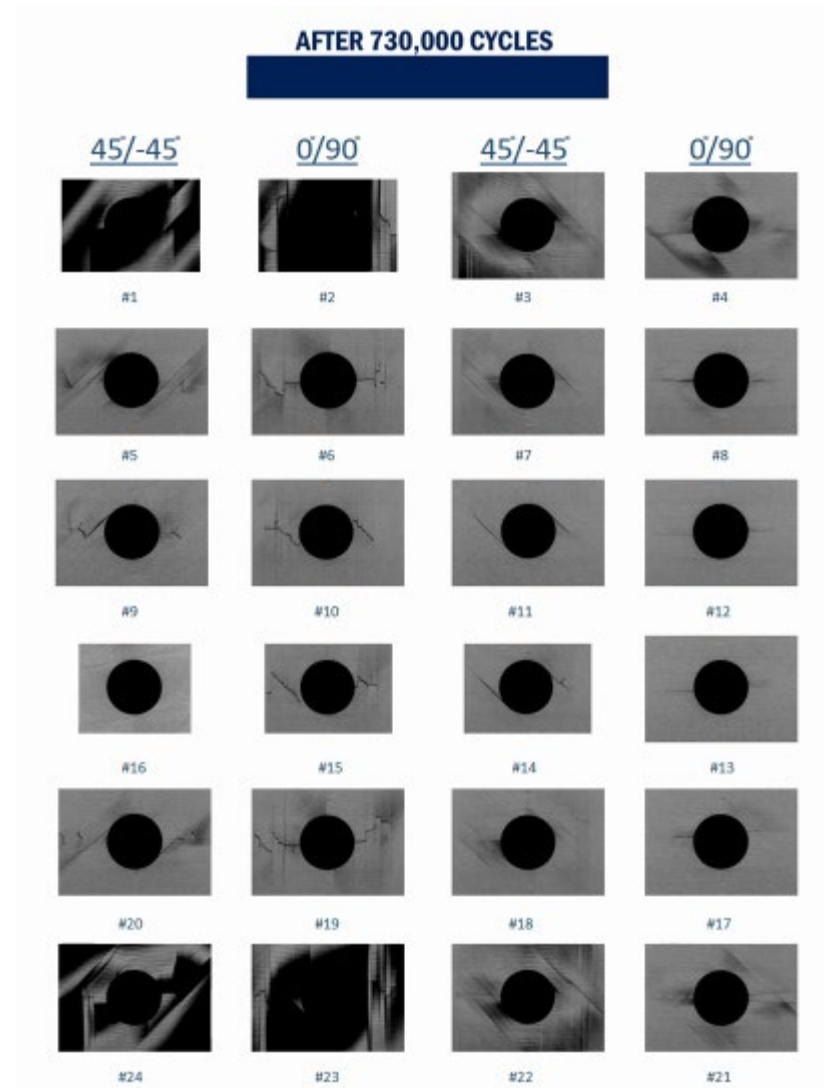


(f) Ply #24 (45°) at 40,000 cycles

Figure 21. Primary failure modes detected during constant amplitude (55% SL, $R = -1$)



(a) Ply-by-ply X-CT analysis at 250,000 cycles



(b) Ply-by-ply X-CT analysis at 730,000 cycles (before failure)

Figure 22. Failure mechanism in each ply of CA UNI-QI Specimen #17 (55% SL, $R = -1$ at 250,000 and 730,000 cycles)

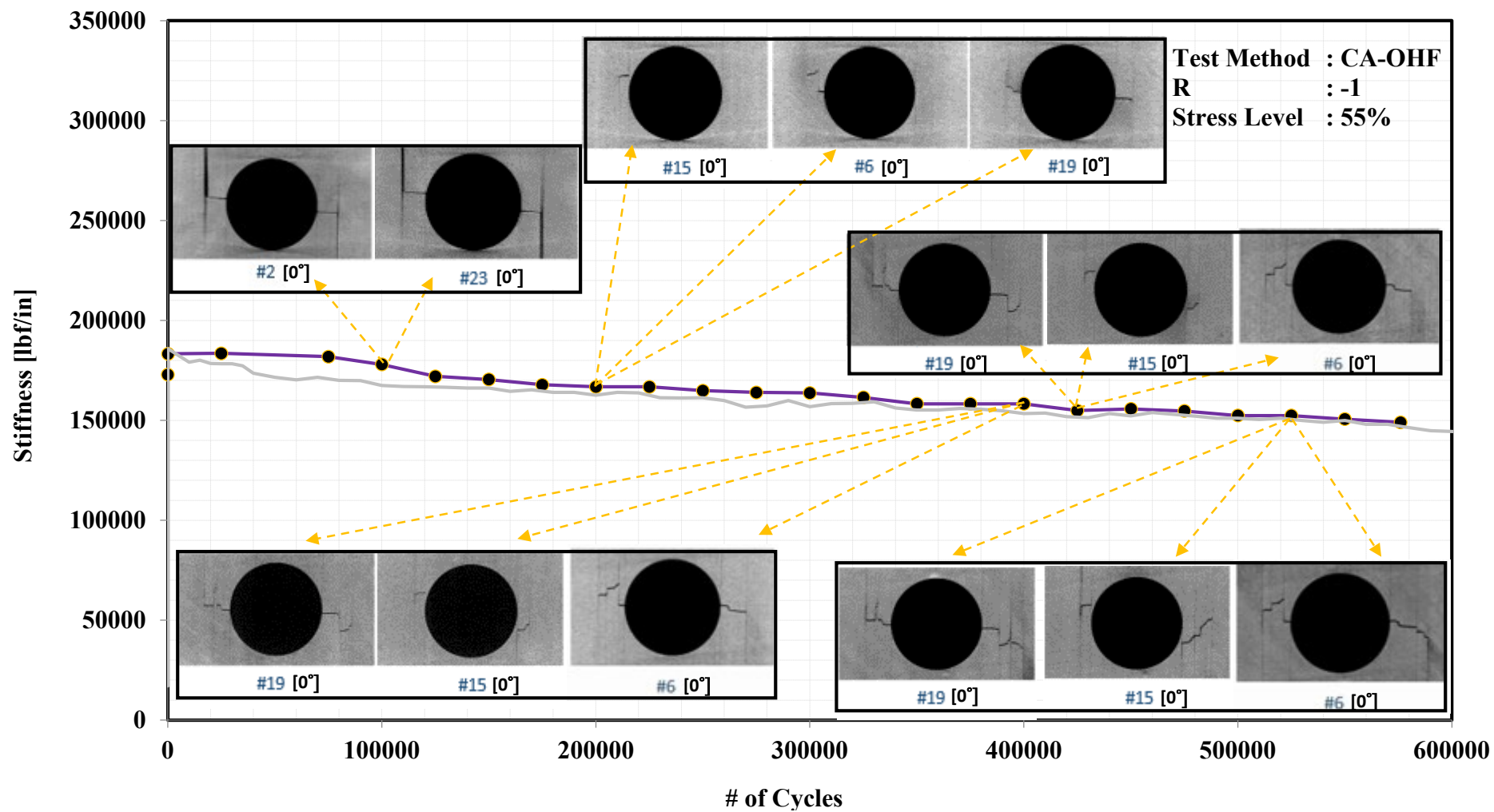
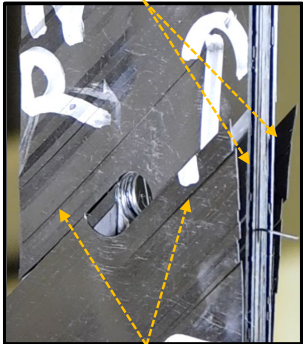
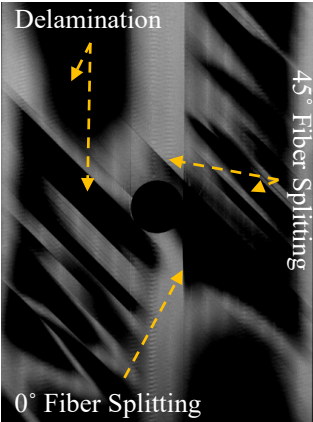
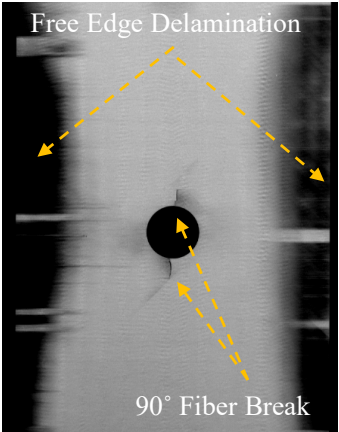
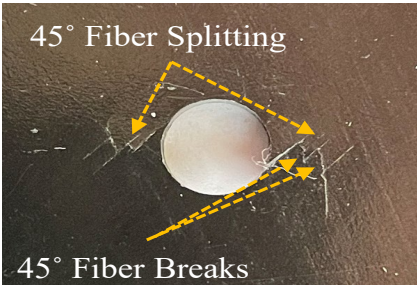
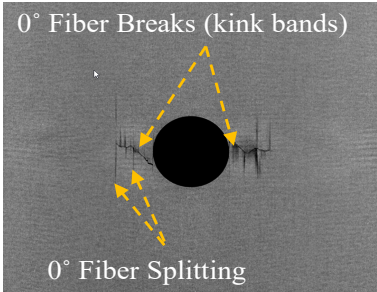
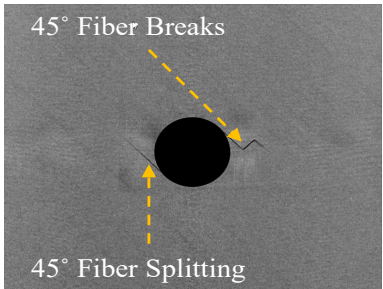
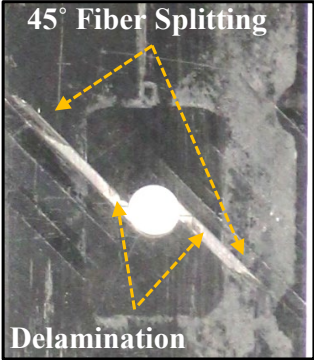
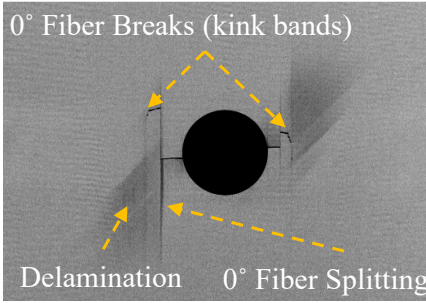
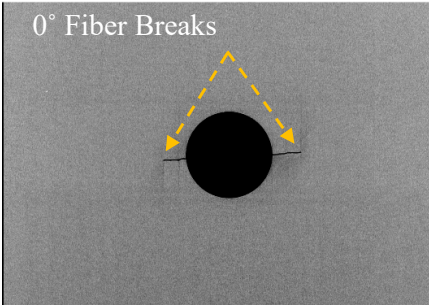


Figure 23. Stiffness degradation damage progression in multiple plies of CA OHF UNI-QI Specimen #8 (55% SL, R = -1)

Table 5. Dominant failure mechanisms in CA fatigue tests ($R = 0.1, 5$, and -1)

	Specimen	Detailed X-CT of Characteristic Damage Mechanism		Dominant Failure Mechanism
$R = 0.1$	<p>Delamination</p>  <p>45° Fiber Splitting</p>	 <p>Delamination</p> <p>45° Fiber Splitting</p> <p>0° Fiber Splitting</p>	 <p>Free Edge Delamination</p> <p>90° Fiber Break</p>	<ul style="list-style-type: none"> ▪ 90° fiber splitting ▪ 45° fiber splitting ▪ Delamination ▪ 0° fiber splitting ▪ Free-edge delamination ▪ 90° fiber breaks
$R = 5$	 <p>45° Fiber Splitting</p> <p>45° Fiber Breaks</p>	 <p>0° Fiber Breaks (kink bands)</p> <p>0° Fiber Splitting</p>	 <p>45° Fiber Breaks</p> <p>45° Fiber Splitting</p>	<ul style="list-style-type: none"> ▪ 45° fiber splitting ▪ 0° fiber breaks (kink bands) ▪ 0° fiber splitting ▪ Delamination ▪ 90° fiber splitting ▪

$R = -1$	 <p>45° Fiber Splitting</p> <p>Delamination</p>	<div data-bbox="646 185 1068 485">  <p>0° Fiber Breaks (kink bands)</p> <p>Delamination 0° Fiber Splitting</p> </div> <div data-bbox="1113 185 1539 488">  <p>0° Fiber Breaks</p> </div>	<ul style="list-style-type: none"> ▪ 90° fiber splitting ▪ 45° fiber splitting ▪ 0° fiber breaks (kink bands) ▪ 0° fiber splitting ▪ Delamination ▪ 90° fiber splitting ▪
----------	--	---	---

3.1.4 Influence of tensile fatigue on residual strength

Composite structures are extremely notch sensitive at the high-stress low-cycle regime of the SN curve. The influence of notch sensitivity on static strength in composites is shown in Figure 24 (Seneviratne & Tomblin, 2012). The OH specimen considered in this research will definitely be a subject of notch sensitivity and the associated strength knockdown. However, a separate phenomenon was investigated and presented here, wherein it was noted that a significant increase in residual strength was noted on OH specimens at various stress levels. This has profound implication from the perspective of ageing and extending service life of composite structures.

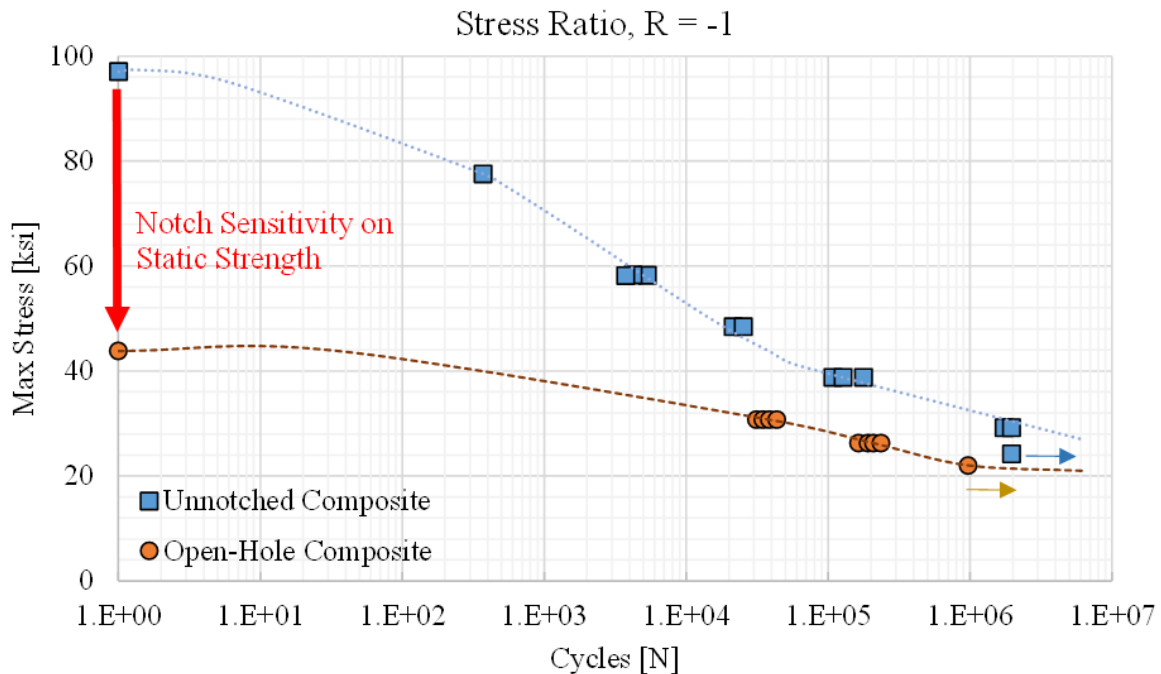


Figure 24. Static notch sensitivity in composites

Initially, residual strength assessment was carried out on runout tensile UNI-QI OH (24 ply) coupons (same material system as previous; refer to Table 3). An increase in RS was noticed on the runout tensile fatigue specimens, as shown in the SN plot in Figure 25. It was noticed that there was a 10–15% increase in tensile strength at the end of two million cycles. Intermediate NDI inspections detected most of the failure mechanisms summarized previously in Table 5. To further validate the observations, the study was further extended by performing RS assessment

on a T650/5320-1 UNI 28-ply hard layup (50/40/10) OH laminate at three distinct relatively high stress levels (70, 80, and 90% of quasi-static strength).

An overall summary of experiments conducted for the hard laminate along with the residual strength results are presented in Table 6. SN data including initial static strengths and RSs for the hard layup are also provided in Figure 26. Average values of initial static strengths (tensile and compressive) were compared against respective compressive and tensile RSs for tensile RS assessment (color-coded red diamond in SN plot, Figure 26). For compressive RS evaluations, three specimens with intermediate interruptions at 500,000, 800,000 and 1,000,000 (runout) were considered (color-coded blue diamond in Figure 26). The change in strengths for various stress levels are also summarized in Table 7.

From the side study conducted here for two different layups, it can be concluded that a notable increase of both tensile and compressive RS was observed after tension fatigue testing ($R = 0.1$). In the case of tensile RS, a significant increase of 21% was noticed, and an increase of 7% in compressive RS was observed for coupons loaded at 70% SL. Note that RS measurements were carried out after 1,000,000 tension fatigue cycles. In addition, as noted in Table 6, higher tensile RSs were obtained for higher fatigue stress levels.

At low applied stress levels, the increase in residual strength may be attributed to the stress redistribution around the hole and notch-tip blunting caused by minor fiber breaks and micro matrix cracks. Invariably, the microcracks formed at lower stress levels reduces stress concentration around the hole (Hart-Smith, 1995) and may not cause delamination. On the other hand, high stress levels are accompanied by delaminations, which should simultaneously reduce the residual strength. However, this is not the case, as was exhibited in Figure 26 for high stress level fatigue loadings are accompanied by excessive delaminations. Findings in Advanced Material Characterization and Structural Certification (AMCSC) Volume 1 of 2 (Seneviratne, Tomblin, & Walimunige, 2020) provided an explanation to this counterintuitive phenomenon using the static notch sensitivity of composite laminates.

At high stress levels, excessive delaminations in conjunction to the lowering of near notch local stiffness (due to localized microcracking) occur. As noted previously in CA tension fatigue (see section 3.1.1), excessive delamination (in addition to free-edge effect) leads to the coupon acting akin to multiple laminates bundled together. An analytical model to predict the residual strength based on resulting 0° plies were noted in (Seneviratne, Tomblin, & Walimunige, 2020) and is briefly presented here for completion.

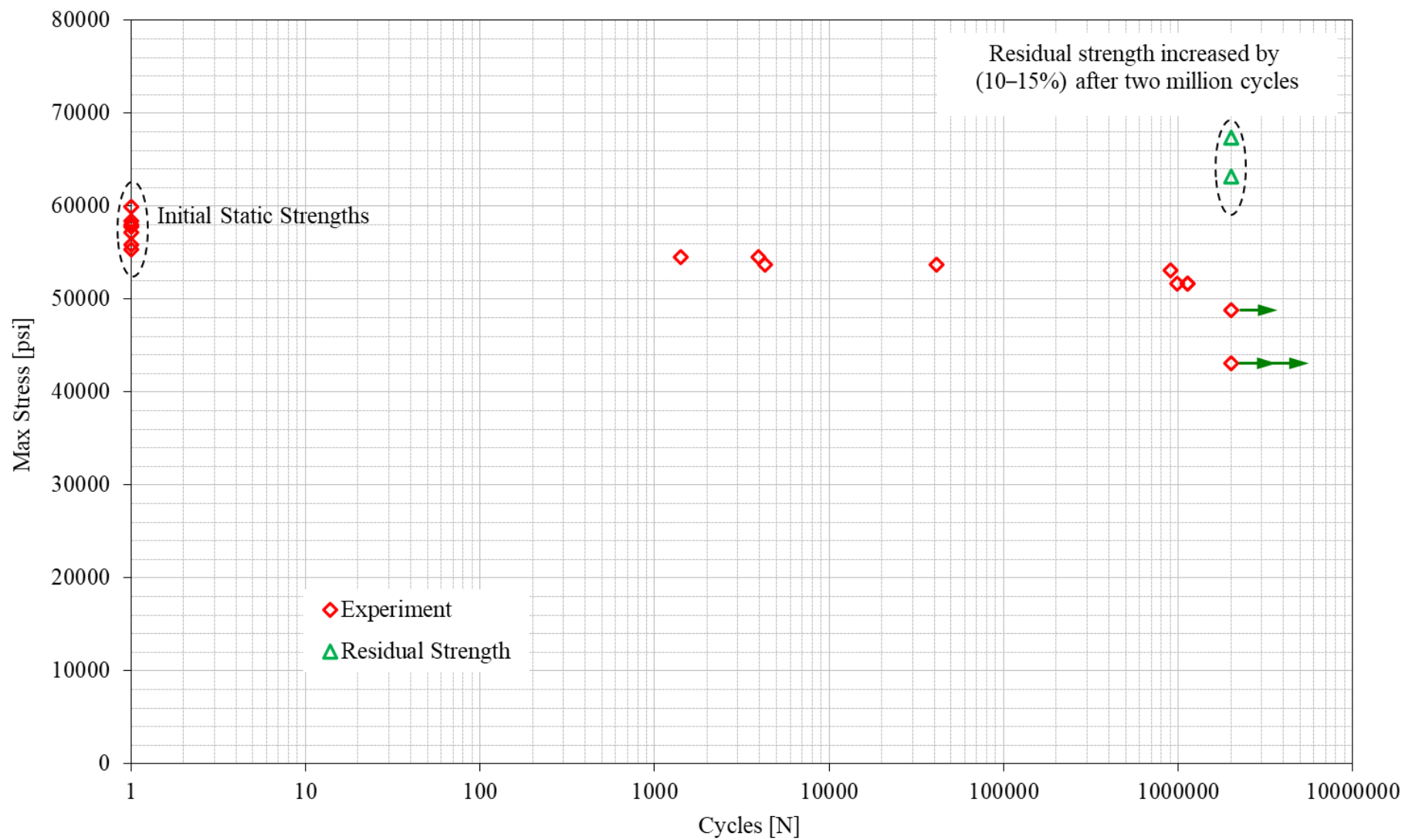


Figure 25. SN data for T650/5320-1 24-Ply UNI-QI OH (R = 0.1)

Table 6. Fatigue summary with tension/compression residual strength for IM7/5250-4 28-ply hard layup (R = 0.1)

Specimen Name	Test Method	R-Ratio	Fatigue Stress Level (%)	Fatigue Max Stress (ksi)	No. of Cycles	Residual Strength (ksi)	Comments
OH-1	OHT	0.1	70	89.0	1,000,000	155.34	Tensile RS
OH-2			70	89.0	1,000,000	152.13	
OH-3			80	101.7	1,000,000	167.02	
OH-4			80	101.7	1,000,000	174.80	
OH-5			90	114.5	1,000,000	182.71	
OH-6			90	114.5	1,000,000	173.50	
OH-7			90	114.5	1,000,000	166.21	
OH-9	OHT	0.1	70	89.0	1,000,000	-75.14	Compressive RS
OH-10			70	89.0	500,000	-82.32	
OH-11			70	89.0	800,000	-76.15	

Table 7. Increase in strength after one million cycles for IM7/5250-4 28-Ply Hard layup

	Initial Strength (ksi)	70% SL One Million Cycles (ksi)	Increase in Strength (%)	80% SL One Million Cycles (ksi)	Increase in Strength (%)	90% SL One Million Cycles (ksi)	Increase in Strength (%)
Tension	127.2	153.74	21	170.91	34.4	174.14	36.9
Compression	-69.9	-75.12	7	-	-	-	-

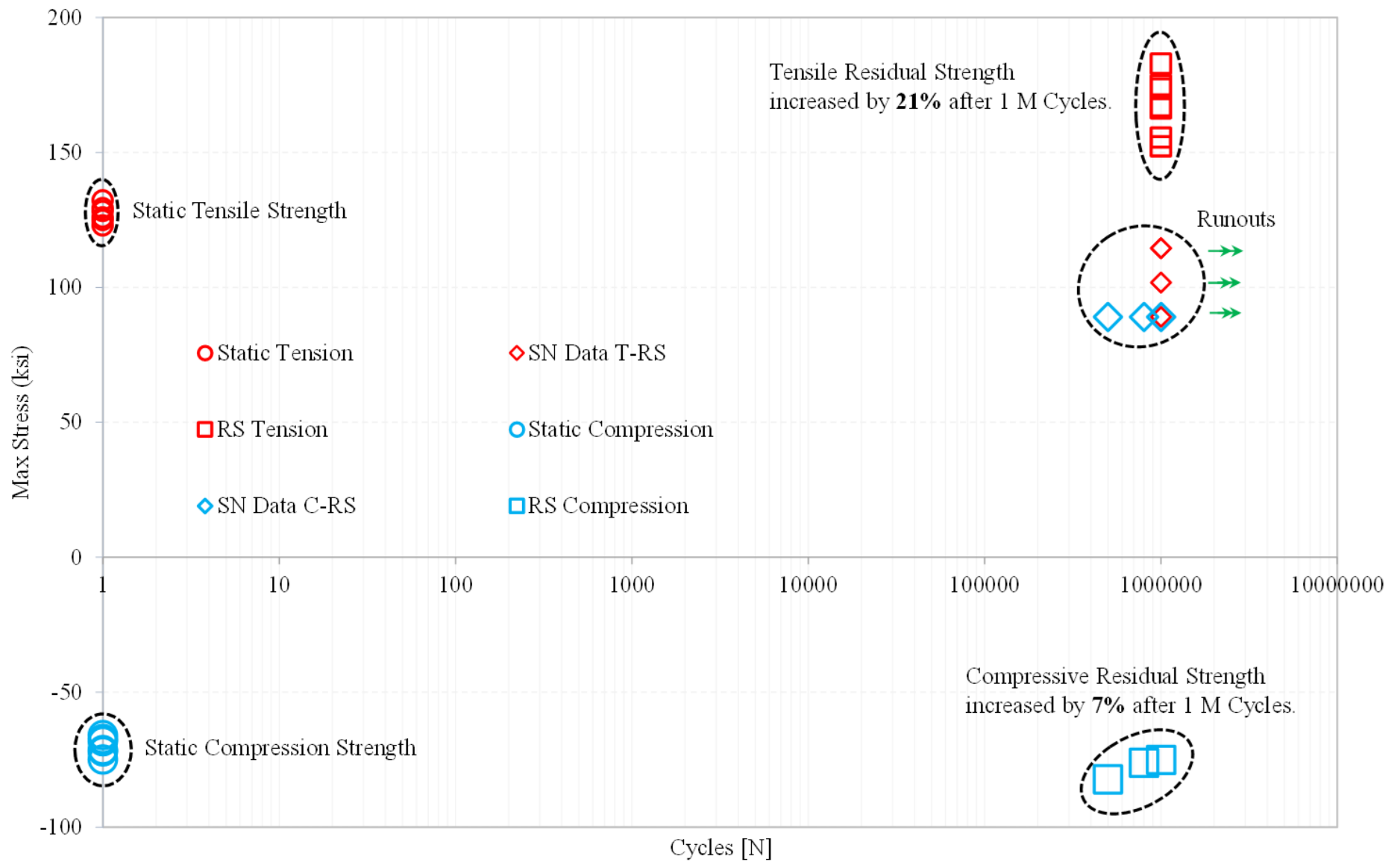


Figure 26. SN plot with tension/compression residual strength for IM7/5250-4 28-ply hard layup ($R = 0.1$)

Essentially, the increase in residual strength can be attributed to initial microcracks followed by delaminations that results in the specimen being split into three regions, as illustrated in Figure 27. During fatigue at high stress levels, most of the 90° plies followed by 45° plies are significantly damaged and overload 0° plies. At this point, significant delaminations are observed separating 0° plies from the remaining laminate. Furthermore, the fiber splits tangential to the hole that runs along the length of the specimen are observed on both side of the hole (Figure 27). The 0° plies of the OH coupon can now be considered, comprising of three distinct regions as shown: two unnotched and one notched, each with distinct width. The fiber splitting along the 0° plies divides the specimen into these columns and run parallel to the fiber direction. This separates the middle column (region 2) that includes the hole from the rest of the specimen, resulting in no continuous fibers in that region. In remainder of the specimen, however, there are two columns (regions 1 and 3) containing continuous fibers dividing the remainder of the 0° plies into two unnotched specimens (refer to inset in Figure 27). In addition, the off-axes plies (45° and 90°) also developed fiber splitting resulting in no continuous fibers in those plies. Note that at high stress levels where delaminations are prominent, the OH specimen also separates into layers (e.g., refer to Figure 11) as they have significant delaminations and interlaminar damages primarily in off-axes ply interfaces.

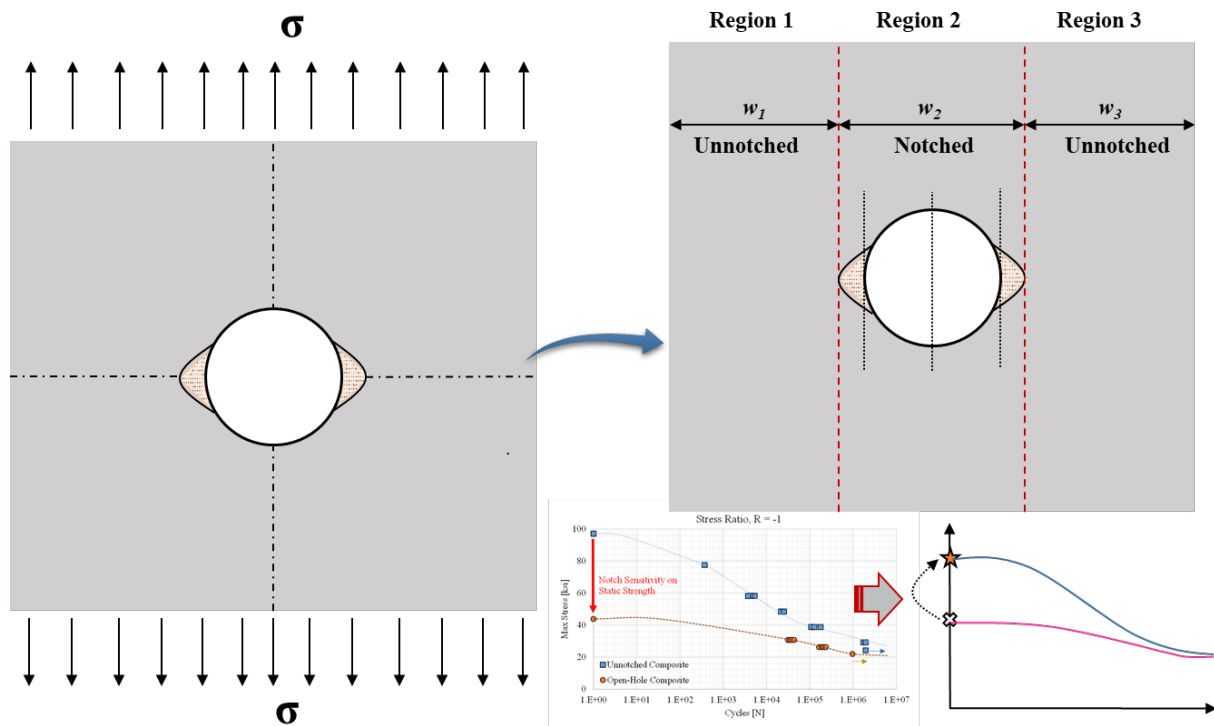


Figure 27. Schematic illustration of increase in residual strength due to localized reduction in stress concentration from fatigue exposure

Stress redistribution around the notched region occurs due to the localized microcrack formation near the hole. This localized micro-cracking is akin to the plastic zone development in metals near the hole and leads to the reduction in notch sensitivity. As loads are predominantly carried by fibers, the reduced stress concentration also prolongs the failure in tension-tension fatigue loading, resulting in an increase in RS that is proportional with the percentage of 0° plies in the coupon. As illustrated in Figure 27, 0° plies in regions 1 and 3 become the primary load-bearing members for tensile loads and behave as unnotched specimens. For composites, the quasi-static strength of unnotched specimens can be as much as twice as that of notched specimens. Hence, by assuming that the 0° plies in the unnotched regions 1 and 3 carry the predominant load (assuming that the region of microcracks near the hole is small), the strength of these load-bearing plies can be expressed as (Seneviratne, Tomblin, & Walimunige, 2020):

$$\sigma_{Net} = \left[\sigma^{tu} \cdot \left(1 - \frac{D}{W} \right) \right] \cdot P \quad (1)$$

where σ^{tu} is the ultimate tensile strength of the material (0° - longitudinal direction), D is the hole diameter, W is the specimen width, and P is the percentage of 0° plies which can be obtained from the laminate sizing chart (Hart-Smith L. J., 1989). For instance, $P = 0.6$, for a 50/40/10 - hard layup for IM7/5320-1 UNI material.

This increase in compressive RS may be attributed to isolated weak fiber breaks (localized micro-cracks) lowering the local stiffness near the hole, which lowers the stress concentration from the tensile fatigue exposure. The increase in strength may also have derived from the benign micro-failures (matrix cracking) that occurs in the immediate vicinity of the notched region. Although this influence might not be significant when compared to the influence of stiffness by very small amount of local weak fiber breaks, this leads to a decrease in stress concentration and consequently an increase in RS. Moreover, the highest fatigue stress level yields the greatest increase in RS, which results from the more isolated weak fiber breaks and a reduction in stress concentration around the notch region.

Note that in order to perform a comprehensive analysis and thoroughly capture the underlying mechanisms, it is required to further evaluate these effects with an expanded text matrix with high-fidelity NDI techniques. However, it can be concluded that most of the tension fatigue (< 90% SL) has a negligible impact on the fatigue life of composite structures, in addition to the tensile and compressive RSs of composite structures.

3.2 Sequencing effects—spectrum fatigue damage characterization

In a realistic flight-loading scenario, such as that of a load spectrum encountered during a typical flight mission, the occurrence of various fatigue profiles (high, low, and medium stress levels) is not sequential. During the study involving the development and validation of the strength-tracking (ST) method (Seneviratne & Tomblin, 2021), it was observed that load-sequencing effects play a vital role in residual strength degradation. A significant difference in the number of cycles until failure under high-, medium-, and low-load sequence alteration was observed. It was apparent that composite damage growth is greatly impacted by high stresses, especially the occurrence sequence of high stress among low and medium stresses. Moreover, damage initiation and subsequent progression alter with the order of load spectra, according to the manner in which it acts on the structure. Hence, it is vital to understand the damage mechanisms occurring under various load-sequencing scenarios.

After thoroughly documenting the damage mechanisms observed under constant-amplitude fatigue loading (refer to section 3.1), efforts were made to characterize failure initiation and its progression under variable-amplitude fatigue loading with a load-sequence alteration. High-fidelity X-CT inspections (similar to CA fatigue tests) were extended to perform damage characterization for a set of chosen load spectra and are presented here. Ultrasonic C-Scan, as well as IR thermography, were also employed. Such an analysis also paves the way for a better understanding of damage interactions as well as a comparison against well-documented CA fatigue failure modes. This study was performed on two different laminate configurations (unidirectional quasi-isotropic (UNI-QI) layup and a plain-weave quasi-isotropic (PW-QI) layup) and were comprised of three different spectrum profiles (Profiles #3, #5, and #6). A constant stress ratio ($R = -1$) was considered, and an anti-buckling fixture was employed for OH fatigue tests.

3.2.1 Effect of 24-ply laminate configuration UNI-QI

The block spectra considered to study sequencing effects are presented in Table 4 and discussed in detail here for the T650/5320 unidirectional laminate 24-Ply UNI-QI. Three different load spectra—namely Profile #3, Profile #5, and Profile #6—under a constant $R = -1$ were generated, and a detailed description is presented in Table 8. Mainly, three different load blocks—low, medium, and high—based on the corresponding percentages of averaged static strength data were arranged in three different sequences. For better identification of the low, medium, and high LBs corresponding to 40, 55, and 70% of static strength, respectively, they have been color-coded in Table 8. It can be noted that the high-stress level appears at the middle, beginning, and end of each spectrum. Hence, the damage mechanics differ in each profile and were thoroughly investigated

using non-destructive inspection methods: TTU C-Scans, IR thermography, DIC (ARAMIS v 6.3.0 User Manual, 2017), and X-CT.

Table 8. Fatigue profiles for sequencing study for 24-Ply UNI-QI OH ($R = -1$)

Stress Level	Percentage	Max/Min Stress (ksi)	No. of Cycles
SL1 (<i>Low</i>)	40	19.835	400,008
SL2 (<i>Medium</i>)	55	27.273	116,330
SL3 (<i>High</i>)	70	34.712	3,000
SL4 (<i>Medium</i>)	55	27.273	116,330
SL5 (<i>Low</i>)	40	19.835	400,008

(a) Fatigue Profile #3

Stress Level	Percentage	Max/Min Stress (ksi)	No. of Cycles
SL1 (<i>High</i>)	70	34.712	3,000
SL2 (<i>Low</i>)	40	19.835	400,008
SL3 (<i>Medium</i>)	55	27.273	116,330
SL4 (<i>Low</i>)	40	19.835	400,008
SL5 (<i>Medium</i>)	55	27.273	116,330

(b) Fatigue Profile #5

Stress Level	Percentage	Max/Min Stress (ksi)	No. of Cycles
SL1 (<i>Low</i>)	40	19.835	400,008
SL2 (<i>Medium</i>)	55	27.273	116,330
SL3 (<i>Low</i>)	40	19.835	400,008
SL4 (<i>Medium</i>)	55	27.273	116,330
SL5 (<i>High</i>)	70	34.712	3,000

(c) Fatigue Profile #6

3.2.1.1 Fatigue spectrum Profile #3

The detailed spectrum for fatigue Profile #3 is presented previously in Table 8(a) and illustrated in Figure 28. A *low-medium-high-medium-low* arrangement of load blocks was chosen for Profile #3, with each stress block undergoing a predetermined number of cycles. In the schematic illustration provided in Figure 28, the amplitude and number of cycles for each block have been scaled and color-coded for a better visual representation of the entire stress profile. In Profile #3, the high LB (70% SL) was sandwiched between two medium LBs (55% SL). A 40% SL was utilized as a low LB at the beginning and end of the spectrum.

TTU C-Scan and IR thermography inspections were performed at the end of each load block to examine the damage accumulation within each block of the spectrum. Although these NDI methods predominantly capture delamination better, they were utilized on all specimens. Both TTU and IR scans capture delamination around notched areas that mask other damage modes. Therefore, detailed X-CT ply-by-ply analysis was conducted on one specimen for each spectrum profile, and critical damage modes observed mainly in the load-bearing 0° plies were investigated.

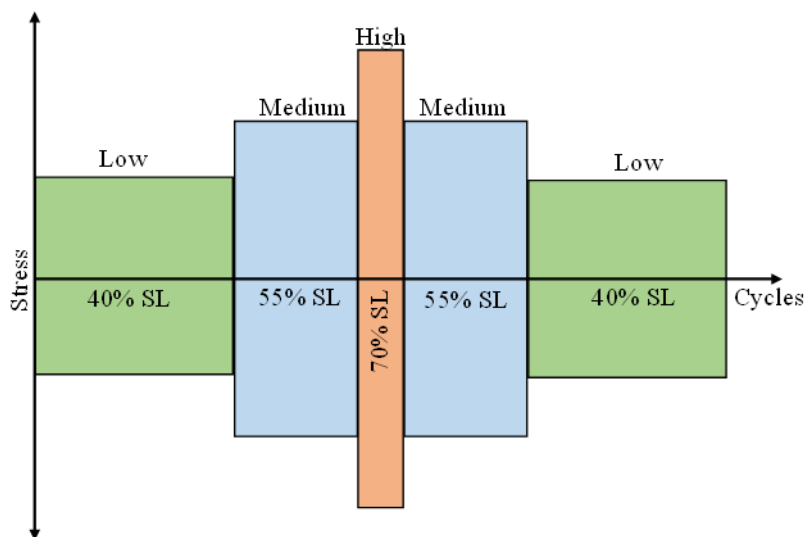


Figure 28. Fatigue spectrum for Profile #3 (*low-medium-high-medium-low*)

Primary damage mechanisms such as fiber splitting (matrix cracking) and fiber breakage were clearly noted. Damage initiation and progression were governed by the sequence of load blocks. In Profile #3, the high LB was in the middle; hence, the specimens underwent a gradual increase and decrease in stress levels. A detailed ply-level analysis at the end of each LB is presented in

Figure 29. As can be seen, at the end of the first LB (*low*), X-CT analysis did not reveal any critical damage accumulation. It is safe to state that micro-cracking did initiate around the notched region, as the first LB underwent 400,000 cycles. However, the scan at the end of the second LB (*medium*) revealed the presence of fiber splitting along the direction of the 0° fibers and the outermost 45° plies. In addition, fiber breakage of the 0° ply (emanated from the notch) was also noted. These failure mechanisms were pronounced at the end of the third LB (*high*), although the high LB underwent only 3,000 cycles. Additional fiber breakage and fiber splitting were observed at the end of this high LB, which ran at 70% SL. The damage characteristics observed here are akin to the CA fatigue case of $R = -1$. However, damage mechanics are influenced by the spectrum profiles due to the effect of load sequencing.

Two specimens underwent the full spectrum, while two specimens failed in the third LB (*high*). At the end of the fourth block, at the medium-stress level of 55%, the existing damages were observed to have saturated. There was no significant damage increase in the load-bearing 0° plies; however, the outer 45° plies were observed to be damaged due to delamination and fiber splitting. This may be attributed to the final LB, which underwent 400,000 cycles. A stiffness degradation map against the number of cycles along with detailed X-CT ply analysis is shown in Figure 30. A characteristic kink in the SD plot at the end of the third LB (*70% SL-high*) was observed. This can be attributed to fiber breaks associated with load-bearing 0° plies. Note that minimal damage progression was observed during the decrease in stress levels after the third LB (*high*) in Profile #3. It is evident that the transition of stress levels from *high-low* or *low-high* significantly influences damage initiation and the rate of damage progression.

Ply #	Load Block# 1 SL - 40% N = 400010 Cycles	Load Block# 2 SL - 55% N = 116330 Cycles	Load Block# 3 SL - 70% N = 3000 Cycles	Load Block# 4 SL - 55% N = 116330 Cycles	Load Block# 5 SL - 40% N = 400010 Cycles
# 1 [45°]					
# 2 [0°]					
# 6 [0°]					
# 10 [0°]					
# 15 [0°]					
# 19 [0°]					
# 23 [0°]					
# 24 [45°]					

Figure 29. X-CT images showing damage progression in selected plies at end of each load block for spectrum Profile #3

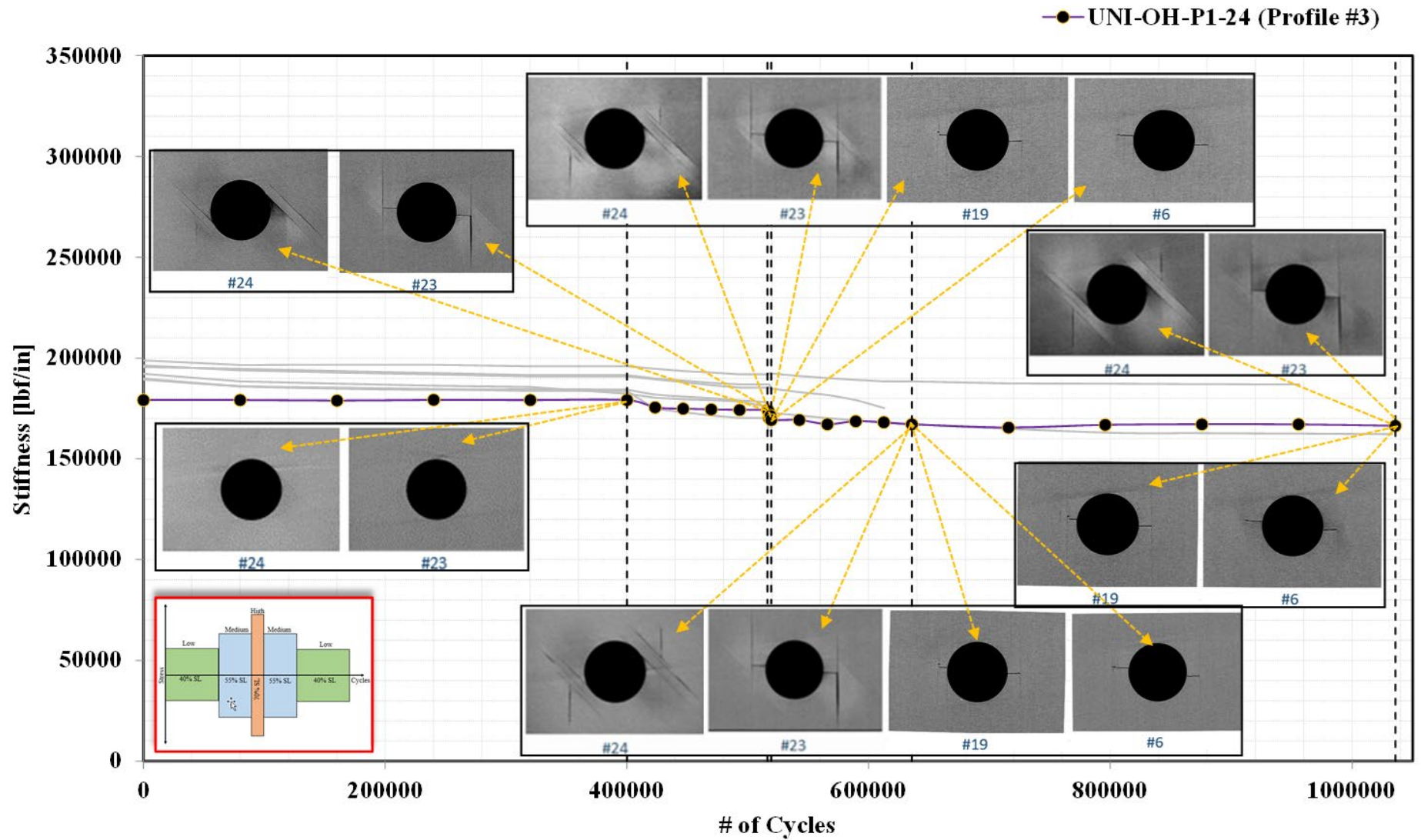


Figure 30. Stiffness degradation vs. number of cycles for UNI-QI OH spectrum Profile #3 with damage progression in multiple plies ($R = -1$)

Figure 31 summarizes all NDI inspections performed during the Profile #3 (*high* LB in the middle) fatigue spectrum. Both TTU and IR scans are presented here along with the number of fatigue failure cycles. Although these scans do not capture damage characteristics, such as fiber breaks and splitting, they are extremely helpful in identifying delamination. Three specimens survived the mid-high LB, and two specimens failed in the high LB. As shown in Figure 31, at the end of LBs 2 (*medium*) and 3 (*high*), the delamination appears to be relatively stable. However, it must be noted that in this medium-high phase, fiber breakage of loading-bearing 0° plies occurred, as shown previously in Figure 29 and Figure 30. For those specimens that survived, a further increase in delamination occurred in the outermost plies after LB 3.

NAME	NDI	N = 0 - Reference	Load Block # 1 SL - 40% N = 400010 Cycles	Load Block # 2 SL - 55% N = 116330 Cycles	Load Block # 3 SL - 70% N = 3000 Cycles	Load Block # 4 SL - 55% N = 116330 Cycles	Load Block # 5 SL - 40% N = 400010 Cycles
UN-EX-7	C - Scan				Failed after 2558 Cycles		
	Thermal						
UN-EX-8	C - Scan						
	Thermal						
UN-EX-9	C - Scan					Failed after 102866 Cycles	
	Thermal						
UN-EX-10	C - Scan				Failed after 2237 Cycles		
	Thermal						
UN-OH-11	C - Scan						
	Thermal						

Figure 31. TTU C-Scan and thermal images for 24-Ply UNI-QI OH at end of each load block for spectrum Profile #3

3.2.1.2 Fatigue spectrum Profile #5

A **high-low-medium-low-medium** load block sequence was considered to generate Profile #5, wherein the high (70% SL) LB was at the beginning of the fatigue spectrum, as shown in Figure 32. For a detailed description of the block spectrum, refer to Table 8(b). Such a spectrum was

chosen to investigate the effect of load sequencing, particularly when a high LB is at the beginning. The damage mechanisms observed at the end of the first LB, despite being *high* (70% SL), were not significant. Micro-cracking around the notched region must have been initiated but did not progress in the subsequent *low* LB (400,000 cycles). Figure 33 shows a detailed ply-by-ply analysis using X-CT at the end of each LB for Profile #5.

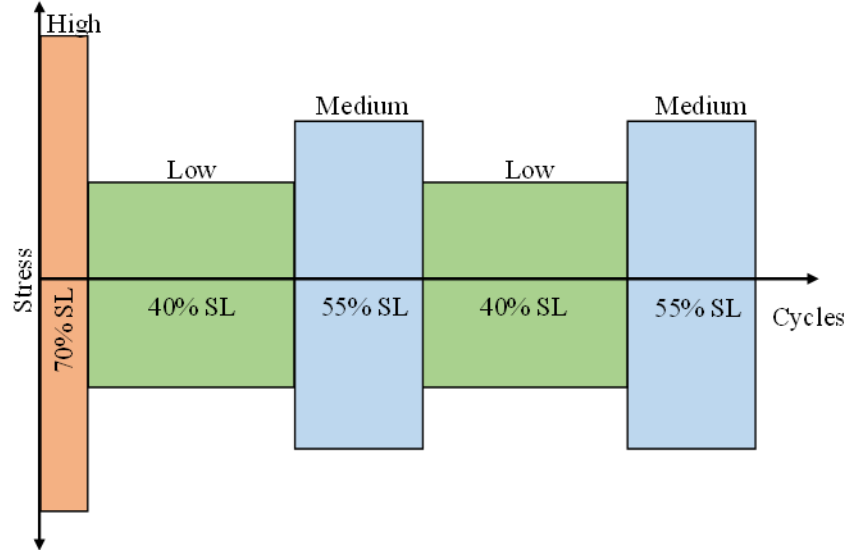


Figure 32. Fatigue spectrum for Profile #5 (*high-low-medium-low-medium*)

The absence of any dominant damage mechanisms reported earlier is noteworthy, in particular, those due to the presence of a high LB at the beginning of the fatigue spectrum. This study clearly highlights the necessity of performing a load-sequencing study. Damage initiation in terms of fiber splitting and fiber breaks in both internal 0° plies and outer 45° plies was observed at the end of LB 3 (*medium SL*, $n = 116,330$ cycles), as shown in Figure 33. This is in accordance with what was observed in the previously considered fatigue spectrum of Profile #3, where damage initiation was detected when the LB transitioned from low to medium. Therefore, it can be concluded that a combination of a low-medium LB led to maximum damage accumulation, despite being fatigued earlier with a high LB in Profile #5.

Stiffness degradation plotted against the number of cycles along with critical damage mechanisms for Profile #5 are presented in Figure 34. As noted in the stiffness degradation plot, there is a gentle decrease in stiffness through the medium LBs, with damage initiation and accumulation clearly visible at the end of *medium* LBs 3 and 5. After this third (*medium*) LB, damage initiated as fiber splits in 45° and 0° outer plies and fiber breaks on the load-bearing 0° plies, which, extended further, led to delamination in the outer 45° ply close to the notched

region. In addition to the progression of the initial damages, additional fiber splits and fiber breaks were also noted after the second LB transition from *low to medium*, as can be seen in Figure 33.

In addition, employing a high-load block at the beginning of the spectrum will also lead to the creation of damage that is not easily detectable e.g., local “weaker” fiber breaks near the hole and microcracks. As noted from the stiffness degradation plot (see Figure 34), there is a drop in stiffness after the high-load block. To detect the local microcracking due to fiber breaks, especially at the beginning of the higher load cycles (characteristic of the first load cycle), a high-fidelity inspection technique may be employed. Note that the weaker fiber breakage during early high-stress fatigue cycles is accompanied by fiber splitting (matrix cracks), which by itself is undetectable with overall specimen compliance measurements.

Figure 35 summarizes all TTU C-Scan and IR thermal inspections performed at the end of each load block for Profile #5 (high load in the beginning) fatigue spectrum. Damage accumulation in terms of delamination is more pronounced after the medium LB 3. This further corroborates the observation made earlier that the initial high LB had very little effect on damage accumulation. Significant delamination was noticed from both thermal and C-Scan images after medium LBs 3 and 5.

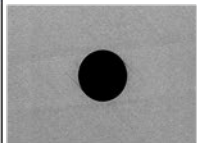
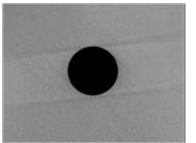
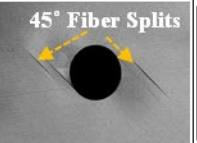
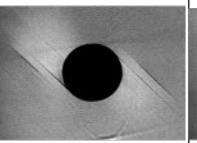
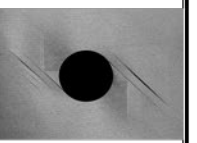
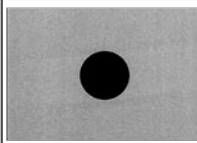
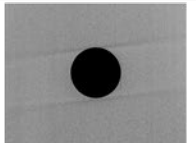
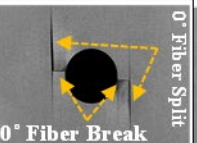
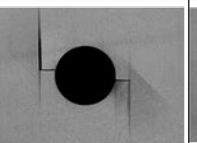
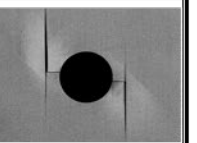
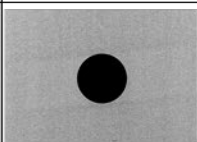
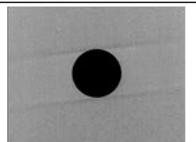
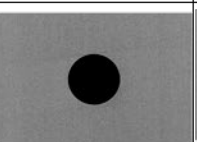
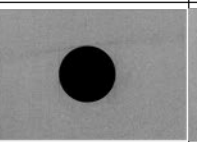
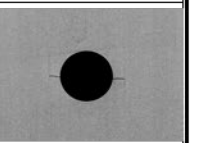
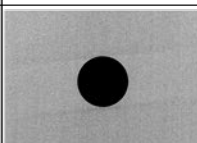
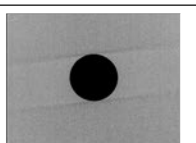
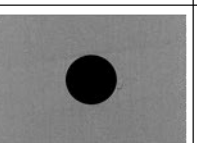
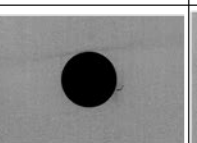
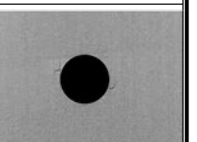
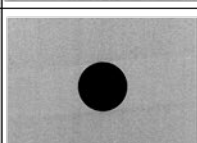
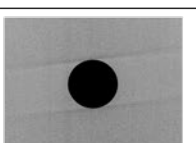
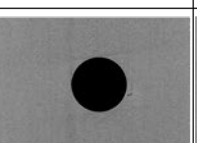
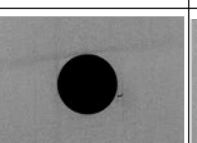
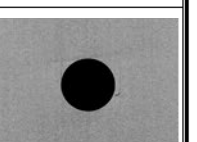
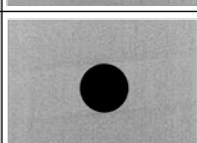
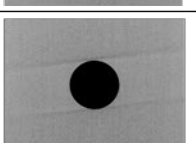
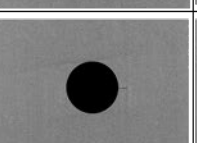
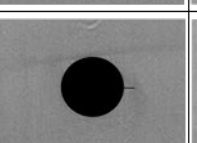
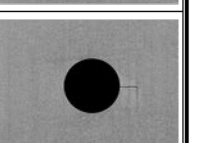
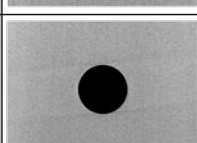
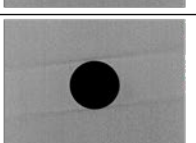
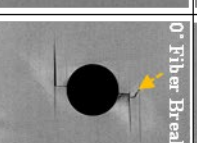
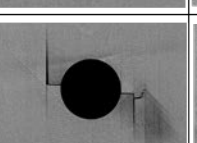
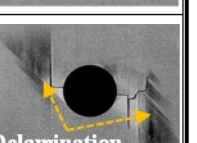
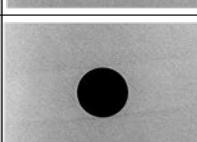
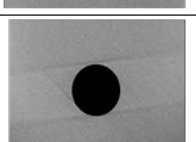
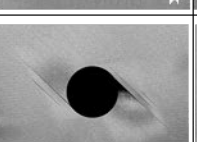
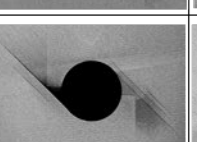
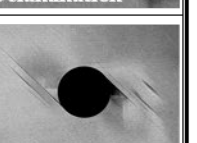
Ply #	Load Block # 1 SL - 70% N = 3000 Cycles	Load Block # 2 SL - 40% N = 400010 Cycles	Load Block # 3 SL - 55% N = 116330 Cycles	Load Block # 4 SL - 40% N = 400010 Cycles	Load Block # 5 SL - 55% N = 116330 Cycles
# 1 [45°]					
# 2 [0°]					
# 6 [0°]					
# 10 [0°]					
# 15 [0°]					
# 19 [0°]					
# 23 [0°]					
# 24 [45°]					

Figure 33. X-CT images showing damage progression in selected plies at end of each load block for spectrum Profile #5

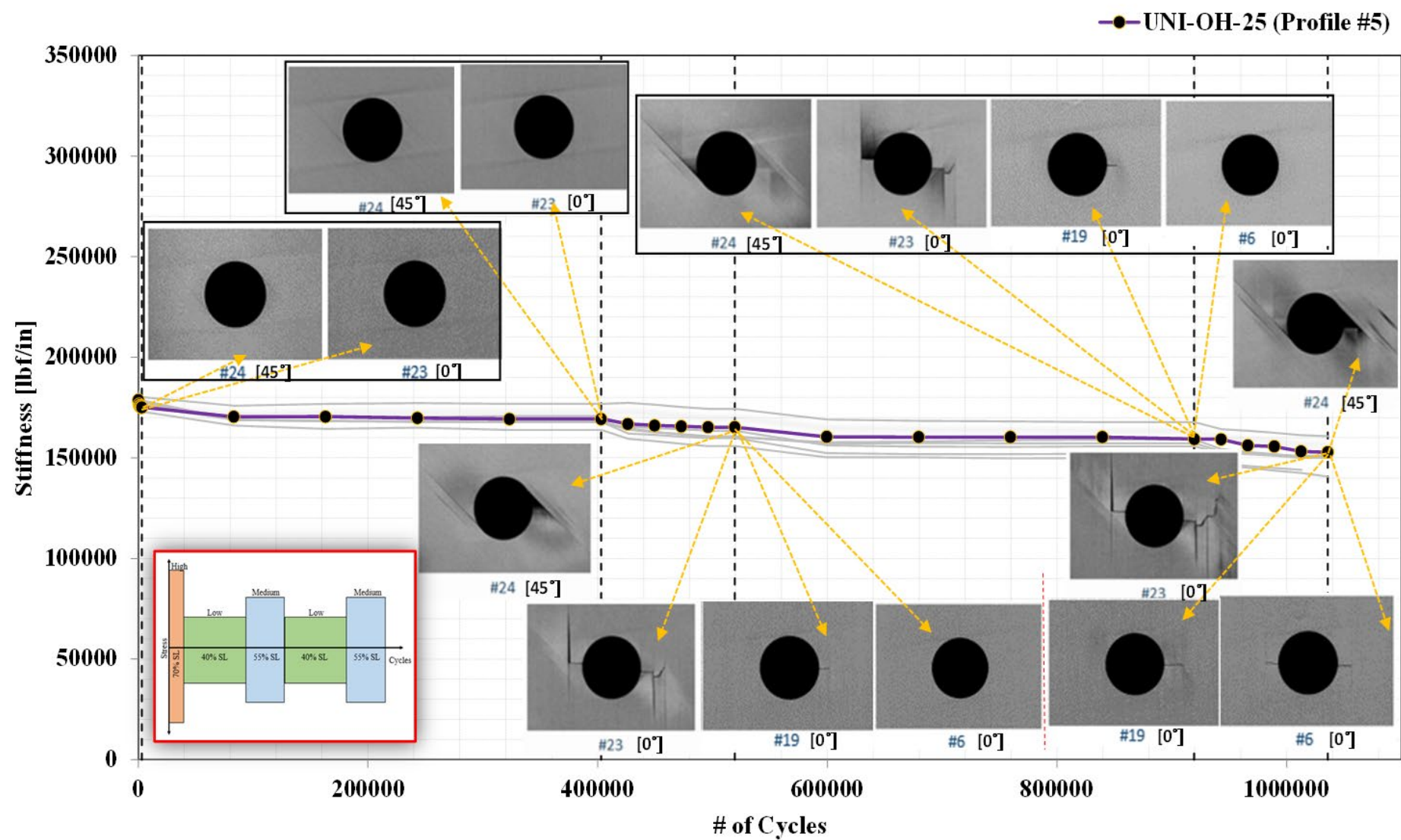


Figure 34. Stiffness degradation vs. number of cycles for UNI-QI OH spectrum Profile #5 with damage progression in multiple plies ($R = -1$)

NAME	NDI	N = 0 - Reference	Load Block # 1 SL - 70% N = 3000 Cycles	Load Block # 2 SL - 40% N = 400010 Cycles	Load Block # 3 SL - 55% N = 116330 Cycles	Load Block # 4 SL - 40% N = 400010 Cycles	Load Block # 5 SL - 55% N = 116330 Cycles
UNEX-11	C - Scan						
	Thermal						
UNEX-13	C - Scan						
	Thermal						
UNEX-14	C - Scan						
	Thermal						
UNEX-17	C - Scan						
UNI-OH-19	C - Scan						
UNI-OH-21	C - Scan						

Figure 35. TTU C-Scan and thermal images for 24-Ply UNI-QI OH at end of each load block for spectrum Profile #5

3.2.1.3 Fatigue spectrum Profile #6

After investigating the effect of a low cycle ($n = 3,000$ cycles) with a high stress load block in the beginning and in the middle of the spectrum, the study on the effect of load sequencing was extended by considering a *high* LB at the end of the spectrum. A *low-medium-low-medium-high* LB sequence was employed to generate Profile #6, wherein the high (70% SL) LB was at the end of the fatigue spectrum, as shown in Figure 36. For details on the block spectrum, refer to Table 8(b). Only two specimens in the batch survived, with the rest of them failing in the final *high* LB.

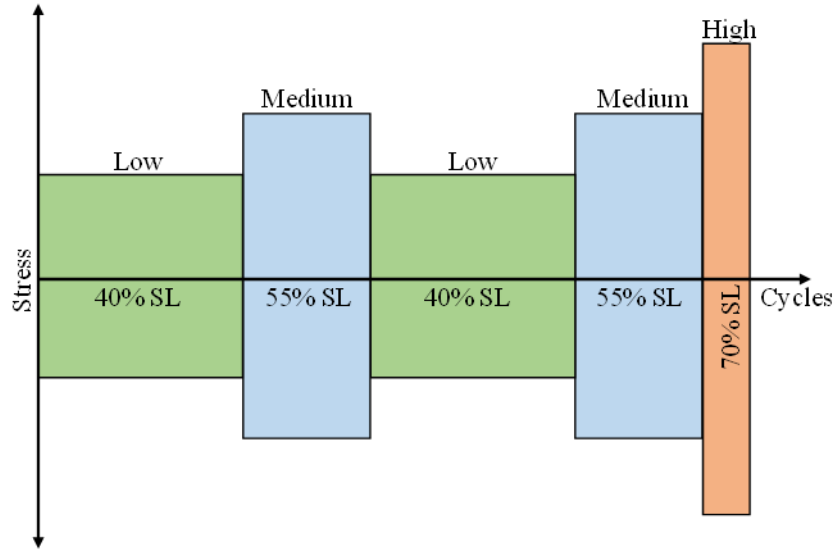


Figure 36. Fatigue spectrum for Profile #6 (*low-medium-low-medium-high*)

Damage initiation in terms of fiber breaks and fiber splitting were observed at the end of the second *medium* LB. Figure 37 shows a detailed ply-by-ply analysis using X-CT at the end of each LB for Profile #6. Similar to Profile #3 fatigue loading, at the end of the first block, barely visible fiber splitting was observed at the notch tip in the outermost plies after 400,000 cycles with 40% SL (low LB 1). However, at the end of the second *medium* LB (116,340 cycles with 55% SL), significant growth in fiber splitting and a few 0° fiber breaks were detected, as shown in Figure 37. In addition, fiber breaks and splitting occurred along the off-axis outer 45° plies around the notch.

Figure 38 summarizes the stiffness degradation for Profile #6 fatigued specimens. SD indicated that the *high* (70% SL) and *medium* (55% SL) load blocks considerably degraded the specimen stiffness (due to 0° fiber breakage), while the low (40% SL) load block showed only a negligible reduction in stiffness. For a better understanding of the damage progression, X-CT images indicating critical damage across plies were also incorporated in the SD plot. There was no indication of any damage initiation after the first *low* (40% SL) LB, even on the outer plies. However, after the second block, fiber splitting, delamination, and fiber breaks were observed in the outer plies due to the low-medium transition. In the subsequent LBs (*low-medium*), no new failure initiations or major damage progression were detected. In the fourth *medium* LB, minor fiber splitting and fiber breaks were observed. After the final *high* (70% SL) LB, extensive progression of the existing damages and critical fiber failure that initiated in the inner 0° plies were observed.

Ply #	Load Block# 1 SL - 40% N = 400010 Cycles	Load Block# 2 SL - 55% N = 116330 Cycles	Load Block# 3 SL - 40% N = 400010 Cycles	Load Block# 4 SL - 55% N = 116330 Cycles	Load Block# 5 SL - 70% N = 3000 Cycles
# 1 [45°]					
# 2 [0°]					
# 6 [0°]					
# 10 [0°]					
# 15 [0°]					
# 19 [0°]					
# 23 [0°]					
# 24 [45°]					

Figure 37. X-CT images showing damage progression in selected plies at end of each load block for spectrum Profile #6

Figure 39 summarizes all NDI inspections performed during the Profile #6 (*high* load at the end) fatigue spectrum. Except for two specimens, the others failed in the final *high* LB. For each failed specimen, fatigue failure cycles are also provided in Figure 37. A significant increase of delamination around the notched region is picked up in both thermal and C-Scan after the completion of *medium* (55% SL) LBs. The results presented here further corroborate the detailed ply-level X-CT analysis.

NAME	NDI	N = 0 - Reference	Load Block # 1 SL - 40% N = 400010 Cycles	Load Block # 2 SL - 55% N = 116330 Cycles	Load Block # 3 SL - 40% N = 400010 Cycles	Load Block # 4 SL - 55% N = 116330 Cycles	Load Block # 5 SL - 70% N = 3000 Cycles
UNI-EX-12	C - Scan						Failed after 2775 Cycles
	Thermal						
UNI-EX-15	C - Scan						
	Thermal						
UNI-EX-16	C - Scan						Failed after 472 Cycles
	Thermal			NA			
UNI-EX-18	C - Scan						Failed after 543 Cycles
UNI-OH-20	C - Scan						Failed after 2447 Cycles
UNI-OH-22	C - Scan						

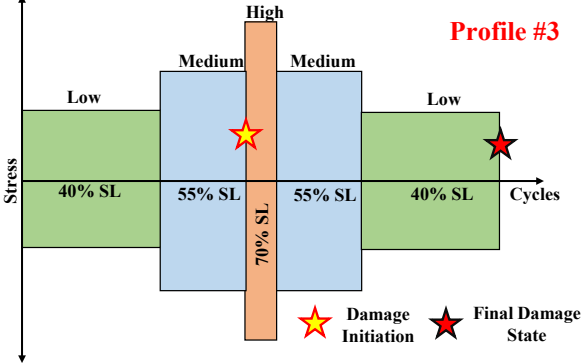
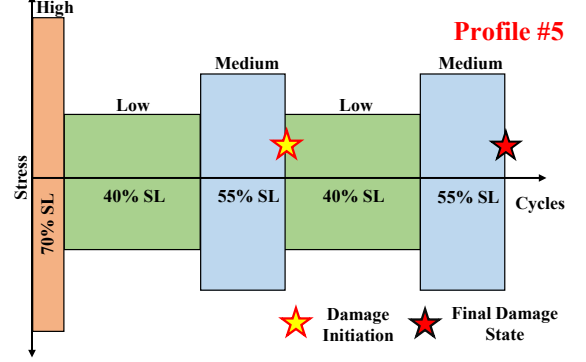
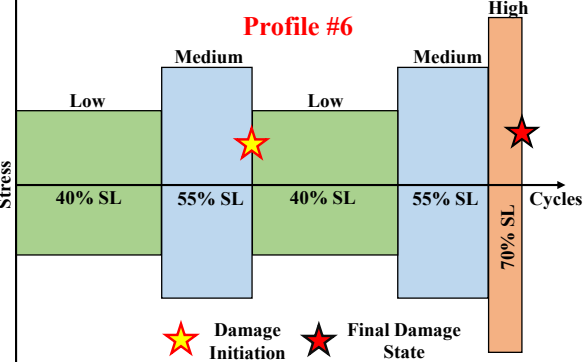
Figure 39. TTU C-Scan and thermal images for 24-Ply UNI-QI OH at end of each load block for spectrum Profile #6

At the termination of the fatigue spectrum, the surviving Profile #6 specimens showed significant damage growth in critical load-bearing plies when compared to Profile #5 specimens. However, X-CT analysis also confirmed that the severity of damage accumulation and damage progression was less when the specimen had to undergo high load at the beginning of the spectrum. This may be attributed to isolated local fiber breaks that occur around the notches under high stresses and cause redistribution and relaxation of these high stresses around the hole. This scenario protects the specimen from initiating critical failure mechanisms and thus reduces the rate of damage

progression. Microcracks will initially form at lower levels than these isolated “weak” local fiber breaks, which may be monitored by using simple local hole displacement measurements and post-test experiments.

In addition, it is evident that damage growth is significantly influenced by the load transition, because it is observed that transitioning from a *high to low* SL significantly reduced or stopped the damage growth. With SL reduction, except for the minor increase in delamination due to long fatigue cycles, there was no significant damage growth in all three-fatigue spectrums. It is also worth noting that having a *medium* load level enhanced the demonstration of load transition and sequencing effects. It is observed that the governing failure mechanisms that occurred under different load levels were unique. Moreover, in the various spectrum fatigue profiles considered here, the magnitude of damage accumulation changed due to load-sequencing effects. Load-sequencing and transitioning effects on failure initiation and progression are illustrated in Table 9. It is evident that stress level changes significantly impact damage initiation and progression. In addition, the damage progression rate changed with the load block transitions. A summary of observed damage initiation and the final damage state of coupons with fatigue Profiles #3, #5, and #6 are provided in Table 9. For detailed X-CT ply-level information along with fatigue results, including block-spectrum data and the number of failure cycles or runouts, refer to Appendix B.

Table 9. Summary of damage initiation and final damage state in critical plies for Profiles #3, #5, and #6

Fatigue Profiles	Observed Damage Initiation	Final Damage State
<p>Profile #3</p>  <p>Stress</p> <p>High</p> <p>Medium</p> <p>Low</p> <p>40% SL</p> <p>55% SL</p> <p>70% SL</p> <p>Cycles</p> <p>★ Damage Initiation</p> <p>★ Final Damage State</p>	<p>Ply # 1 [45°]</p> <p>45° Fiber Splitting</p> <p>Ply # 2 [0°]</p> <p>0° Fiber Splitting</p> <p>0° Fiber Breaks</p> <p>Ply # 6 [0°]</p> <p>Ply # 10 [0°]</p>	<p>Ply # 1 [45°]</p> <p>Delamination</p> <p>45° Fiber Splitting</p> <p>Ply # 2 [0°]</p> <p>Delamination</p> <p>0° Fiber Breaks</p> <p>Ply # 6 [0°]</p> <p>0° Fiber Breaks</p> <p>Ply # 10 [0°]</p> <p>0° Fiber Breaks</p>
<p>Profile #5</p>  <p>High</p> <p>Medium</p> <p>Low</p> <p>70% SL</p> <p>40% SL</p> <p>55% SL</p> <p>40% SL</p> <p>55% SL</p> <p>Cycles</p> <p>★ Damage Initiation</p> <p>★ Final Damage State</p>	<p>Ply # 1 [45°]</p> <p>45° Fiber Splitting</p> <p>Ply # 2 [0°]</p> <p>0° Fiber Splitting</p> <p>0° Fiber Breaks</p> <p>Ply # 6 [0°]</p> <p>Ply # 10 [0°]</p> <p>0° Fiber Breaks</p>	<p>Ply # 1 [45°]</p> <p>45° Fiber Splitting</p> <p>Ply # 2 [0°]</p> <p>0° Fiber Breaks</p> <p>0° Fiber Splitting</p> <p>Ply # 6 [0°]</p> <p>0° Fiber Breaks</p> <p>Ply # 10 [0°]</p> <p>0° Fiber Breaks</p>
<p>Profile #6</p>  <p>High</p> <p>Medium</p> <p>Low</p> <p>40% SL</p> <p>55% SL</p> <p>40% SL</p> <p>55% SL</p> <p>70% SL</p> <p>Cycles</p> <p>★ Damage Initiation</p> <p>★ Final Damage State</p>	<p>Ply # 1 [45°]</p> <p>45° Fiber Splitting</p> <p>Ply # 2 [0°]</p> <p>0° Fiber Splitting</p> <p>0° Fiber Breaks</p> <p>Ply # 6 [0°]</p> <p>Ply # 10 [0°]</p>	<p>Ply # 1 [45°]</p> <p>Delamination</p> <p>45° Fiber Splitting</p> <p>Ply # 2 [0°]</p> <p>Delamination</p> <p>0° Fiber Breaks</p> <p>Ply # 6 [0°]</p> <p>0° Fiber Breaks</p> <p>Ply # 10 [0°]</p> <p>0° Fiber Breaks</p>

3.3 Supplementary studies on sequencing effects

The fatigue spectrum profiles considered in section 0 consisted of only a single stress ratio ($R = -1$) and were performed on a 24-Ply T650/5320 UNI-QI laminate configuration. Supplementary studies were carried out to further showcase the effect that load sequencing has on damage mechanics on fatigued coupons by varying the stress levels and R-ratios. Tests were conducted for the following fatigue spectrums:

- $R = 5$ (Compression-compression fatigue spectrum with high stress levels)
- $R = -1$ (Fully reversed spectrum with high stress levels).
- $R = 5$ and -1 (Fatigue spectrum (with multiple stress ratios)
- $R = -1$ and 5 (Fatigue spectrum (with multiple stress ratios)

As stated previously, T650/5320 UNI (Quasi-Isotropic 24-Ply) was considered, and the test matrix for supplementary studies involving varying R-ratios and stress levels is provided in Table 10. X-CT was employed to perform detailed ply-level analysis in order to characterize damage initiation and accumulation in the fatigue spectrum. Detailed X-CT ply-by-ply analysis is included in Appendix C. Three specimens were tested for each fatigue spectrum. Also, in order to evaluate the sequencing effects on a different laminate configuration, a 16-Ply T650/5320 PW was also investigated. The test matrix for T650/5320-PW material configuration is provided in Table 10. The same fatigue profile as for Profiles #5 and #6 (see Table 11) was employed by modifying the number of cycles.

Table 10. UNI-QI (24-Ply) OH test matrix

Material System	Layup	Test Method	No. of Specimens	NDI
T650/5320 UNI	Quasi-Isotropic [45/0/-45/90] _{3s}	Spectrum Fatigue $R = 5$	3	X-CT
		Spectrum Fatigue $R = -1$		
		Spectrum Fatigue $R = 5$ and -1		
		Spectrum Fatigue $R = -1$ and 5		

Table 11. PW-QI (16-Ply) OH test matrix

Material System	Layup	Block Spectrum	No. of Specimens	NDI
T650/5320 PW	Quasi-Isotropic [45/0/-45/90] _{2s}	Profile #5	3	DIC and TTU
		Profile #6	3	

3.3.1 Effect of 16-ply laminate configuration PW-QI

In order to investigate the sequencing effects on a different laminate configuration, a 16-Ply T650/5320 PW-QI configuration was considered. The stress ratio was kept constant for both material systems at $R = -1$. Two different load spectra (same as UNI-QI configuration) were considered (refer to Table 4) as follows:

- Profile #5-A
- Profile #6-A

A detailed account of each fatigue profile along with number of cycles, stress level (percent of average ultimate static strength), and maximum/minimum stress are presented for the PW-QI laminate configuration in Table 12. This configuration will aid in understanding the impact that changes in the material system and layup have on the sequencing effect. For the PW-QI configuration considered here, NDI inspection techniques were limited to only TTU C-Scans and DIC (ARAMIS). Only three specimens were tested for each fatigue spectrum.

Table 12. Profiles of sequencing study for 16-Ply PW-QI OH ($R = -1$)

Stress Level	Percentage	Max/Min Stress (ksi)	No. of Cycles
SL1 (High)	70	32.413	1,040
SL2 (Low)	40	18.522	400,010
SL3 (Medium)	55	25.467	14,560
SL4 (Low)	40	18.522	400,010
SL5 (Medium)	55	25.467	14,560

(a) Fatigue Profile #5-A

Stress Level	Percentage	Max/Min Stress (ksi)	No. of Cycles
SL1 (Low)	40	19.835	400,010
SL2 (Medium)	55	27.273	14,560
SL3 (Low)	40	34.712	400,010
SL4 (Medium)	55	27.273	14,560
SL5 (High)	70	19.835	1,040

(b) Fatigue Profile #6-A

Schematic illustrations of Profiles #5-A and #6-A are provided previously in Figure 32 and Figure 36, respectively. A detailed account of stress level for the 16-Ply PW-UNI OH configuration is shown in Table 12 for both load spectra. Note that the initial high load block underwent a relatively lower number of cycles (1,048 as opposed to 3,000 cycles for UNI-QI). The PW material system demonstrated similar observations in the load-sequencing study. The fatigue profile with a high LB (Profile #5) exhibited longer fatigue life and less damage accumulation compared to Profile #6 fatigued specimens, where the high LB was at the end of the spectrum. A high load block renders reduced near-notch stress concentration due to local isolated fiber failures that are not easily detectable. As the stress concentration is reduced, it becomes tedious to accelerate fiber splitting (matrix damage) accumulating all the way to delamination propagating to the specimen free edge, which can further contribute to stiffness loss and finite width scaling issues. Alternatively, fiber splitting can also reduce the stress concentration; however, this is unlikely, particularly when there is only fiber splitting in 45° and 90° plies that have limited influence on axial stiffness.

TTU C-Scans acquired at the end of each load block are summarized in Figure 40 and Figure 41 for fatigue spectrums #5-A and #6-A, respectively. As observed in Figure 41 (Profile #6-A, high SL at the end), damage accumulation at the end of LB 3 (*medium*) indicated a higher damage state than the damage accumulated at the end of LB 4 (*medium*) in Figure 40 (Profile #5 A, (high SL in the beginning)). In addition, surviving specimens fatigued with Profile #5-A indicated less damage at the end of LB 5 (*medium*) when compared to Profile #6-A after LB 3 (*low*). At the end of LB 4 (*low*) of Profile #5-A, the specimens had been through the same LBs as Profile #6-A specimens had experienced at the end of LB 3 and an additional 1,040 cycles with 70% SL (*high*). Despite this, the damage accumulation detected in Profile #5-A fatigued specimens was far lower due to the sequencing effects.

NAME	N = 0 - Reference	Load Block # 1 SL - 70% N = 1040 Cycles	Load Block # 2 SL - 40% N = 400010 Cycles	Load Block # 3 SL - 55% N = 14560 Cycles	Load Block # 4 SL - 40% N = 400010 Cycles	Load Block # 5 SL - 55% N = 14560 Cycles
PW-OH.27						
PW-OH.1						Failed after 7903 Cycles
PW-OH.2						Failed after 12210 Cycles

Figure 40. TTU C-Scan and thermal images for 16-Ply PW-QI OH at end of each load block for spectrum Profile #5-A

NAME	N = 0-Reference	Load Block # 1 SL - 40% N = 400010 Cycles	Load Block # 2 SL - 55% N = 14560 Cycles	Load Block # 3 SL - 40% N = 400010 Cycles	Load Block # 4 SL - 55% N = 14560 Cycles	Load Block # 5 SL - 70% N = 1040 Cycles
PW-OH.3					Failed after 970 Cycles	
PW-OH.5					Failed after 8269 Cycles	
PW-OH.6					Failed after 1422 Cycles	

Figure 41. TTU C-Scan and thermal images for 16-Ply PW-QI OH at end of each load block for spectrum Profile #6-A

The effects of load sequencing investigated here for the 16-Ply PW-QI OH material configuration correspond well with the results obtained for the 24-Ply UNI-QI OH laminate considered previously in section 3.2.1. Stiffness degradation for both PW-QI OH specimens fatigued using Profiles #5 and #6 are provided in Figure 42 and Figure 43, respectively. Compared to the UNI-QI layup, the transition in stiffness from a *low* to *medium* load block is very gradual and does not involve any steep reduction in the slope. Surface strains acquired using DIC are also provided in the SD plots. Surface strain captured during fatigue Profile #6-A indicated higher strain levels compared to those of Profile #5. Higher surface strain levels can be attributed to critical internal damage mechanisms (load-bearing fiber breaks). Further studies employing high-fidelity X-ray inspections to investigate the internal failure mechanisms in PW

and other material configurations are suggested here. Surface strains acquired at the end of each LB confirmed the damage accumulation observations discussed here. As discussed previously, the initial stiffness drop for Profile #5-A (see Figure 42) in LB1 (*high*) is significant and is accompanied by fiber splitting. Although this matrix damage keeps on accumulating, as noted in Figure 42 and Figure 43, the stiffness drop remains relatively flat until 400,000 cycles (transition from *low* to *medium*), where another dramatic drop in stiffness occurs indicating the onset of compression fiber failure/kinking to a greater degree that is far more detectable.

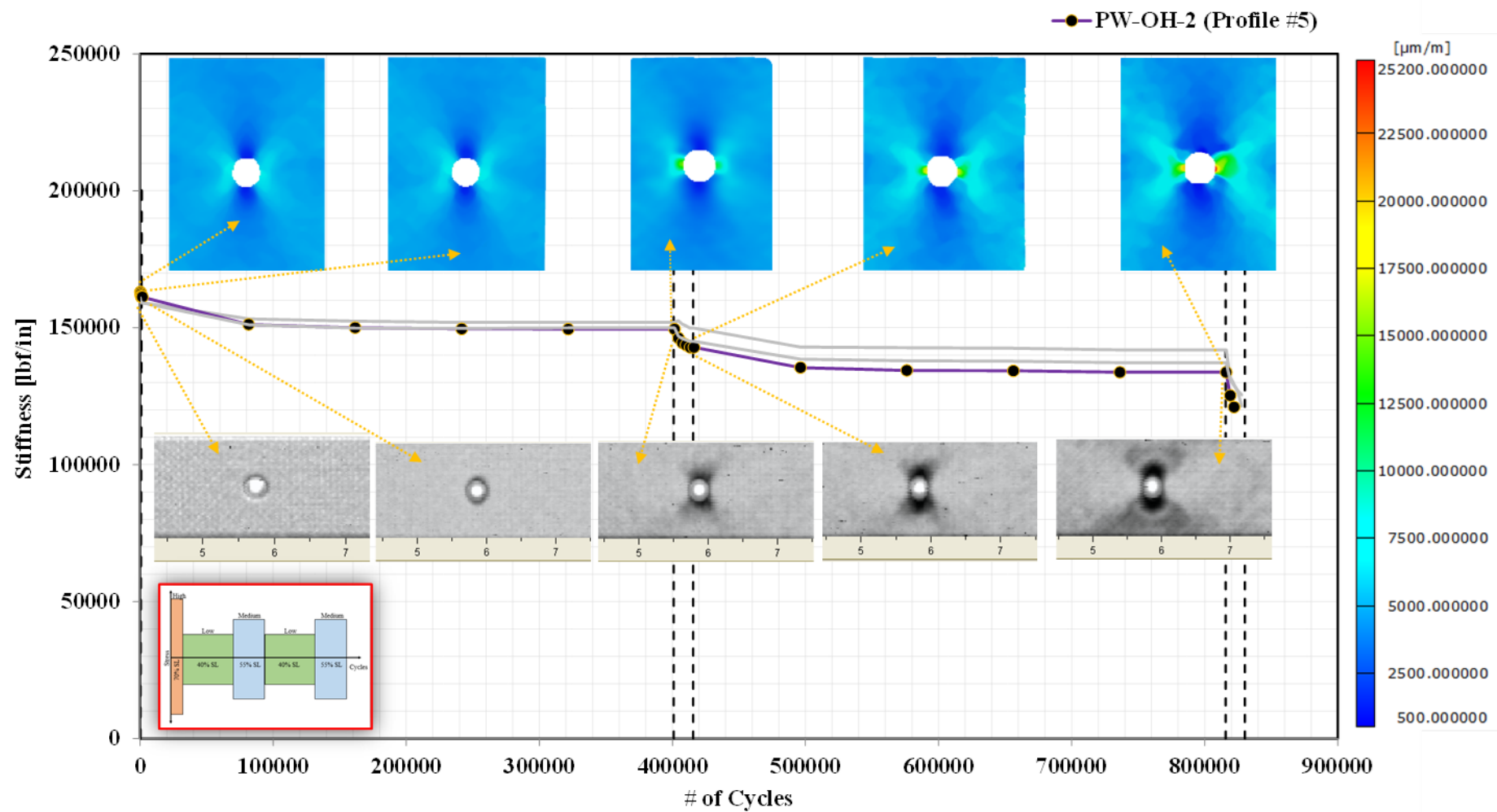


Figure 42. Stiffness degradation vs. number of cycles for spectrum Profile #5-A with DIC and C-Scan for 16-Ply PW-QI OH ($R = -1$)

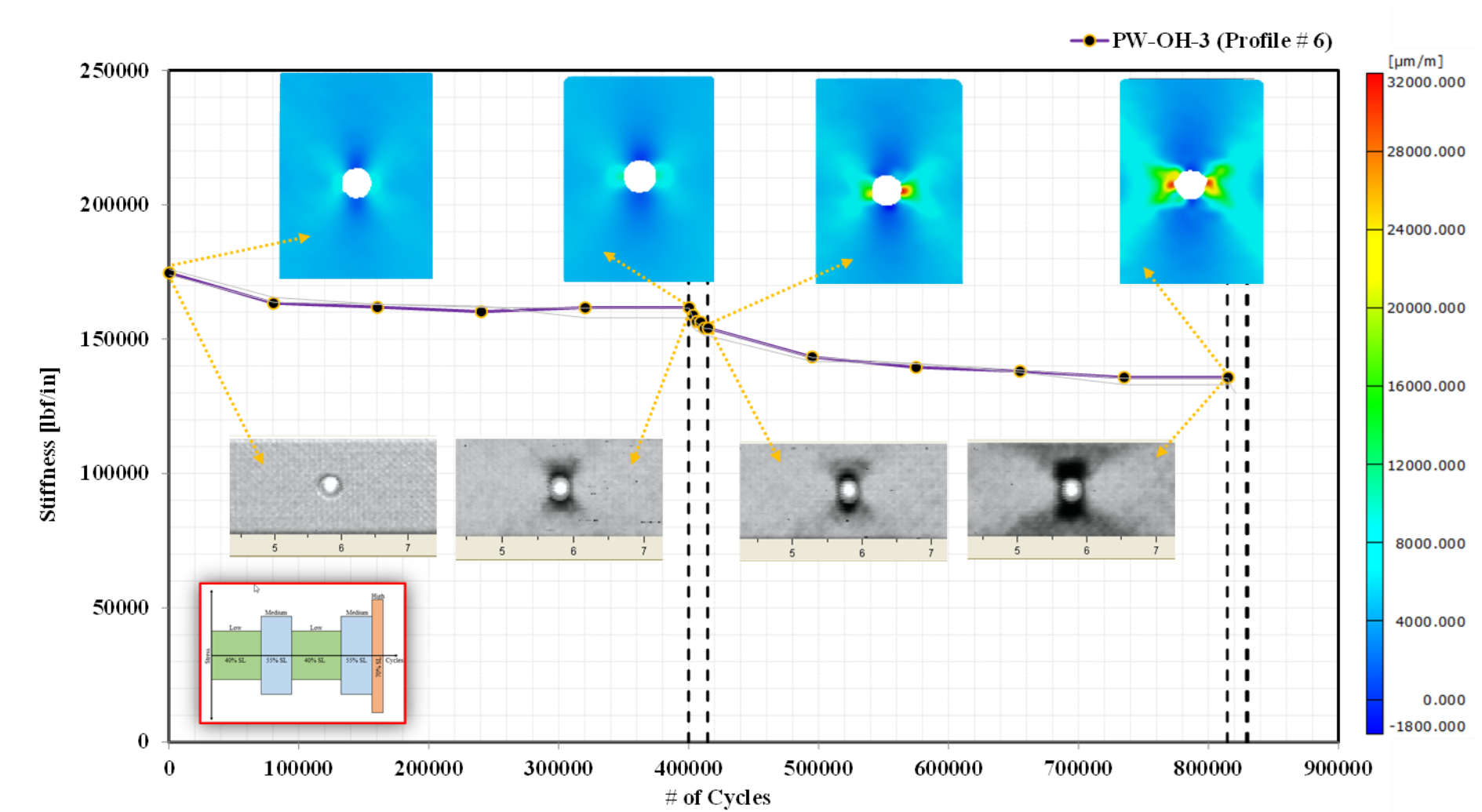


Figure 43. Stiffness degradation vs. number of cycles for spectrum Profile #6-A with DIC and C-Scan for 16-Ply PW-QI OH (R = -1)

In both 24-Ply UNI-QI OH and 16-Ply PW-QI-16 OH specimen configurations, observations of the sequencing effects were confirmed. Both fatigue tests lean towards the same conclusion that during a multi-stress level fatigue profile, having the highest load in the beginning of the fatigue spectrum allows the structure to survive longer, as opposed to having the highest load at either the middle or end. Stress levels and number of cycles in each load block are other key factors that drive sequencing effects in a fatigue spectrum. Thus, load sequencing is proven to play an important role during variable-amplitude fatigue, particularly involving high SLs. This study involving two different laminate configurations revealed the effects of load sequencing on damage initiation and progression across several fatigue spectrums.

3.3.2 Effect of stress levels: constant R-ratio spectra

Previously, load-sequencing effects were investigated on fatigue spectra at a constant R-ratio ($R = -1$), considering three unique fatigue load block spectra profiles, as shown previously in Table 4. Each fatigue profile had a unique arrangement, wherein the *high* appeared at the beginning, middle, and end of each spectrum. Previously, 70% SL was utilized for a *high* LB, 55% SL for a *medium* LB, and 40% SL for a *low* LB. In this next phase, stress levels for those three blocks were deliberately chosen to be higher. A detailed description of SLs, maximum/minimum stress, and number of cycles for both $R = 5$ (compression) and $R = -1$ (load reversal) is provided in Table 13¹ and the generated spectra for both cases schematically illustrated in Figure 44. Note that the block spectrum for $R = -1$ considered here, which is Figure 44(b), is akin to Profile #3 (refer to Figure 28). However, the *low* and *medium* stress levels were hiked to 50% and 60%, respectively. Therefore, the current analysis also paves the way for performing a direct comparison of varying stress levels on damage mechanisms for a given block spectrum.

Table 13. Fatigue profiles for sequencing study of 24-Ply UNI-QI OH with varying SL for compression and fully reversed cases

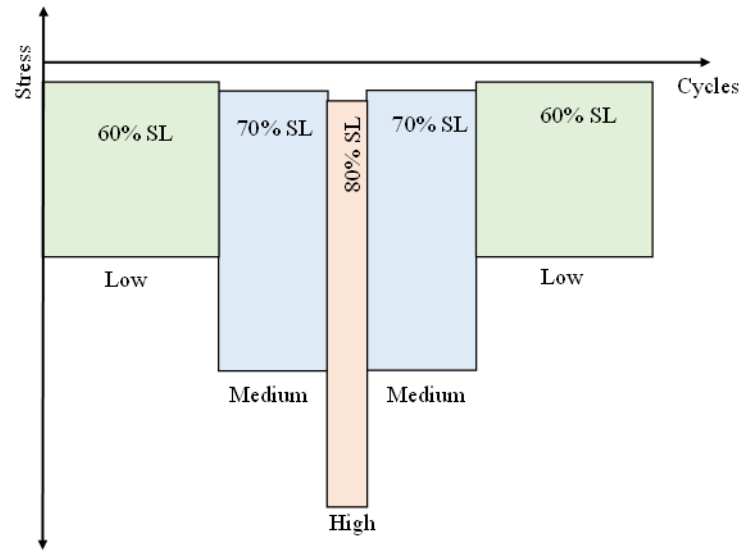
Stress Level	Max Stress (ksi)	Min Stress (ksi)	No. of Cycles
SL1 (Low-60%)	-6	-30	200,000
SL2 (Medium-70%)	-7	-35	20,000
SL3 (High-80%)	-8	-40	2,000
SL4 (Medium-70%)	-7	-35	20,000
SL5 (Low-60%)	-6	-30	200,000

¹ Note that *low*, *medium*, and *high* stress levels for $R = 5$ and $R = -1$ have been differentiated with dark and light shades to highlight the varying SL considered in both spectra.

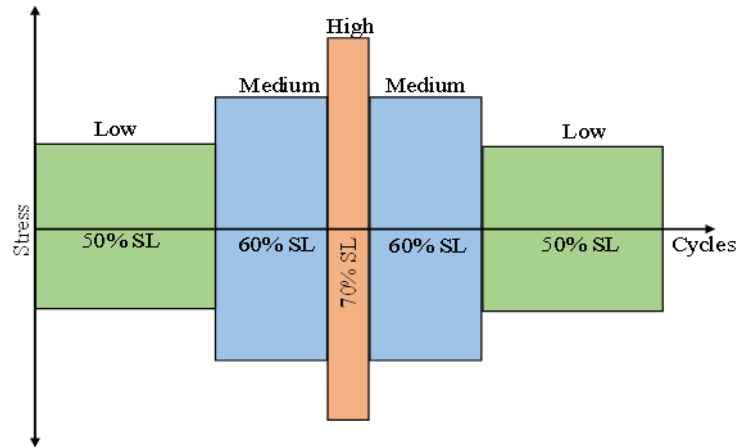
(a) $R = 5$ (compression)

Stress Level	Max Stress (ksi)	Min Stress (ksi)	No. of Cycles
SL1 (Low-50%)	25	-25	250,000
SL2 (Medium-60%)	30	-30	25,000
SL3 (High-70%)	35	-35	2000
SL4 (Medium-60%)	30	-30	25,000
SL5 (Low-50%)	25	-25	250,000

(b) $R = -1$ (load reversal)



(a) $R = 5$



$R = -1^2$

Figure 44. Fatigue spectrum profiles for load-sequencing effects under varying stress levels for constant R-ratio

For both block spectra, X-CT analysis was conducted at the end of each load block to thoroughly characterize the damage mechanisms. Specimens fatigued with spectrum $R = 5$ demonstrated similar failure mechanisms observed during the constant-amplitude compression fatigue study (refer to section 3.1.2). As noted previously, both damage mode transition and growth rates were dependent on the stress level, sequence of their occurrence, and transition state (low-high or high-low). Stiffness degradation was also measured and employed to correlate observed damage

² Spectrum is similar to Profile #3; however, *low* and *medium* load blocks correspond to 50% and 60% SL, respectively.

characteristics at the end of each LB for each fatigue spectrum. Figure 45 shows the SD plotted against number of cycles for $R = 5$. Barely visible cracks (fiber splits) in the outermost 45° ply were noted at the end of the second LB (medium SL). The final damage state at the end of LB 5 is very similar to a CA compression fatigued specimen (Figure 16(b) and #23 (0°) in Figure 45). However, at the end of third LB (high SL), fiber splitting and fiber breaks occurred in the outer plies. In addition, barely-visible fiber splits were observed in the load-bearing 0° plies (see Figure 45).

Stiffness degradation vs. number of cycles for the modified spectrum Profile #3 ($R = -1$) is provided in Figure 46. Detailed X-CT images of critical plies indicating damage accumulation at the end of each LB are also included in the plot. Note that for this modified spectrum with $R=-1$, the specimens underwent fewer cycles than specimens fatigued with Profile #3. Although the first low LB in the modified spectrum underwent half the number of cycles compared to Profile #3, due to the higher stress level, significant damage accumulation was noted at the end of LB 1. Fiber splitting along 0° and 45° outer plies was observed, along with fiber breakage and delamination. This observation clearly emphasizes the influence of stress level on load-sequencing effects.

For the modified Profile #3 spectrum with $R = -1$, fiber breakage in the load-bearing inner 0° plies was observed at the end of LB 2 (medium SL). Moreover, the damage modes in the outer plies noted in the previous LB were exacerbated (see LB 2 in Figure 46). At the end of the mid-high LB, significant delamination in the outer plies and an increase in fiber breakage and splits among inner plies were noticed. As the load transitioned from higher to lower LBs, the damage growth was significantly reduced. In general, for the fully reversed modified spectrum, the observed damage-growth characteristics are similar to those in the previously considered spectrum Profile #3. However, damage initiation and subsequent progression were found to be governed by stress levels. In contrast, for the compression-fatigued specimens ($R = 5$), the impact of stress level on damage growth is minimal. A comparison of critical damage initiations observed for both constant R-ratio fatigue profiles with higher SL is shown in Figure 47.

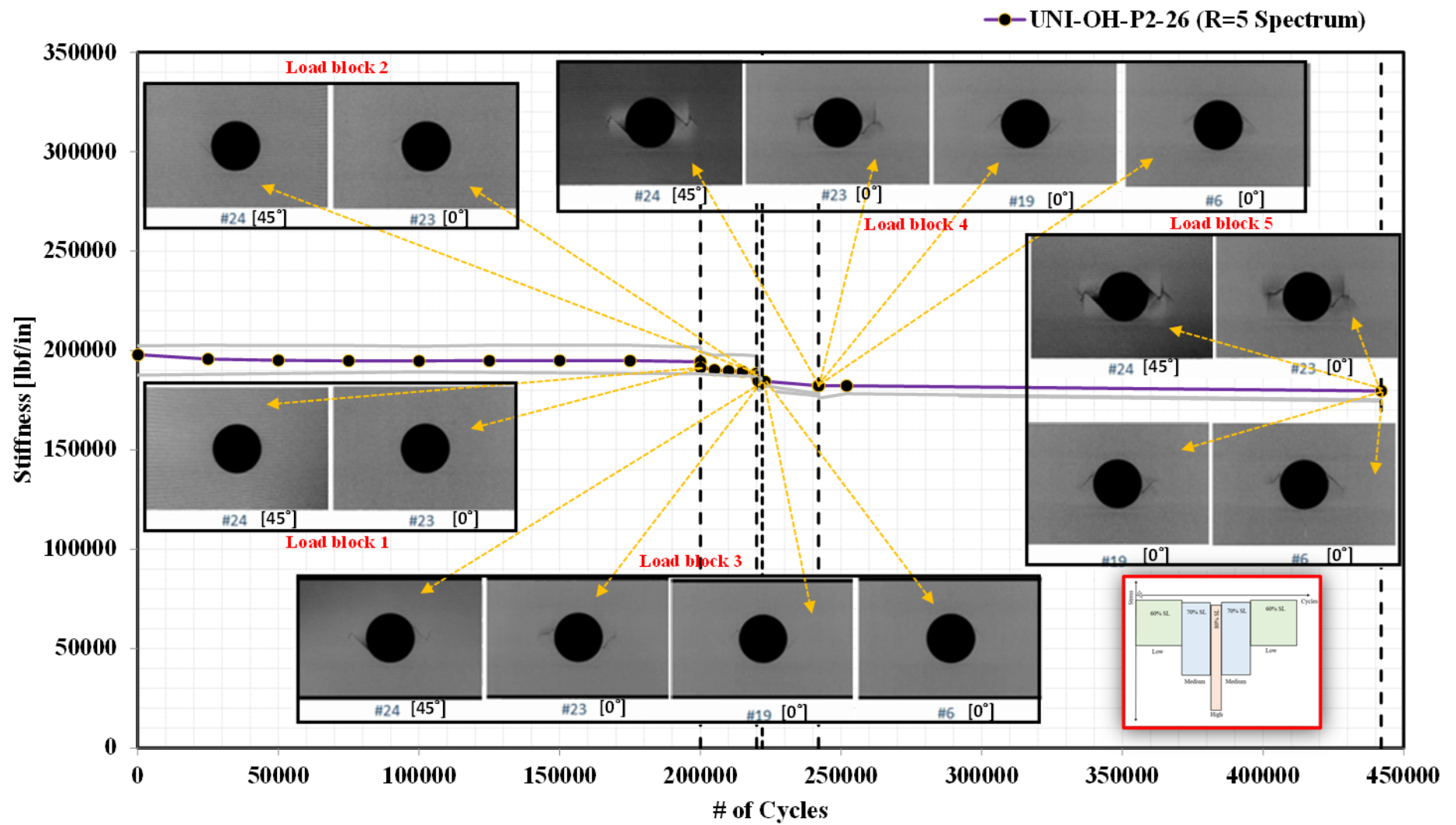


Figure 45. Stiffness degradation vs. number of cycles for UNI-QI OH with damage progression in critical plies (R = 5 spectrum)

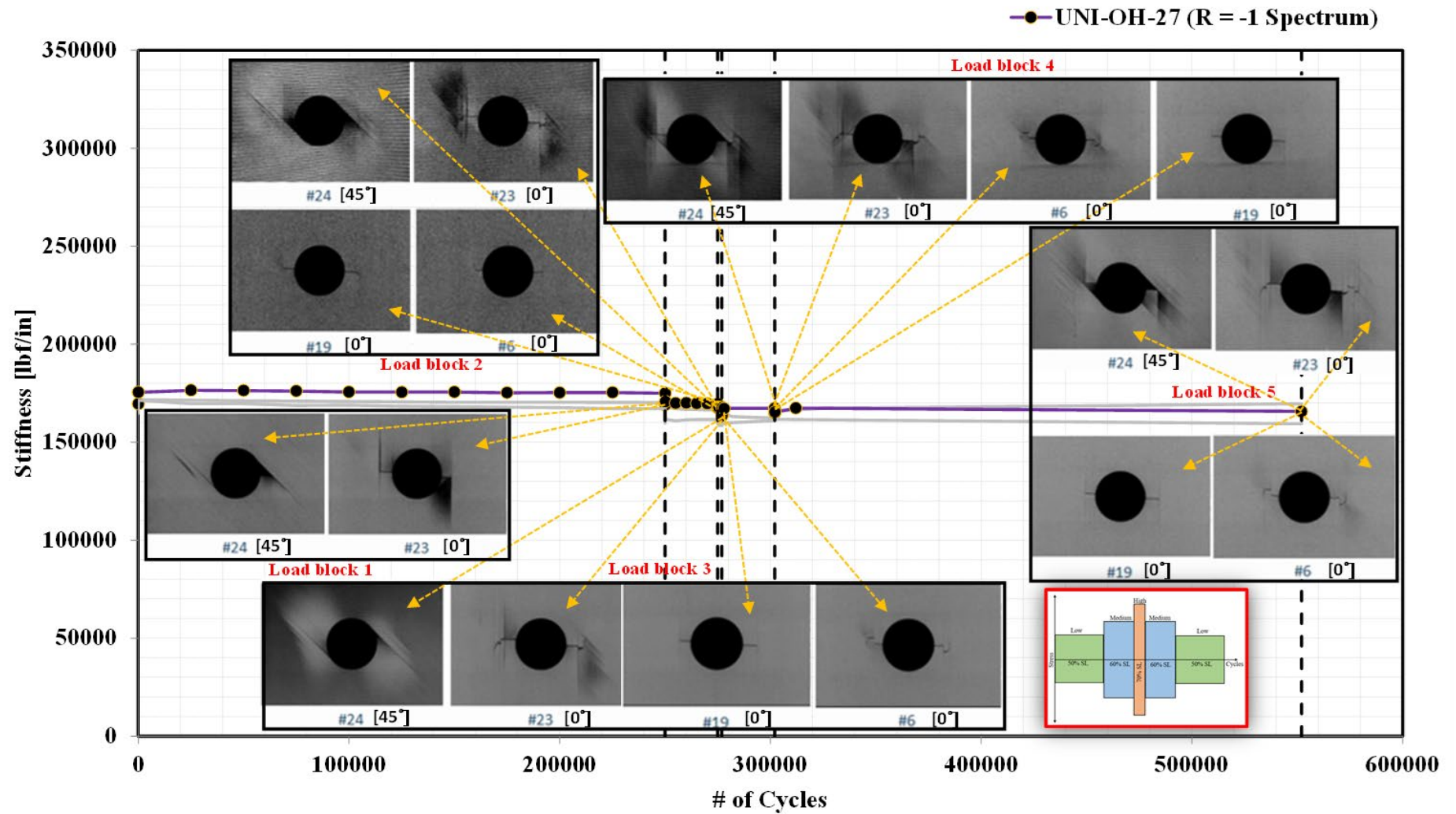
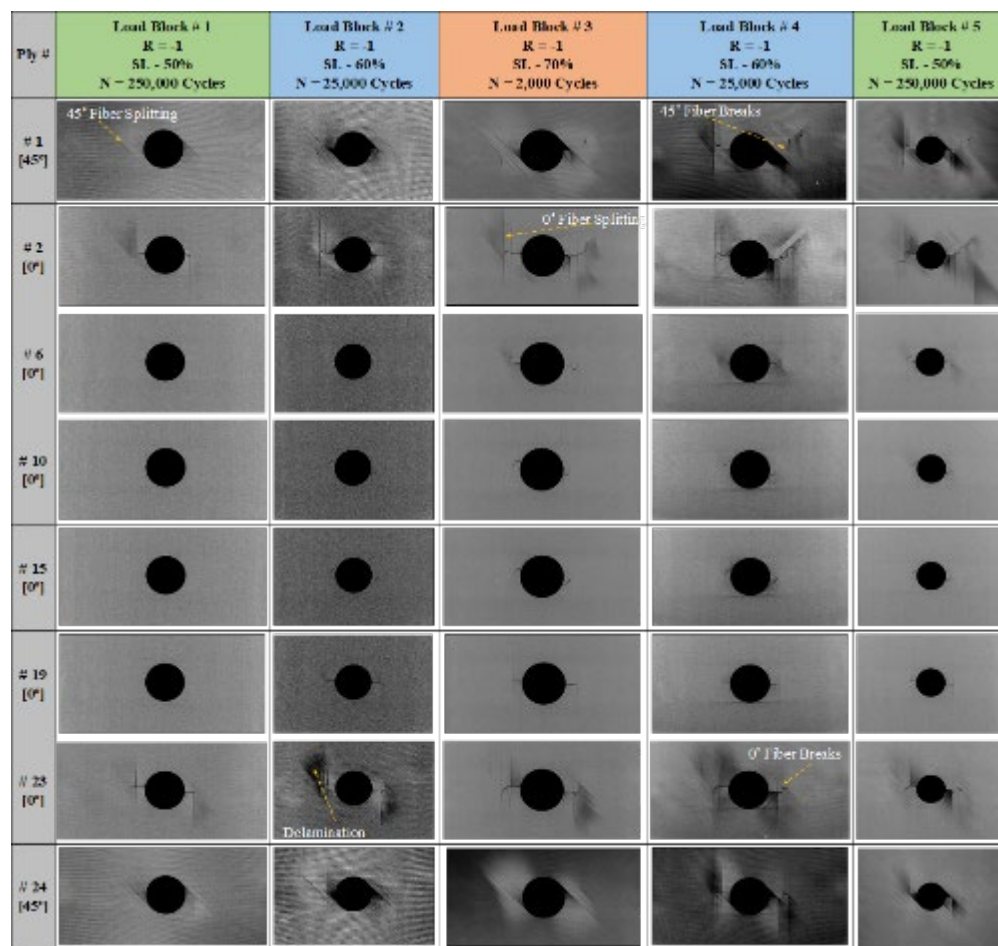
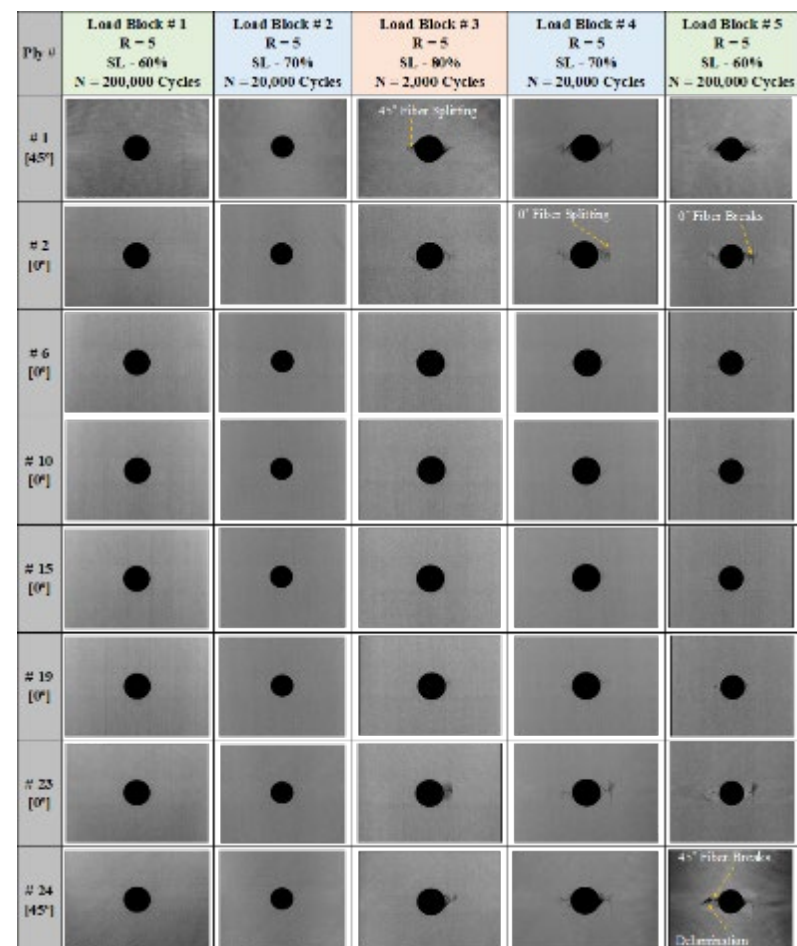


Figure 46. Stiffness degradation vs. number of cycles for UNI-QI OH with damage progression in critical plies (R = -1 spectrum)



(a) Constant $R = -1$ low-medium-high-medium-low



(b) Constant $R = 5$ low-medium-high-medium-low

Figure 47. Critical damage mechanisms at the end of each load block for 24-Ply UNI-QI OH (constant R-Ratio spectra)

3.3.3 Effect of stress levels: variable R-ratio spectra

After investigating the load-sequencing effects utilizing constant R-ratio spectra, this study was extended to include variable R-ratios. Two unique block spectra were generated, as detailed in Table 14 and schematically illustrated in Figure 48. Both stress levels and R-ratio were altered to study the damage mechanisms under the influence of varying stress ratios. As shown schematically in Figure 48(a), for the block spectrum comprising $R = 5$ and -1 , low, medium, and high load blocks were arranged in sequence with altering stress ratios. Similarly, the low, medium, and high LBs for respective R-ratios were reversely arranged in sequence to generate block spectra with $R = -1$ and 5 , as shown in Figure 48(b) and Table 14(b). In the fully reversed block ($R = -1$) contained in both spectra, the low, medium, and high stress levels were 50%, 60%, and 70% of the average static strength, respectively. For the compression fatigue block ($R = 5$), the low, medium, and high LBs were 60%, 70%, and 80% SL, respectively. In both spectra considered here to analyze the effect of mixed stress ratios, the stress levels were gradually increased within the spectrum.

Table 14. Fatigue profiles for sequencing study for 24-Ply UNI-QI OH with varying R-ratios³

Stress Level	Stress Ratio (R)	Max Stress (ksi)	Min Stress (ksi)	No. of Cycles
SL1 (Low-1 60%)	5	-6	-30	200,000
SL2 (Low-2 50%)	-1	25	-25	200,000
SL3 (Medium-1 70%)	5	-7	-35	20,000
SL4 (Medium-2 60%)	-1	30	-30	20,000
SL5 (High-1 80%)	5	-8	-40	1,000
SL6 (High-2 70%)	-1	35	-35	1,000

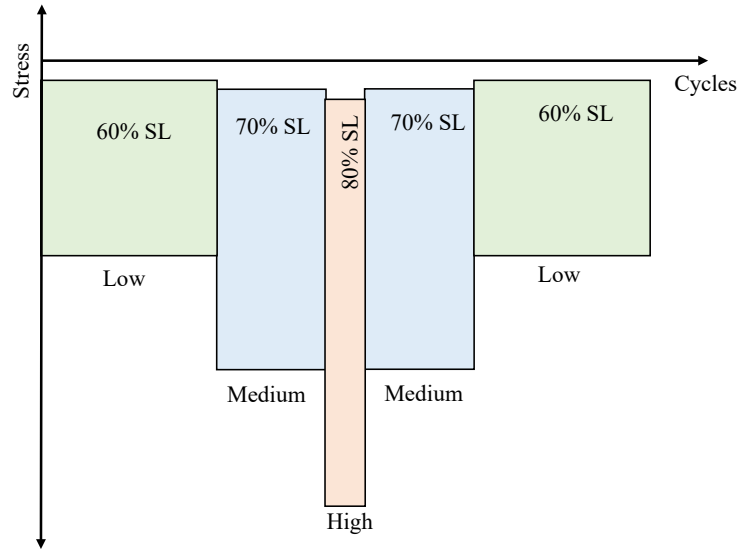
(a) $R = 5$ and -1

Stress Level	Stress Ratio (R)	Max Stress (ksi)	Min Stress (ksi)	No. of Cycles
SL1 (Low-2 50%)	-1	25	-25	200,000
SL2 (Low-1 60%)	5	-6	-30	200,000
SL3 (Medium-1 60%)	-1	30	-30	20,000
SL4 (Medium-2 70%)	5	-7	-35	20,000

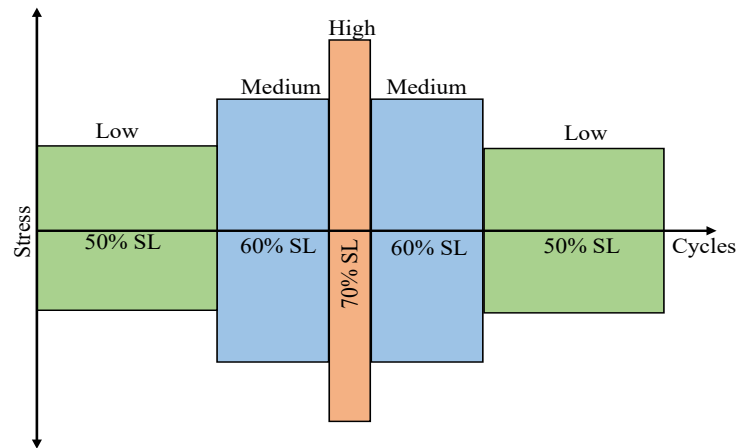
³ Note that *low*, *medium*, and *high* SL for both spectra have been differentiated with dark and light shades to highlight the varying stress levels.

SL5 (<i>High-2</i> 70%)	−1	35	−35	1,000
SL6 (<i>High-1</i> 80%)	5	−8	−40	1,000

(b) $R = -1$ and 5



(a) $R = 5$



(a) $R = -1$

Figure 48. Fatigue spectrum profiles for load-sequencing effects under varying R-ratios

Spectrum fatigue performed with mixed stress ratios resulted in failure mechanisms observed during compression and fully reversed fatigue testing, as discussed previously (see Table 5 for a brief summary). SD plots for both profiles are provided in Figure 49 and Figure 50. For the

profile with an initial compression fatigue LB, no damage was detected in this first LB ($R = 5$, 30 ksi), as shown in Figure 49. Damage was initiated in the second fully reversed LB ($R = -1$, 25 ksi). Fiber splitting along the outermost 0° and 45° plies along with delamination around the notched region was observed. Due to the severity in LB transition from compression to a fully reversed fatigue block, damage initiation was noted at the end of LB 2. Thus, despite being at a lower load level, the transition from compression to a fully reversed fatigue loading impacted the damage characteristics.

Conversely, having a fully reversed fatigue loading ($R = -1$, 25 ksi) in the beginning of the spectrum decreased the total damage accumulation, and the stiffness degradation vs. number of cycles for the spectrum containing an initial fully reversed loading ($R = 1$ and 5) is provided in Figure 50. As noted, fiber splits along the outermost 0° and 45° plies were initiated in LB 1. No significant damage growth, except for delamination around the notched region, was detected in LB 2 ($R = 5$, 60% SL). A comparison of critical damage initiations observed for both varying R-ratio fatigue profiles is shown in Figure 51.

Earlier in the study during evaluation of the sequencing effect (see section 3.2), it was found that damage accumulation was higher when the applied stress level transitioned from a low to high load block. From the investigation carried out here using mixed stress ratio spectrums, it can be concluded that a transition from compression to fully reversed fatigue block has a similar effect. Conversely, a compression LB (even with higher SL) behaves very similarly to a low LB in a fully reverse fatigue. A comprehensive fatigue study with altering sequence of stress and a constant average fatigue creep load, followed by fully reversed fatigue loading, are required to further investigate the sequencing effects of mixed R-ratio fatigue spectra.

For all the block spectra loading considered here, NDI scans were performed at the end of each load block for both UNI and PW. It was confirmed that the damage had progressed beyond half the specimen width prior to either the end of the final load block or specimen failure. For almost all the block spectra loading considered in this research (including Profiles #3, #5, #6, #5-A, and #6-A), the damage accumulation surpassed beyond the coupon half width in the initial stages of the block spectra, thus indicating the influence of size effects. To take into account the size effects as well as load sequencing, further studies must be performed to thoroughly characterize these two phenomena and decouple them.

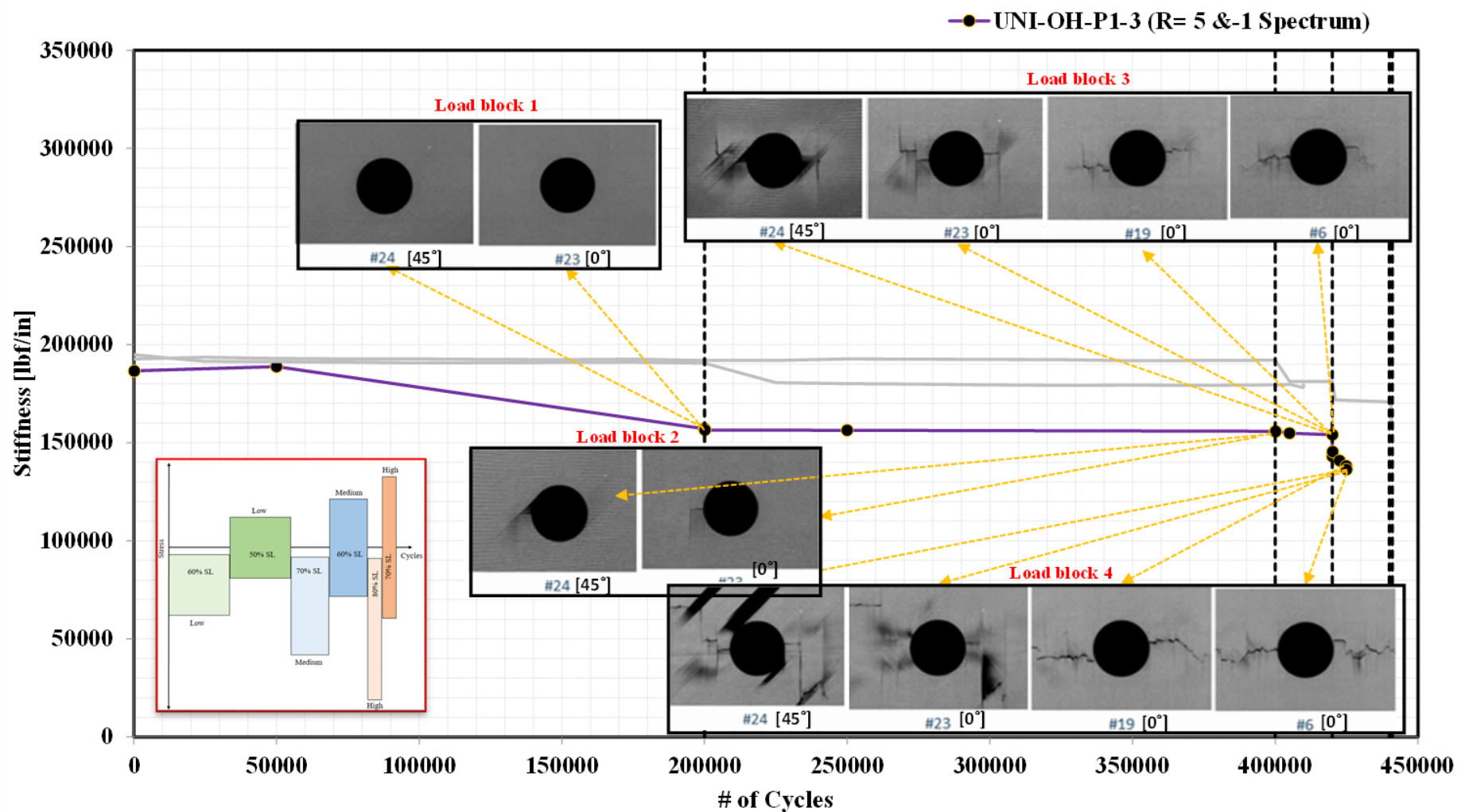


Figure 49. Stiffness degradation vs. number of cycles for UNI-QI OH with damage progression in critical plies (R = 5 and -1 spectra)

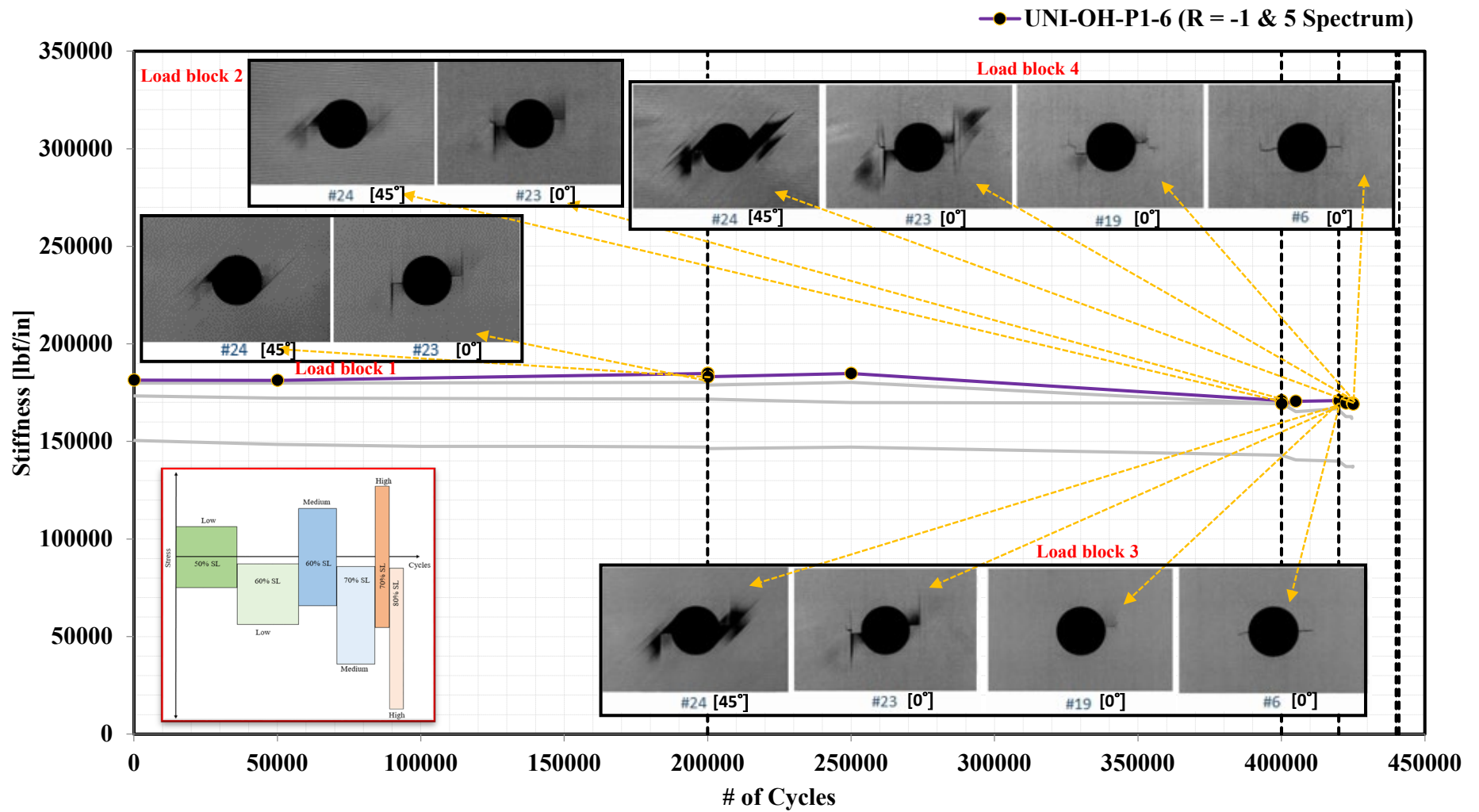


Figure 50. Stiffness degradation vs. number of cycles for UNI-QI OH with damage progression in critical plies (R = -1 and 5 spectra)

Ply #	Load Block # 1 R = 5 SL = 60% N = 200,000 Cycles	Load Block # 2 R = -1 SL = 50% N = 200,000 Cycles	Load Block # 3 R = 5 SL = 70% N = 20,000 Cycles	Load Block # 4 R = -1 SL = 60% N = 20,000 Cycles	Load Block # 5 R = 5 SL = 80% N = 1,000 Cycles	Load Block # 6 R = -1 SL = 70% N = 1,000 Cycles
# 1 [45°]						
# 2 [0°]						
# 6 [0°]						
# 10 [0°]						
# 15 [0°]						
# 19 [0°]						
# 23 [0°]						
# 24 [45°]						

(a) R= 5 and -1

Ply #	Load Block # 1 R = -1 SL = 50% N = 200,000 Cycles	Load Block # 2 R = 5 SL = 60% N = 200,000 Cycles	Load Block # 3 R = -1 SL = 60% N = 20,000 Cycles	Load Block # 4 R = 5 SL = 70% N = 20,000 Cycles	Load Block # 5 R = -1 SL = 70% N = 1,000 Cycles	Load Block # 6 R = 5 SL = 80% N = 1,000 Cycles
# 1 [45°]						
# 2 [0°]						
# 6 [0°]						
# 10 [0°]						
# 15 [0°]						
# 19 [0°]						
# 23 [0°]						
# 24 [45°]						

(b) R= -1 and 5.

Figure 51. Critical damage mechanisms at the end of each load block for 24-Ply UNI-QI OH (variable R-Ratio spectra)

3.3.4 Evaluation of service loads

Currently, composite structures are qualified by fatigue testing at low stress levels. It was found that pristine OH specimens were able to sustain high loads (70% SL) with minimal damage for a low number of cycles and were able to carry medium (55% SL) to low loads (40% SL) closer or beyond a million (cumulative) cycles without failure. Further studies conducted with compression-compression fatigue ($R = 5$) at a low (50%) stress level for a very high number of cycles (25 million) indicated minimal damage growth, as shown in Figure 52 (Seneviratne & Tomblin, 2016). In the scenario shown in Figure 52, the investigation was conducted on a quasi-isotropic layup subjected to a CA fatigue stress level that corresponds to approximately $3,200 \mu\epsilon$ (at undamaged state). Note that this stress level was 50% of the quasi-static strength. At lower loads, microcrack formation leads to stress redistribution around the notch, which increases the fatigue life of the coupon. This case of stress redistribution that happens at lower stress levels, along with the residual strength increase observed on tension-tension fatigued coupons at higher load levels, was discussed in detail in section 3.1.4. At these low strain levels, no sequencing effects are observed, since the applied stresses are insufficient to initiate damage. Typical aircraft designs employ strain levels that result in relatively small stress concentrations near holes and barely visible impact damage (BVID) locations.

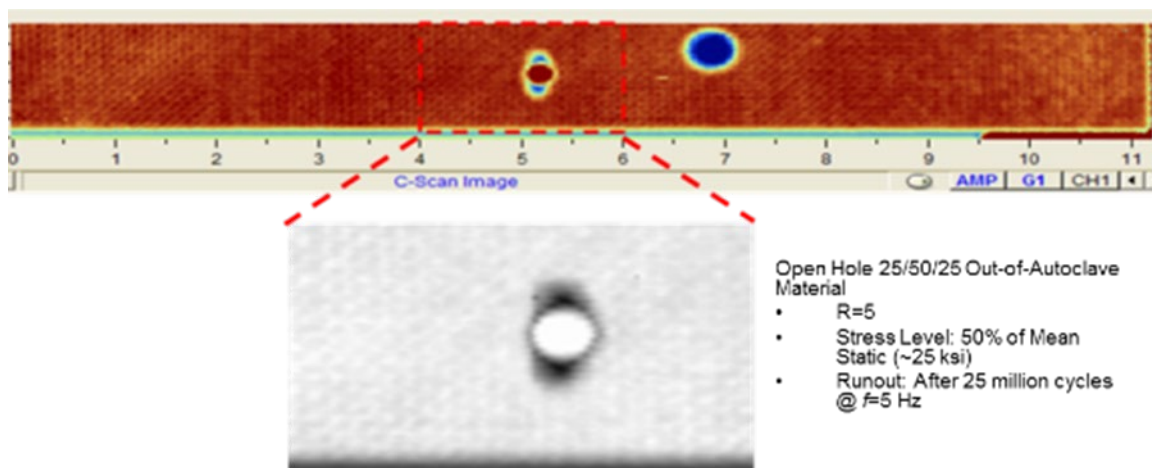


Figure 52. Damage growth in composites at realistic stress levels

4 Conclusions and outlook

In current aviation applications, overly conservative assumptions are employed during fatigue-life assessment, resulting in heavier aviation structures. This impedes utilizing the full weight savings potential of composites. The overly conservative assumptions are a result of complex fatigue damage mechanics of composite materials. During the course of this study, it was demonstrated that the fatigue life and damage of composite structures are governed by the sequence of occurrence of variable-amplitude loads (*load-sequencing effect*).

To illustrate the load-sequencing effect, three unique fatigue profiles with low, medium, and high load blocks were considered, wherein the high LB was at the beginning, middle, and end of the spectrum. Extensive damage characterization utilizing X-CT was performed; a comprehensive ply-level analysis was conducted to identify damage initiation and to characterize damage growth for various fatigue profiles. The observed failure characteristics were also compared against damage mechanisms obtained for CA fatigue tests in tension ($R = 0.1$), compression ($R = 5$), and fully reversed ($R = -1$) scenarios. Hence, this study also documented the primary failure mechanisms in CA tests, such as fiber splitting (matrix cracks), delamination, micro-buckling, and fiber breaks. A side study conducted on tensile-fatigued specimens showed a significant increase in both tensile (up to 21%) and compressive (7%) residual strengths.

The investigation carried out here on the sequencing effect clearly demonstrated that the sequence of occurrence of high load levels (70% SL) plays a significant role in governing the fatigue life and damage accumulation. A high LB in the beginning of the fatigue spectrum was found to sustain structures longer than having the high LB either in the middle or at the end. To further this research, supplementary studies were carried out by altering the laminate configuration and stress level in each LB, as well as utilizing spectra containing multiple stress ratios. Here, load-sequencing effects demonstrated on both UNI and PW laminate configurations were comparable.

In the study conducted to investigate the load-sequencing effect involving spectra with a mixed stress ratio, it was evident that damage accumulation corresponded well with those obtained in the previous study containing *high-low* LBs. Moreover, a transition in stress ratio from fully reversed to compression within the spectrum decreased the severity of damage accumulation. Conversely, when the stress ratio transitioned from compression to a fully reversed LB, a significant increase in damage accumulation rate was noted.

In summary, this research documents primary damage initiation mechanisms and subsequent progression under various fatigue-loading scenarios. High-fidelity NDI results were used to carry

out detailed ply-level analyses. In both laminate configurations—24-Ply T650/5320 UNI-QI OH and 16-Ply PW-QI OH—similar sequencing effects were confirmed. The set of experiments carried out here conclude that in a multi-stress level fatigue profile, a high LB in the beginning of the fatigue spectrum allows the structure to survive longer than having this high LB in the middle or at the end. Both stress levels and numbers of cycles in each LB of a spectrum were also found to be key contributors of load-sequencing effects.

In order to decouple the sequencing effects from finite width damage growth, longer and wider specimens will be tested as part of the future studies to validate whether the dominance of sequencing effects identified here exists. This study will be carried out using similar block spectra loading, materials system, and layup sequence. The studies published in the literature about sequencing effects provide mixed conclusions. In this work, sequencing effects and their influence on failure mechanisms were demonstrated using specially designed block spectrum loading configuration on a single material system (UNI and PW) employing only a single test method, namely OH. Therefore, this study must also be expanded to other material systems, layups, geometries, and change in occurrence of load sequence (or reduce realistic load spectra) to further solidify the observed load sequencing and size effects.

4.1 Pilot study on compression after impact coupons

In order to investigate load-sequencing effects, an OH specimen configuration was selected here to simulate a notched specimen scenario, because holes are the most common flaws found in aerospace applications. In addition to holes, impact damage and delamination are common flaws in aircraft structures. Damage mechanics associated with OH specimens will be different than those of an impacted coupon, because the latter experiences an impact event causing inherent delamination and fiber breaks in the laminate. Hence, efforts must be made to thoroughly document the initial damage state and further progression of various damage mechanisms that happen due to sequencing effects.

A pilot study was conducted here on compression after impact (CAI) coupons, and efforts were made to identify the damage mechanisms under the influence of two variable-amplitude fatigue loading scenarios. Profiles #5 and #6 (refer to Table 4) were considered by modifying stress levels in the low, medium, and high load blocks to be 50%, 65%, and 80%, respectively. The modified spectra are referred to as Profile #5-B and Profile #6-B in this section. TTU C-Scans were employed to observe damage growth and compare against the initial ($n = 0$) damage state. Two coupons were tested from each profile, and a 32-ply T650/5320 UNI-QI laminate configuration was chosen. A 6 x 4 in. coupon size was chosen and was impacted by 0.625 in.

tup-diameter with an energy level of 1,000 in-lb/in. C-Scan images at the end of each LB for both modified Profiles #5-B and #6-B are provided in Figure 53 and Figure 54, respectively. Note that the scanned images contain the C-Scan tracing dot and strain gages. Focus was placed around the notched region to monitor damage progression.

From the scanned images, it can be seen that CAI specimens subjected to an initial high load block (Profile #5-B) showed higher damage accumulation. Clear damage growth in the notched region at the end of the first *high* LB is clearly visible, as shown previously in Figure 53. This is in contrast to what was observed previously on OH specimens with an initial high LB in the spectrum. Note that only two coupons were considered for each spectrum here. Therefore, in order to comprehensively study the load-sequencing effect on CAI coupons, the study must be further extended to include more fatigue samples and profiles.

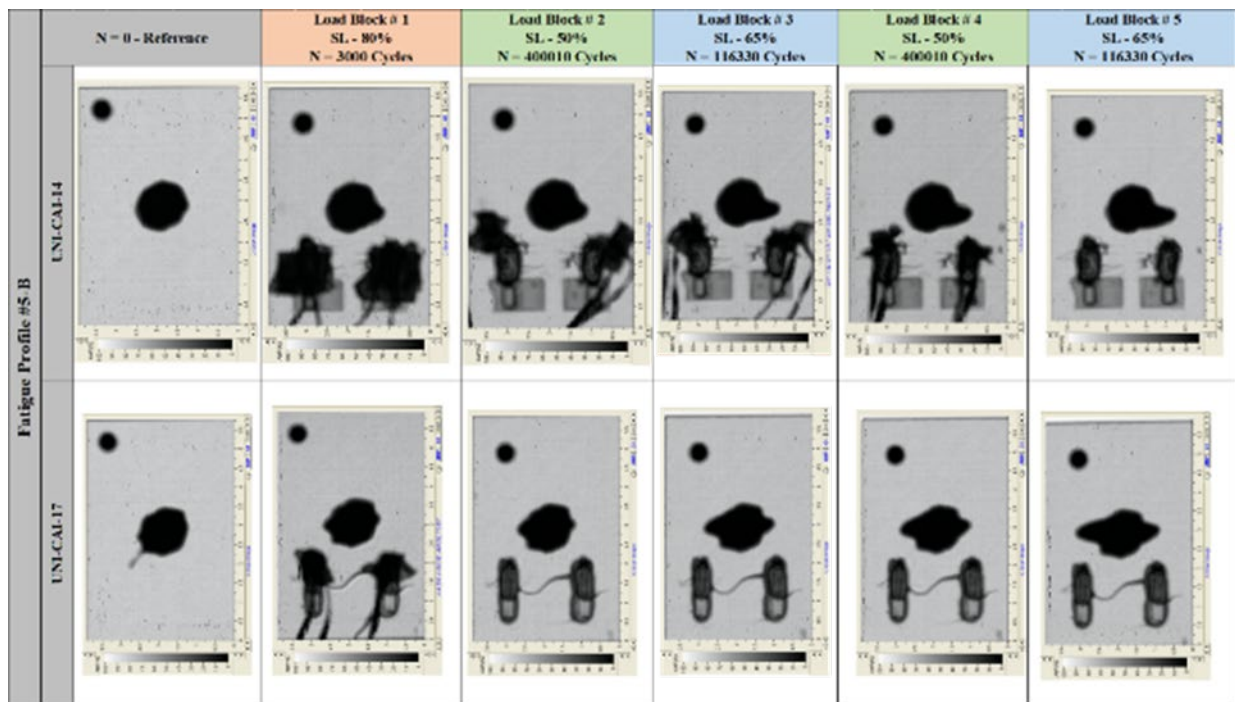


Figure 53. TTU C-Scan images for 16-Ply PW-QI CAI at the end of each load block for spectrum Profile #5-B

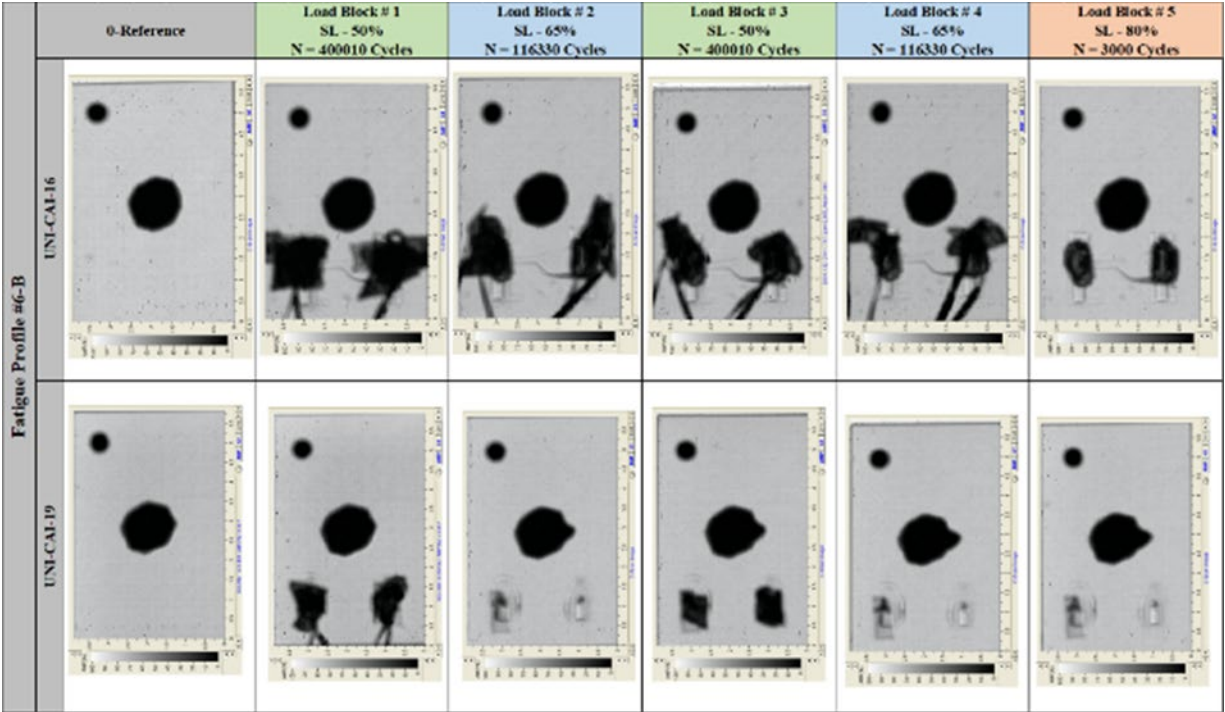


Figure 54. TTU C-Scan images for 16-Ply PW-QI CAI at the end of each load block for spectrum Profile #6-A

4.2 Recommendations

Recommendations for further research are noted as follows:

- Realistic flight data must be used to generate fatigue block spectra, and then load-sequencing effects for these profiles must be investigated.
- Similar tests must be performed using much larger specimens (width and length) while maintaining the same original defect sizes (holes and impact damage) to see if some parts of the load sequencing effects relate to finite specimen width effects and specific damage growth mechanisms.
- A tool must be developed to convert realistic flight data into several block spectra in order to aid in analyzing damage progression under variable-amplitude fatigue loads.
- Additional studies by including various material systems, layups, and geometries (OH, CAI, interlaminar tension, etc.) must be conducted.
- Additional critical fatigue profiles must be evaluated to study sequencing effects.

- Altered fatigue spectrums with variable stress ratio must be considered to evaluate sequencing effects.
- Prime failure mechanisms in PW and other material configurations using high-fidelity X-ray inspections during spectrum fatigue must be further investigated.

5 References

- Aly, N. M. (2017). A Review on Utilization of Textile Composites in Transportation Towards. *IOP Conference Series: Materials Science and Engineering*, (p. 042002). Vol. 254.
- ARAMIS v 6.3.0 User Manual. (2017). GOM GmbH.
- ASTM D5766 / D5766M-11. (1995). *Standard Test Method for Open Hole Tensile Strength of Polymer Matrix Composite Laminates*. West Conshohocken, PA: ASTM International. Retrieved from www.astm.org
- ASTM D6484 / D6484M-14. (2014). *Standard Test Method for Open-Hole Compressive Strength of Polymer Matrix Composite Laminates*. West Conshohocken, PA: ASTM International. Retrieved from www.astm.org
- ASTM D7615 / D7615M-19. (2019). *Standard Practice for Open-Hole Fatigue Response of Polymer Matrix Composite Laminates*. West Conshohocken, PA: ASTM International. Retrieved from www.astm.org
- Badaliane, R., & Dill, H. (1982). *Compression Fatigue Life Prediction Methodology for Composite Structures*. Vol. I and II, NADC Report.
- Bartley-Cho, J., Lim, S. G., Hahn, H. T., & Shyprykevich, P. (1998). Damage Accumulation in Quasi-Isotropic Graphite/Epoxy Laminates under Constant-Amplitude Fatigue and Block Loading. *Composites Science and Technology*, 58(9), 1535-1547.
- Berg, C., & Salama, M. (1973). Fatigue of Graphite Fibre-Reinforced Epoxy in Compression. *Fibre Science and Technology*, 6(2), 79-118.
- Broutman, L. J., & Sahu, S. (1972). A New Theory to Predict Cumulative Fatigue Damage in Fiberglass Reinforced Plastics. In H. T. Corten (Ed.), *Composite Materials: Testing and Design (Second Conference)* (pp. 170-188). West Conshohocken: ASTM International .
- Camponeschi, E. (1991). Compression of Composite Materials: A Review. *Composite Materials: Fatigue and Fracture (Third Volume)*, 1110, 550-578.
- Dang, C., Bernetich, K., Carter, E., & Butler, G. (2011). Mechanical Comparison of Out-of-Autoclave Prepreg Part to Conventional Autoclave Prepreg Part. *American Helicopter Society 67th Annual Forum* (pp. 3-5). Virginia Beach: American Helicopter Society.
- Evans, A., & Adler, W. (1978). Kinking as a Mode of Structural Degradation in Carbon Fiber Composites. *Acta Metallurgica*, 26(5), 725-738.

- Gamstedt, E. K., & Sjögren, B. (2002). An experimental Investigation of the Sequence Effect in Block Amplitude Loading of Cross-Ply Composite Laminates. *International Journal of Fatigue*, 24(2-4), 437-446.
- Halpin, J., Jerina, K., & Johnson, T. (1973). Characterization of Composites for the Purpose of Reliability Evaluation. *Analysis of Test Methods for High Modulus Fibers and Composites*, 521, 5-64.
- Han, K., & Hamdi, M. (1983). Fatigue Life Scattering of RP/C. *38th Annual RP/CI Conference*. SPI.
- Hart-Smith, L. (1995). An Engineer's Viewpoint on Design and Analysis of Aircraft Structural Joints. *Proceedings of the Institution of Mechanical Engineers, Part G: Journal of Aerospace Engineering*, 109(2), 105-129.
- Hart-Smith, L. J. (1989). A New Approach to Fibrous Composite Laminate Strength Prediction, Douglas Paper 8366. *MIL-HDBL-17 Committee Meeting*. Singer Island, Palm Beach, FL.
- Miner, M. A. (1945). Cumulative Damage in Fatigue. *Journal of Applied Mechanics*, 12(3), A159-A164.
- Naik, N., & Kumar, R. (1999). Compressive Strength of Unidirectional Composites: Evaluation and Comparison of Prediction Models. *Composite Structures*, 46(3), 299-308.
- North Star Imaging. (n.d.). X7000 Industrial 3D X-Ray Inspection System. North Star Imaging.
- O'Brien, T. (1985). Analysis of Local Delaminations and Their Influence on Composite Laminate Behavior. *Delamination and Debonding of Materials*, 876, 282-297.
- Palmgren, A. (1924). Durability of Ball Bearings. *ZVDI*, 68(14), 339-341.
- Sendeckyj, G. (1981). Fitting Models to Composite Materials Fatigue Data. (C. Chamis, Ed.) *Test Methods and Design Allowables for Fibrous Composites, II*, 245-260.
- Seneviratne, W. P., & Tomblin, J. S. (2012). *Certification of Composite-Metal Hybrid Structures using Load Enhancement Factors*. Baltimore, MD: AA Joint Advanced Materials and Structures (JAMS)/Aircraft Airworthiness and Sustainment (AA&S).
- Seneviratne, W. P., & Tomblin, J. S. (2016). *Load Sequencing Effects and Damage Growth Retardation of Composites*. Seattle, WA: Federal Aviation Administration, Joint Advanced Materials and Structures (JAMS).

- Seneviratne, W., & Tomblin, J. (2017). *Analytical Fatigue Life Determination Based on Residual Strength Degradation of Composites*. Salt Lake City, UT: Federal Aviation Administration, Joint Advanced Materials and Structures (JAMS).
- Seneviratne, W., & Tomblin, J. (2021). Life of Composites under Variable Amplitude Fatigue Using ST Method. *AIAA SciTech Forum*. Virtual: AIAA.
- Seneviratne, W., Tomblin, j., & Walimunige, R. (2020). *Advanced Material Characterization and Structural Certification (AMCSC) Volume 1 of 2*. Wright-Patterson Air Force Base: AFRL-RX-WP-TR-2020-0110.
- Solvay. (2017). <https://www.solvay.com/en/product/cycom-5320-1>. *Cycom 5320-1 Prepreg—Product Technical Data Sheet*. Retrieved from <https://www.solvay.com/en/>.
- Spearing, S., & Beaumont, P. (1992). Fatigue Damage Mechanics of Composite Materials. I: Experimental Measurement of Damage and Post-Fatigue Properties. *Composites Science and Technology*, 44(2), 159-168.
- Tomblin, J., & Seneviratne, W. (2011). *Determining the Fatigue Life of Composite Aircraft Structures Using Life and Load-Enhancement Factors*. Springfield, VA: Rep No DOT. FAA/AR-10/6. Dept of Transportation.
- Treasurer, P. (2006). Characterization and Analysis of Damage Progression in Non-traditional Composite Laminates with Circular Holes. (*Doctoral dissertation, Mechanical Engineering, Georgia Institute of Technology*).
- Wanhill, R. J. (2017). Fatigue Requirements for Aircraft Structures. In *Aerospace Materials and Material Technologies* (Vol. 1, pp. 331-352). Singapore: Springer.
- Whitehead, R. S., Kan, H., Cordero, R., & Saether, E. (1986). *Certification Testing Methodology for Composite Structures*. Volumes I and II, Report No. NADC-87042-60 (DOT/FAA/CT-86-39).
- Whitney, J., & Browning, C. (1972). Free-Edge Delamination of Tensile Coupons. *Journal of Composite Materials*, 6(2), 300-303.
- Wisnom, M. R. (1999). Size effects in the testing of fibre-composite materials. *Composites Science and Technology*, 1937-1957.
- Yan, Y., Wen, W., Chang, F., & Shyprykevich, P. (1999). Experimental Study on Clamping Effects on the Tensile Strength of Composite Plates with a Bolt-Filled Hole. *Composites Part A: Applied Science and Manufacturing*, 30(10), 1215-1229.

A High-fidelity X-CT summary of constant amplitude Fatigue testing

Figure A- 1. X-CT inspections of 24-Ply UNI-QI-OH-P2-CA specimen #21 ($R = 0.1$ at 25 K and 400 K cycles)	A-2
Figure A- 2. X-CT inspections of 24-Ply UNI-QI-OH-P2-CA specimen #21 ($R = 0.1$ at 600 K and 800 K cycles).....	A-3
Figure A- 3. X-CT inspections of 24-Ply UNI-QI-OH-P2-CA specimen #21 ($R = 0.1$ at 1,000 K and 1,100 K cycles).....	A-4
Figure A- 4. X-CT (cross-sectional views) of 24-Ply UNI-QI-OH-P2-CA specimen #21 ($R = 0.1$ at various fatigue cycles)	A-5
Figure A- 5. X-CT inspections of 24-Ply UNI-QI-OH-P2-CA specimen #8 ($R = 5$ at 100 K and 200 K cycles)	A-6
Figure A- 6. X-CT inspections of 24-Ply UNI-QI-OH-P2-CA specimen #8 ($R = 5$ at 400 K and 600 K cycles)	A-7
Figure A- 7. X-CT inspections of 24-Ply UNI-QI-OH-P2-CA specimen #8 ($R = 5$ at 800 K and 1,100 K cycles)	A-8
Figure A- 8. X-CT inspections of 24-Ply UNI-QI-OH-P2-CA specimen #17 ($R = -1$ at 10 K and 100 K cycles)	A-9
Figure A- 9. X-CT inspections of 24-Ply UNI-QI-OH-P2-CA specimen #17 ($R = -1$ at 200 K and 300 K cycles).....	A-10
Figure A- 10. X-CT inspections of 24-Ply UNI-QI-OH-P2-CA specimen #17 ($R = -1$ at 400 K and 500 K cycles).....	A-11
Figure A- 11. X-CT inspections of 24-Ply UNI-QI-OH-P2-CA specimen #17 ($R = -1$ at 600 K and 650 K cycles).....	A-12
Figure A- 12. X-CT inspections of 24-Ply UNI-QI-OH-P2-CA specimen #17 ($R = -1$ at 700 K and 730 K cycles).....	A-13

High-fidelity X-CT ply-level inspections conducted on CA fatigue coupons under tension ($R = 0.1$), compression ($R = 5$), and fully reversed ($R = -1$) loading scenarios are presented here. This ply-level data was used to investigate damage mechanisms and damage progression in each ply for all CA fatigue scenarios. Four-dimensional (4D) X-CT video with all inspections can be furnished upon request. Note that damage accumulation in the high-fidelity X-CT three-dimensional (3D) model along with the number of cycles (time) is identified as 4D.

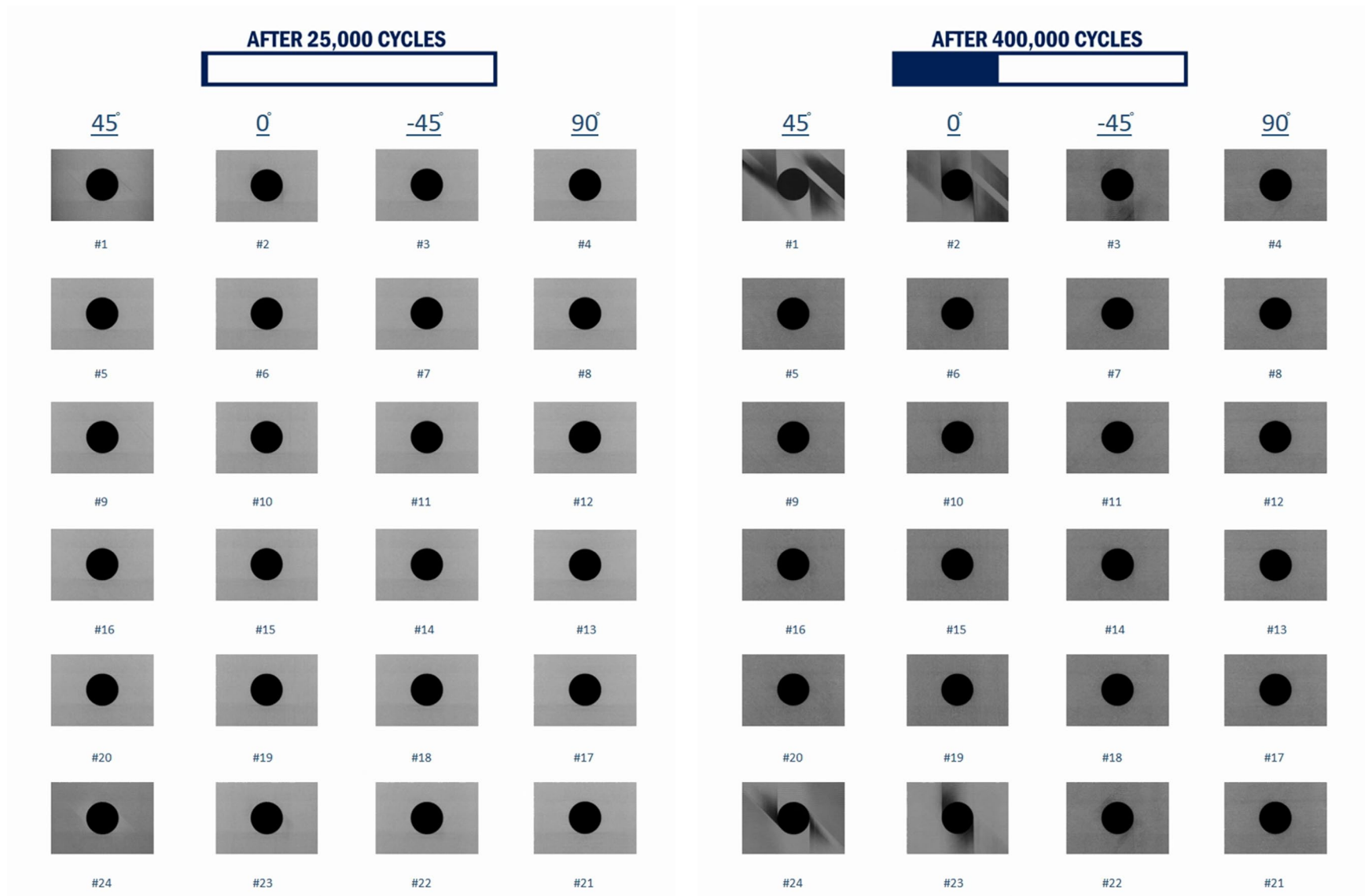


Figure A- 1. X-CT inspections of 24-Ply UNI-QI-OH-P2-CA specimen #21 ($R = 0.1$ at 25 K and 400 K cycles)

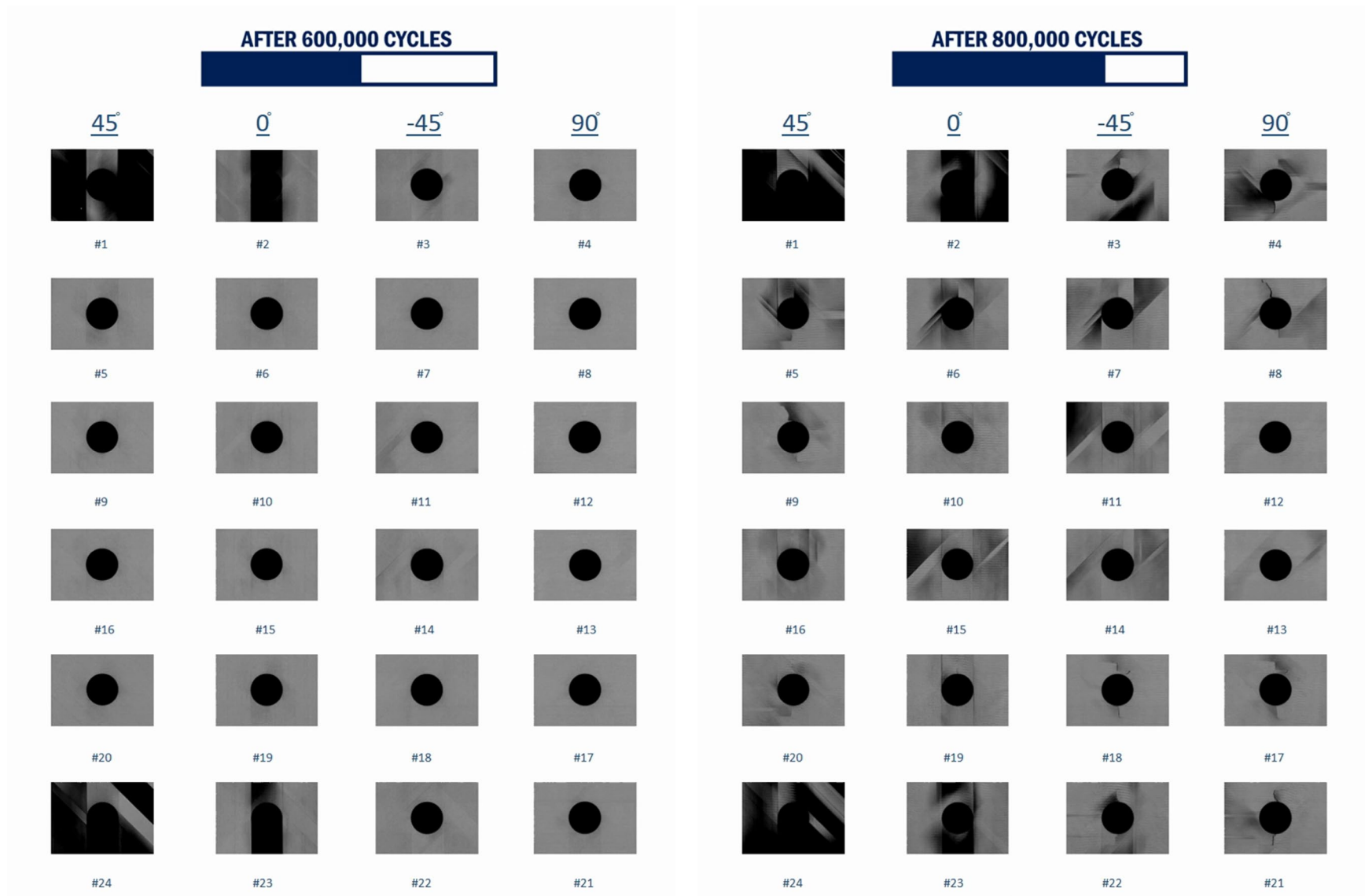


Figure A- 2. X-CT inspections of 24-Ply UNI-QI-OH-P2-CA specimen #21 ($R = 0.1$ at 600 K and 800 K cycles)

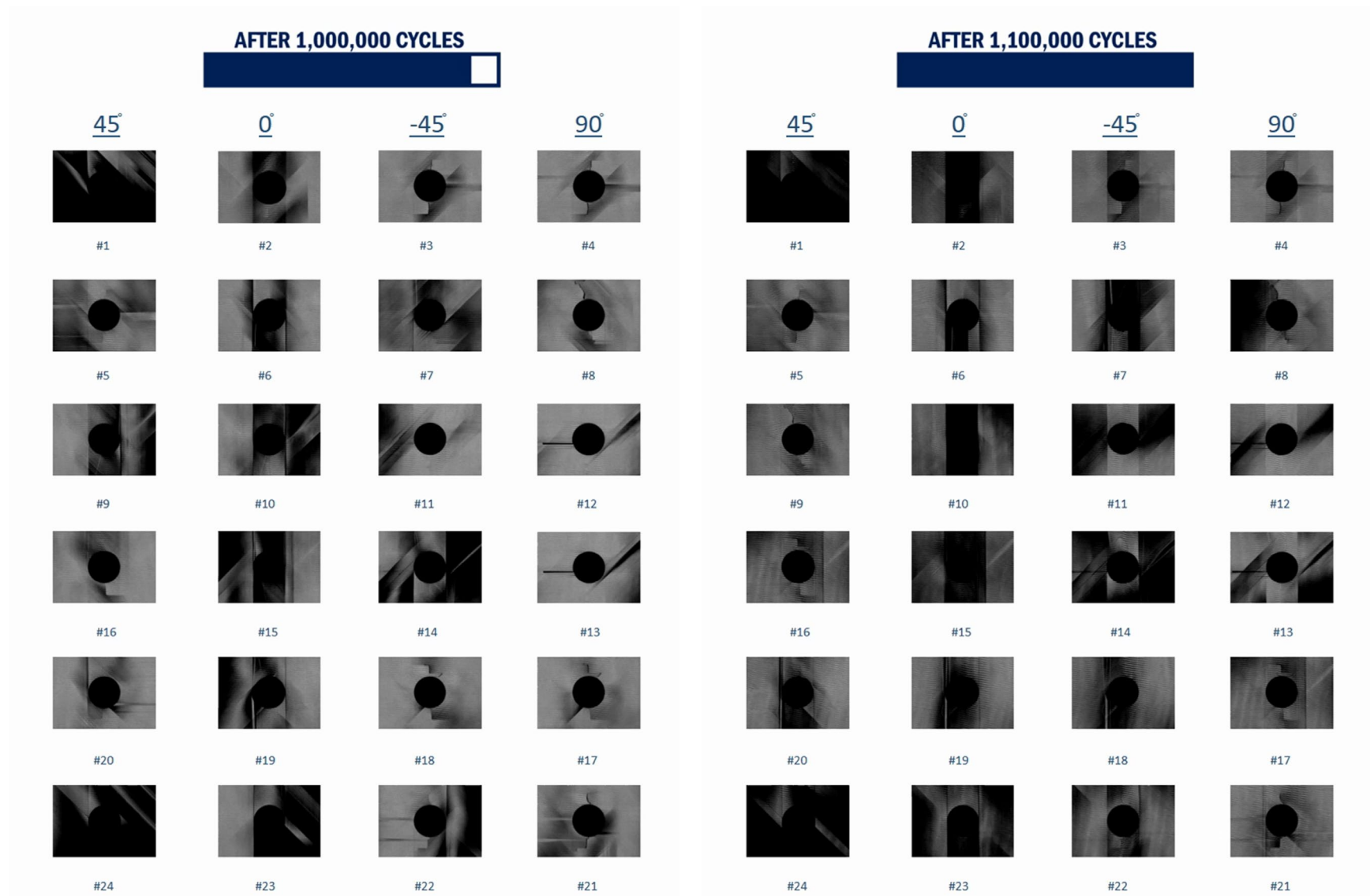


Figure A- 3. X-CT inspections of 24-Ply UNI-QI-OH-P2-CA specimen #21 ($R = 0.1$ at 1,000 K and 1,100 K cycles)

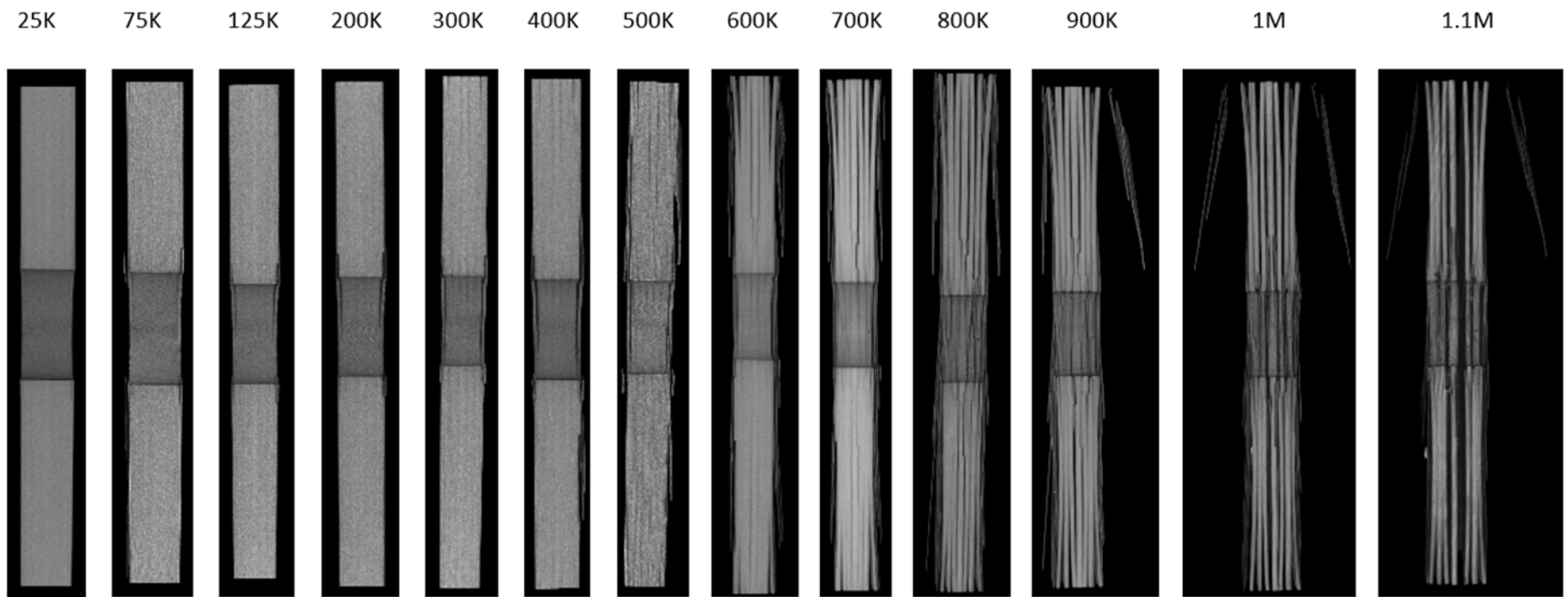


Figure A- 4. X-CT (cross-sectional views) of 24-Ply UNI-QI-OH-P2-CA specimen #21 ($R = 0.1$ at various fatigue cycles)

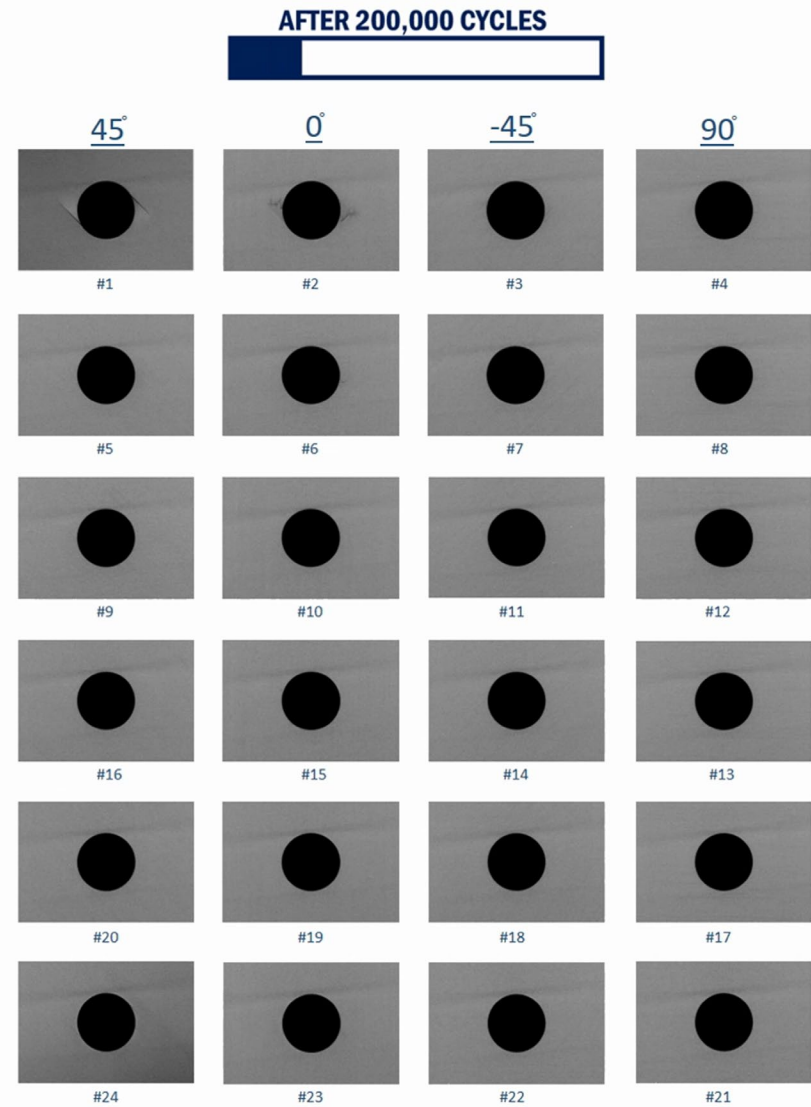
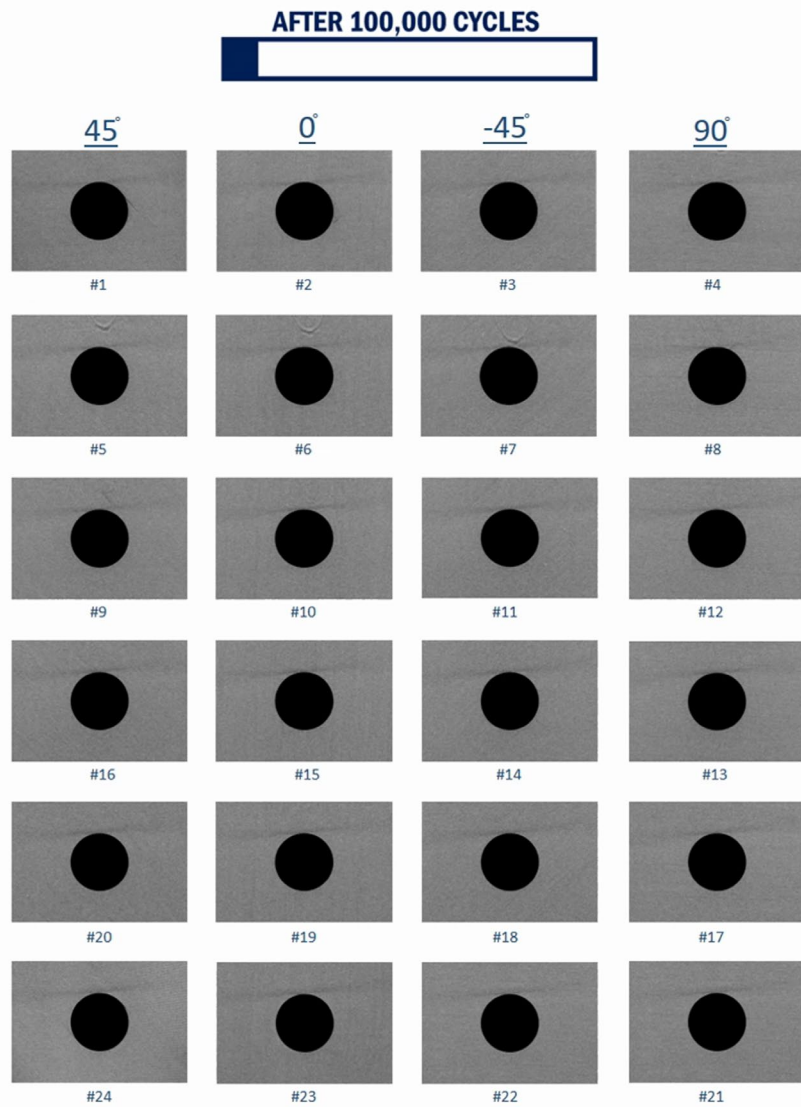


Figure A- 5. X-CT inspections of 24-Ply UNI-QI-OH-P2-CA specimen #8 (R = 5 at 100 K and 200 K cycles)

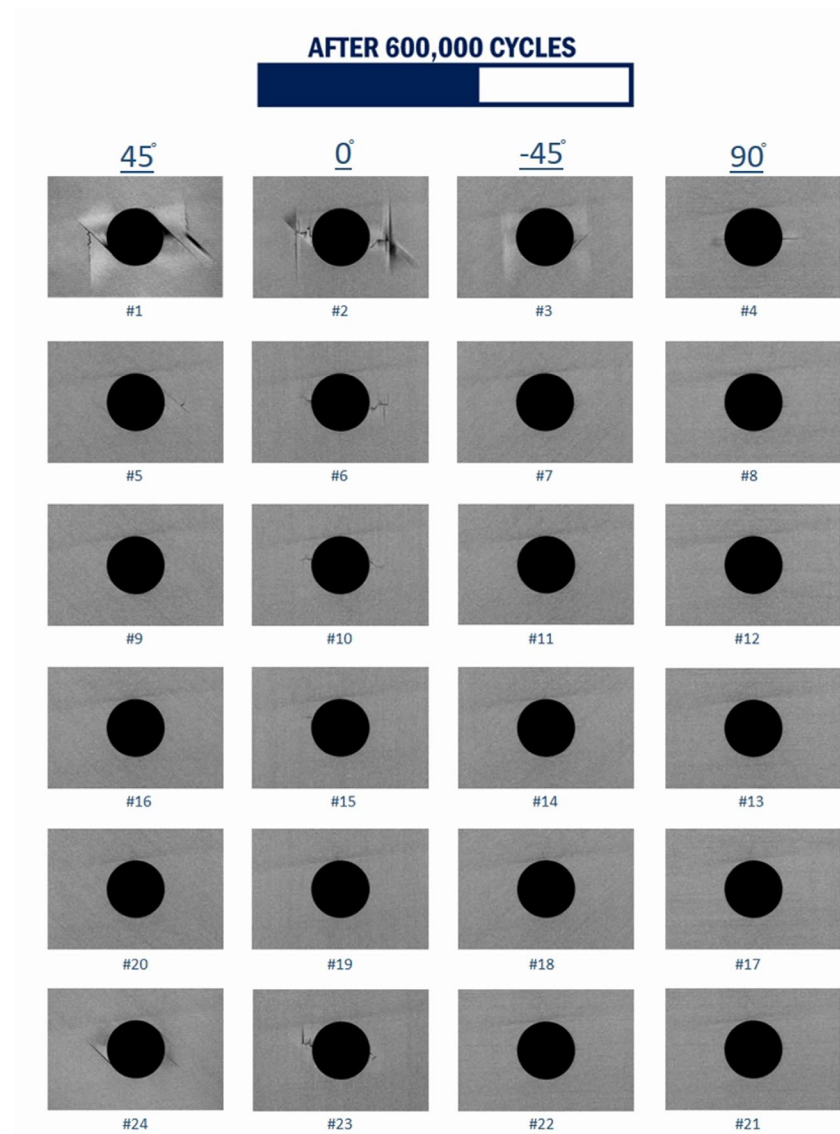
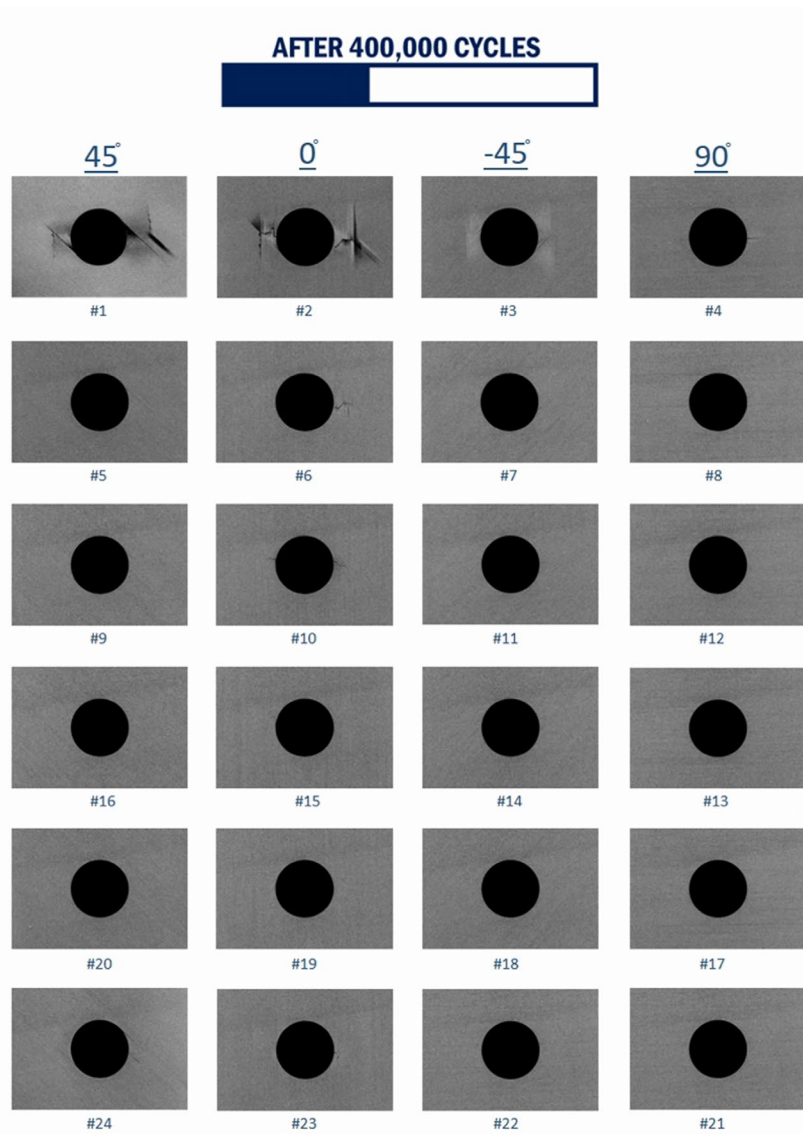


Figure A- 6. X-CT inspections of 24-Ply UNI-QI-OH-P2-CA specimen #8 (R = 5 at 400 K and 600 K cycles)

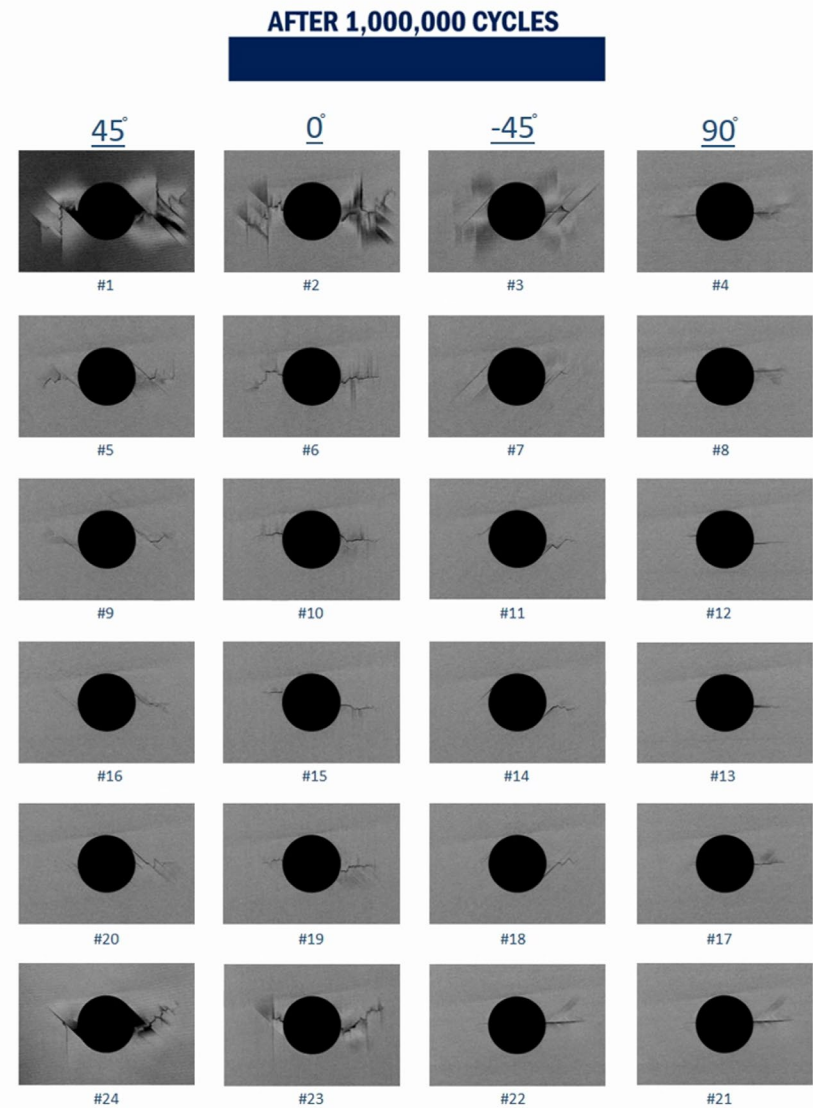
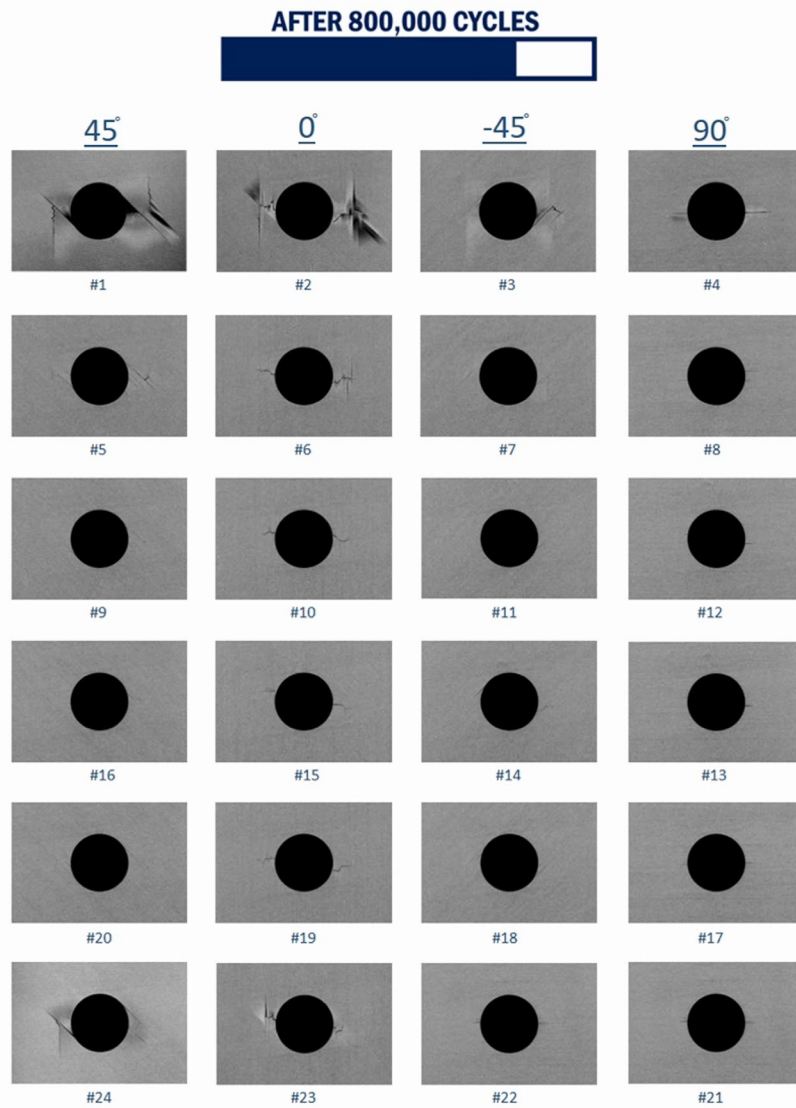


Figure A- 7. X-CT inspections of 24-Ply UNI-QI-OH-P2-CA specimen #8 (R = 5 at 800 K and 1,100 K cycles)

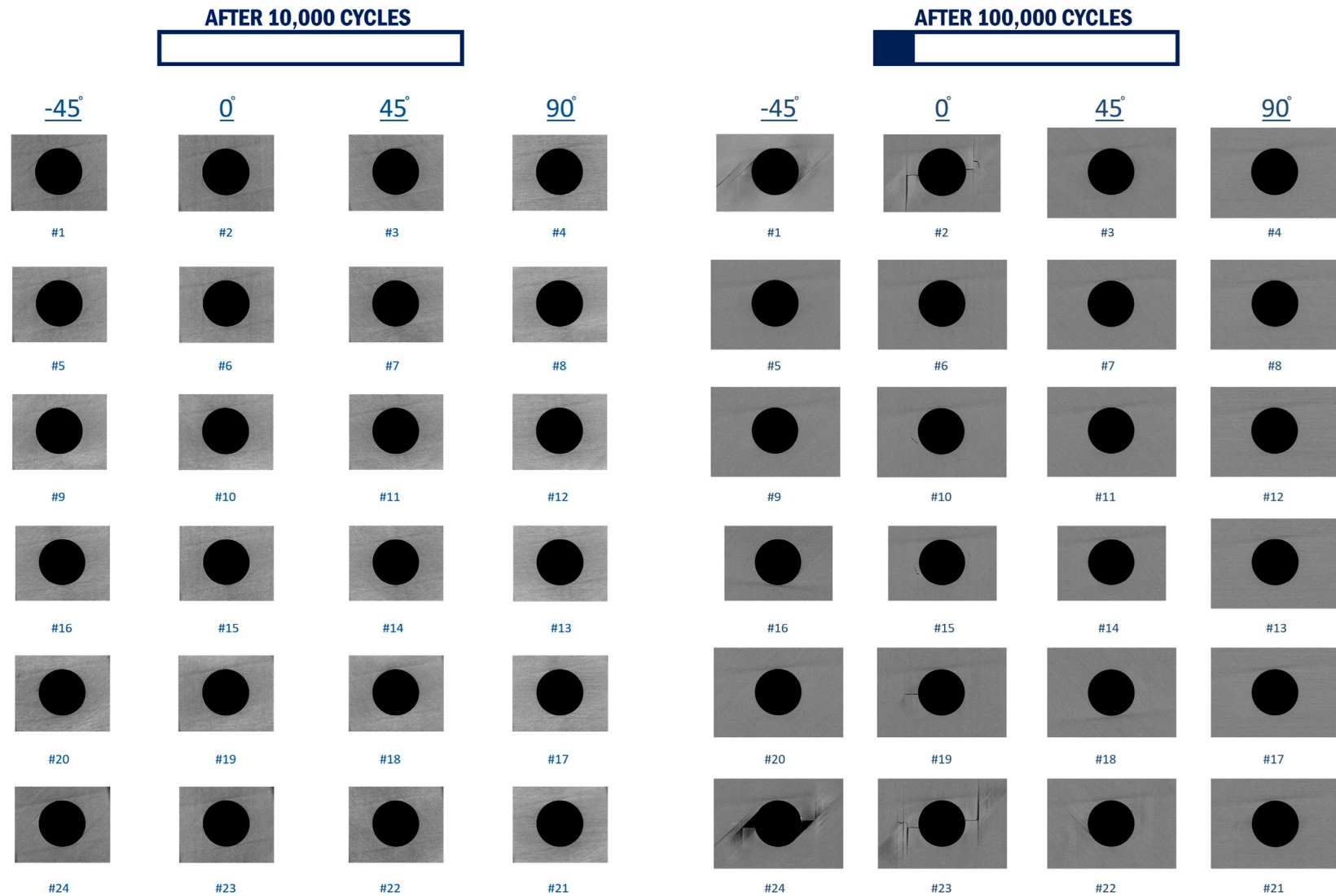


Figure A- 8. X-CT inspections of 24-Ply UNI-QI-OH-P2-CA specimen #17 ($R = -1$ at 10 K and 100 K cycles)

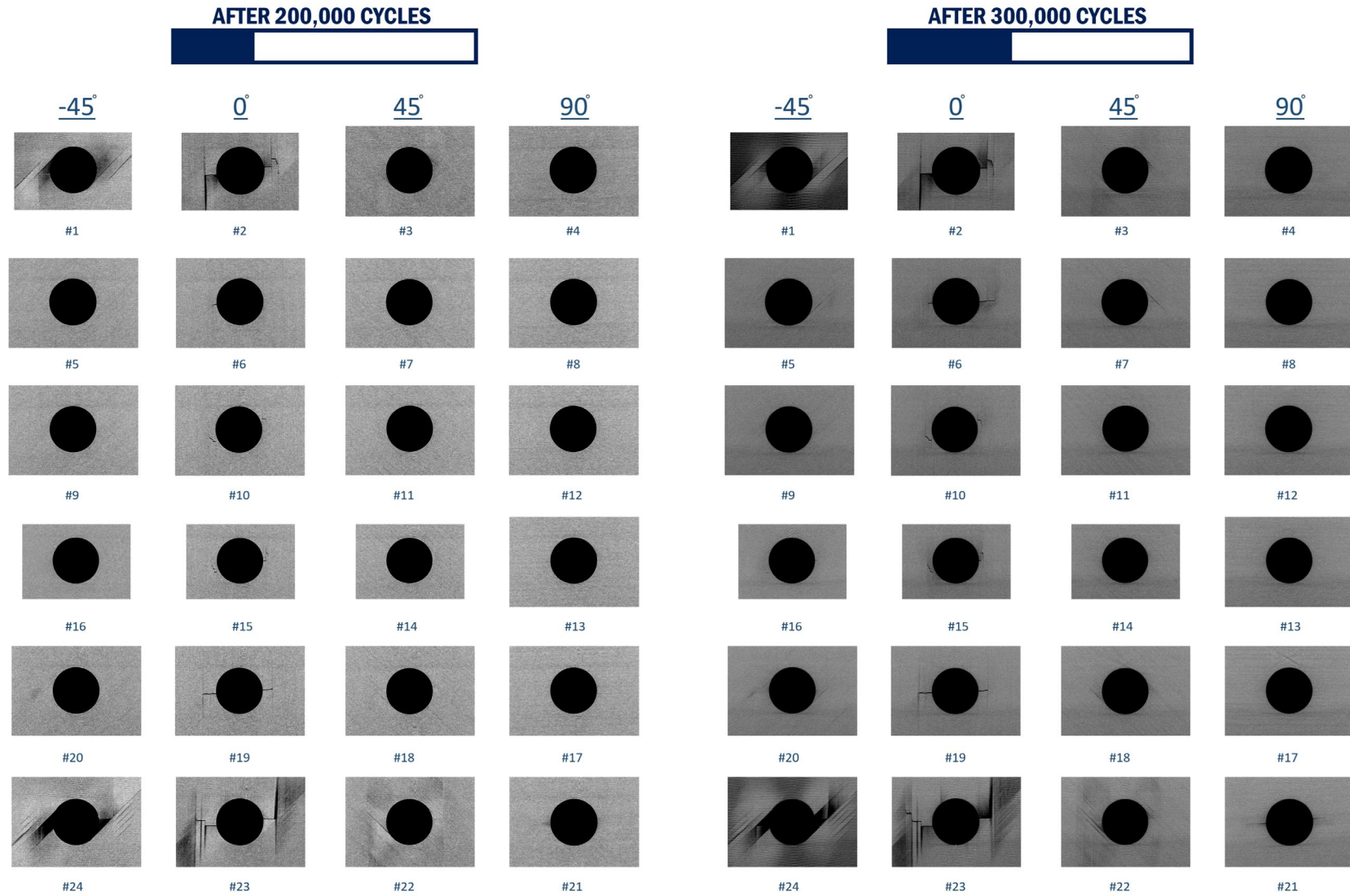


Figure A- 9. X-CT inspections of 24-Ply UNI-QI-OH-P2-CA specimen #17 ($R = -1$ at 200 K and 300 K cycles)

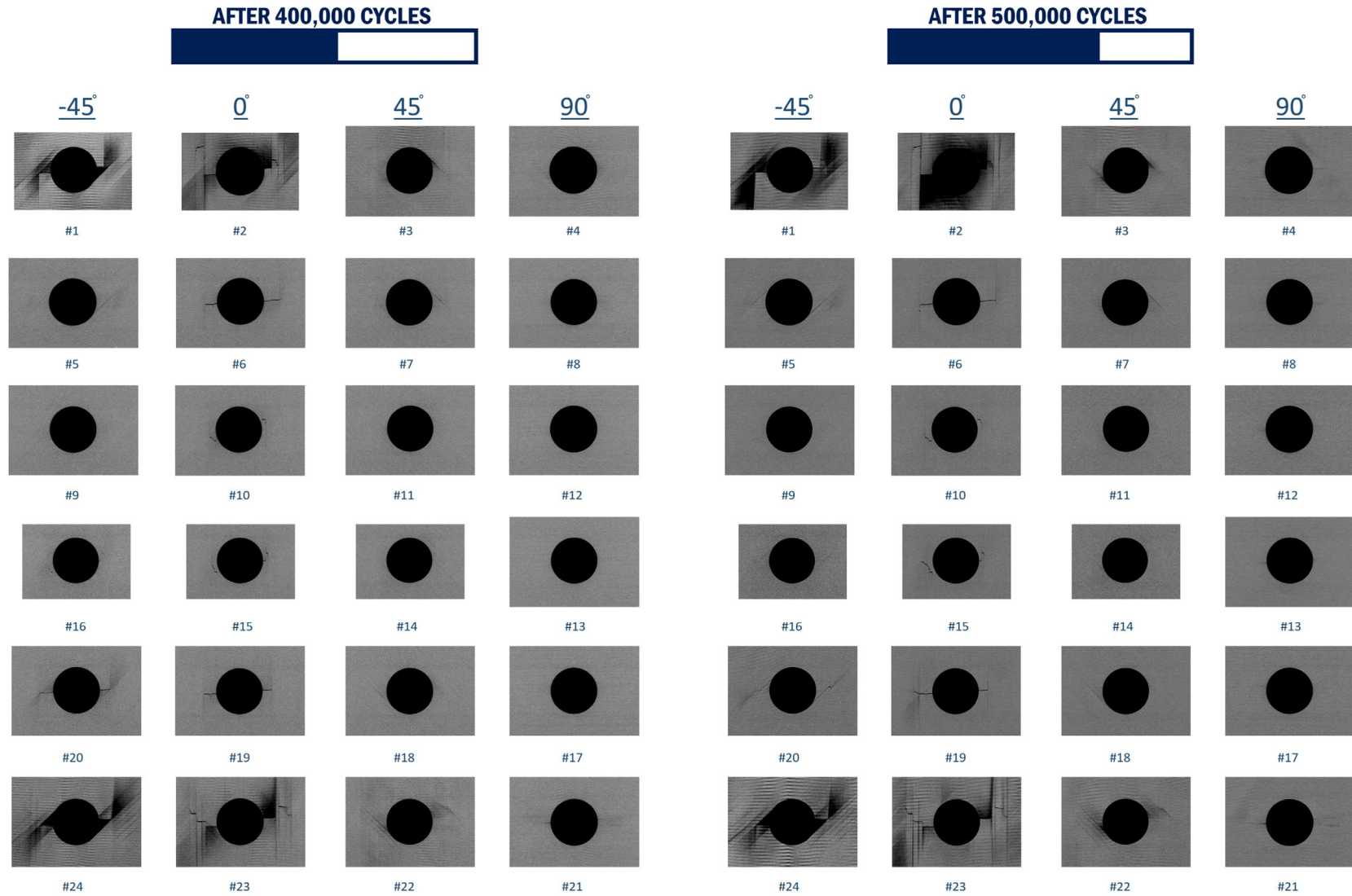


Figure A- 10. X-CT inspections of 24-Ply UNI-QI-OH-P2-CA specimen #17 ($R = -1$ at 400 K and 500 K cycles)

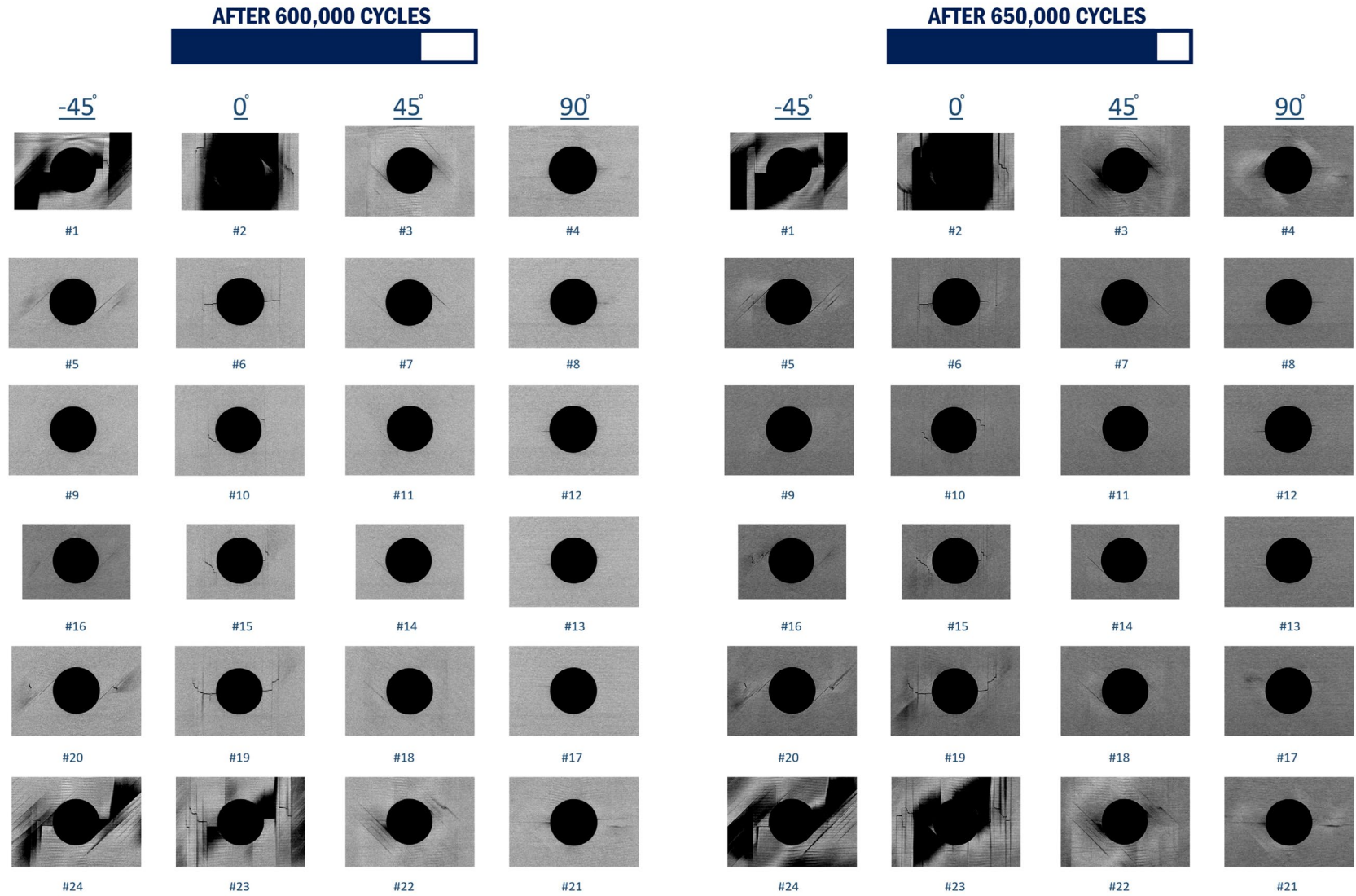


Figure A- 11. X-CT inspections of 24-Ply UNI-QI-OH-P2-CA specimen #17 ($R = -1$ at 600 K and 650 K cycles)

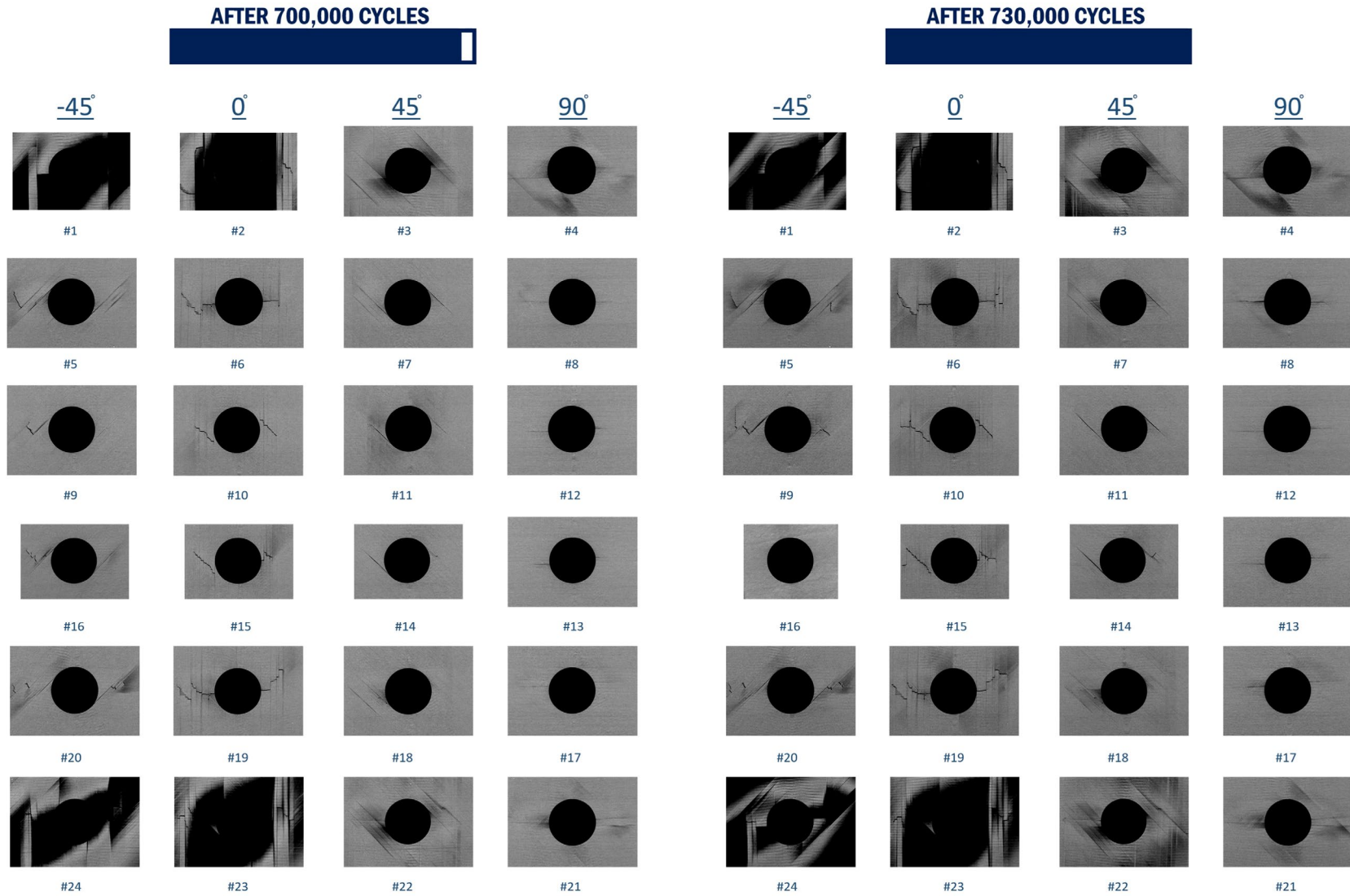


Figure A- 12. X-CT inspections of 24-Ply UNI-QI-OH-P2-CA specimen #17 ($R = -1$ at 700 K and 730 K cycles)

B Fatigue and high-fidelity X-CT summary of spectrum fatigue profiles

Figure B- 1. X-CT inspections of 24-Ply UNI-QI-OH Profile #5 (Specimen #25 at 3 K and 403 K Cycles) (LB 1 and 2).....	B-4
Figure B- 2. X-CT inspections of 24-Ply UNI-QI-OH Profile #5 (Specimen #25 at 519,340 and 919,350 Cycles) (LB 3 and 5).....	B-5
Figure B- 3. X-CT inspections of 24-Ply UNI-QI-OH Profile #5 (Specimen #25 at 989,148 and 1,012,414 Cycles) (LB 5).....	B-6
Figure B- 4. X-CT inspections of 24-Ply UNI-QI-OH Profile #6 (Specimen #26 at 400 K and 516,340 Cycles) (LB 1 and 2).....	B-7
Figure B- 5. X-CT inspections of 24-Ply UNI-QI-OH Profile #6 (Specimen #26 at 916,350 and 1,032,680 Cycles) (LB 3 and 4).....	B-8
Figure B- 6. X-CT inspections of 24-Ply UNI-QI-OH Profile #6 (Specimen #26 at 1,033,880 and 1,035,680 Cycles) (LB 5).....	B-9
Figure B- 7. X-CT inspections of 24-Ply UNI-QI-OH Profile #3 (Specimen #24 at 400 K and 516,340 Cycles) (LB 1 and 2).....	B-10
Figure B- 8. X-CT inspections of 24-Ply UNI-QI-OH Profile #3 (Specimen #24 at 517,540 and 519,340 Cycles) (LB 3).....	B-11
Figure B- 9. X-CT inspections of 24-Ply UNI-QI-OH Profile #3 (Specimen #24 at 635,670 and 1,035,680 Cycles) (LB 4 and 5).....	B-12

High-fidelity X-CT ply-level inspections conducted on fatigue coupons under spectrum fatigue Profiles, #3, #5, and #6 are presented here. The ply-level data was used to investigate damage mechanisms and damage progression in each ply for all CA fatigue scenarios. Four-dimensional (4D) X-CT video with all inspections can be furnished upon request. Note that damage accumulation in the high-fidelity X-CT three-dimensional (3D) model along with the number of cycles (time) is identified as 4D. In addition, a fatigue summary of UNI-QI and PW-QI laminate configurations for Profiles #3, #5, and #6 are also presented here.

B.1. Fatigue summary tables

Table B 1. Fatigue summary of sequencing study for 24-Ply UNI-QI-OH

NAME	Profile	R-Ratio	Load Block 1			Load Block 2			Load Block 3			Load Block 4			Load Block 5			Total # of Cycles Survived
			Max Stress [ksi]	Min Stress [ksi]	Cycles Survived	Max Stress [ksi]	Min Stress [ksi]	Cycles Survived	Max Stress [ksi]	Min Stress [ksi]	Cycles Survived	Max Stress [ksi]	Min Stress [ksi]	Cycles Survived	Max Stress [ksi]	Min Stress [ksi]	Cycles Survived	
UNI-EX-5	3	-1	20	-20	400010	27	-27	116330	35	-35	716	27	-27		20	-20		517056
UNI-EX-7	3	-1	20	-20	400010	27	-27	116330	35	-35	3058	27	-27		20	-20		519398
UNI-EX-8	3	-1	20	-20	400010	27	-27	116330	35	-35	3000	27	-27	116330	20	-20	400010	1035785
UNI-EX-9	3	-1	20	-20	400010	27	-27	116330	35	-35	3000	27	-27	103366	20	-20		622706
UNI-EX-10	3	-1	20	-20	400010	27	-27	116330	35	-35	2737	27	-27		20	-20		519077
FY15-UNI-OH-11	3	-1	20	-20	400010	27	-27	116330	35	-35	3000	27	-27	116330	20	-20	400010	1035680
FY15-UNI-OH-24	3	-1	20	-20	400010	27	-27	116330	35	-35	3000	27	-27	116330	20	-20	400010	1035680
UNI-EX-11	5	-1	35	-35	3000	20	-20	400010	27	-27	116330	20	-20	400010	27	-27	116330	1035680
UNI-EX-13	5	-1	35	-35	3000	20	-20	400010	27	-27	116330	20	-20	400010	27	-27	116330	1035680
UNI-EX-14	5	-1	35	-35	3000	20	-20	400010	27	-27	116330	20	-20	400010	27	-27	116330	1035680
UNI-EX-17	5	-1	35	-35	3000	20	-20	400010	27	-27	116330	20	-20	400010	27	-27	116330	1035680
UNI-EX-19	5	-1	35	-35	3000	20	-20	400010	27	-27	116330	20	-20	400010	27	-27	116330	1035680
UNI-EX-21	5	-1	35	-35	3000	20	-20	400010	27	-27	116330	20	-20	400010	27	-27	116330	1035680
FY15-UNI-OH-25	5	-1	35	-35	3000	20	-20	400010	27	-27	116330	20	-20	400010	27	-27	116330	1035680
FY15-UNI-OH-3	5	-1	35	-35	3000	20	-20		27	-27		20	-20		27	-27		3000
FY15-UNI-OH-4	5	-1	35	-35	3000	20	-20	400010	27	-27	116330	20	-20		27	-27		519340
FY15-UNI-OH-9	5	-1	35	-35	3000	20	-20	400010	27	-27	116330	20	-20	400010	27	-27	116330	1035680
UNI-EX-12	6	-1	20	-20	400010	27	-27	116330	20	-20	400010	27	-27	116330	35	-35	2775	1035455
UNI-EX-15	6	-1	20	-20	400010	27	-27	116330	20	-20	400010	27	-27	116330	35	-35	3000	1035680
UNI-EX-16	6	-1	20	-20	400010	27	-27	116330	20	-20	400010	27	-27	116330	35	-35	472	1033152
UNI-EX-18	6	-1	20	-20	400010	27	-27	116330	20	-20	400010	27	-27	116330	35	-35	543	1033223
UNI-EX-20	6	-1	20	-20	400010	27	-27	116330	20	-20	400010	27	-27	116330	35	-35	2447	1035127
UNI-EX-22	6	-1	20	-20	400010	27	-27	116330	20	-20	400010	27	-27	116330	35	-35	3000	1035680
FY15-UNI-OH-26	6	-1	20	-20	400010	27	-27	116330	20	-20	400010	27	-27	116330	35	-35	3000	1035680
FY15-UNI-OH-6	6	-1	20	-20	400010	27	-27	116330	20	-20		27	-27		35	-35		516340
FY15-UNI-OH-7	6	-1	20	-20	400010	27	-27	116330	20	-20	400010	27	-27	116330	35	-35		1032680
FY15-UNI-OH-8	6	-1	20	-20	400010	27	-27	116330	20	-20	400010	27	-27	116330	35	-35	3000	1035680

Table B 2. Fatigue summary of sequencing study for 16-Ply PW-QI-OH

NAME	Profile	R-Ratio	Load Block 1			Load Block 2			Load Block 3			Load Block 4			Load Block 5			Total # of Cycles Survived	Comments
			Max Stress [ksi]	Min Stress [ksi]	Cycles Survived	Max Stress [ksi]	Min Stress [ksi]	Cycles Survived	Max Stress [ksi]	Min Stress [ksi]	Cycles Survived	Max Stress [ksi]	Min Stress [ksi]	Cycles Survived	Max Stress [ksi]	Min Stress [ksi]	Cycles Survived		
FY15-PW-OH-27	5	-1	32	-32	1040	19	-19	400010	25	-35	14560	19	-19	400010	25	-25	14560	830180	Survived
FY15-PW-OH-1	5	-1	32	-32	1040	19	-19	400010	25	-35	14560	19	-19	400010	25	-25	7905	823525	Failed
FY15-PW-OH-2	5	-1	32	-32	1040	19	-19	400010	25	-35	14560	19	-19	400010	25	-25	12212	827832	Failed
FY15-PW-OH-3	6	-1	19	-19	400010	25	-25	14560	19	-35	400010	25	-25	970	32	-32		815550	Failed
FY15-PW-OH-5	6	-1	19	-19	400010	25	-25	14560	19	-34	400010	25	-25	8269	32	-32		822849	Failed
FY15-PW-OH-6	6	-1	19	-19	400010	25	-25	14560	19	-33	400010	25	-25	1422	32	-32		816002	Failed

B.2. Ply-level damage progression

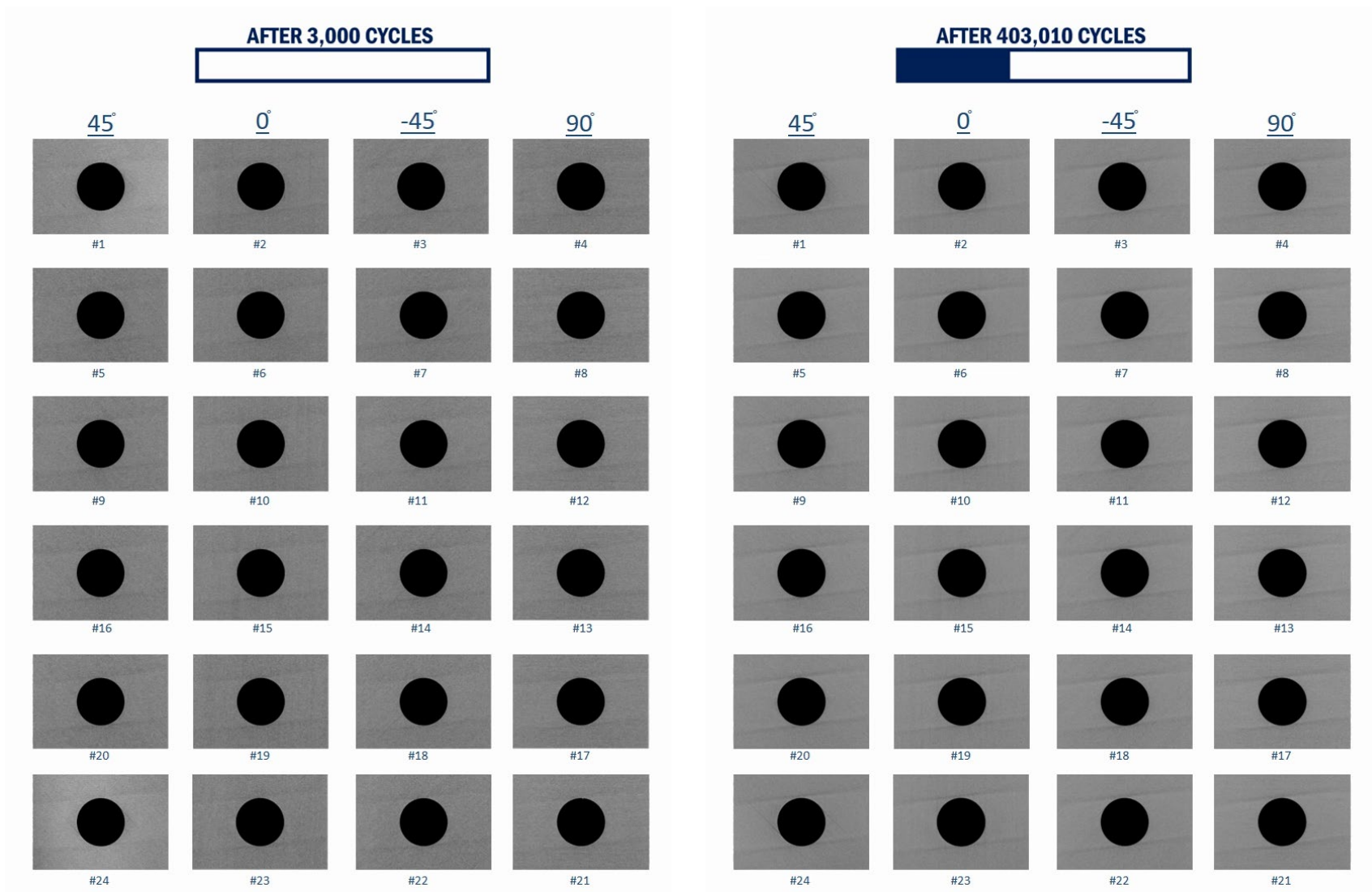


Figure B- 1. X-CT inspections of 24-Ply UNI-QI-OH Profile #5 (Specimen #25 at 3 K and 403 K Cycles) (LB 1 and 2)

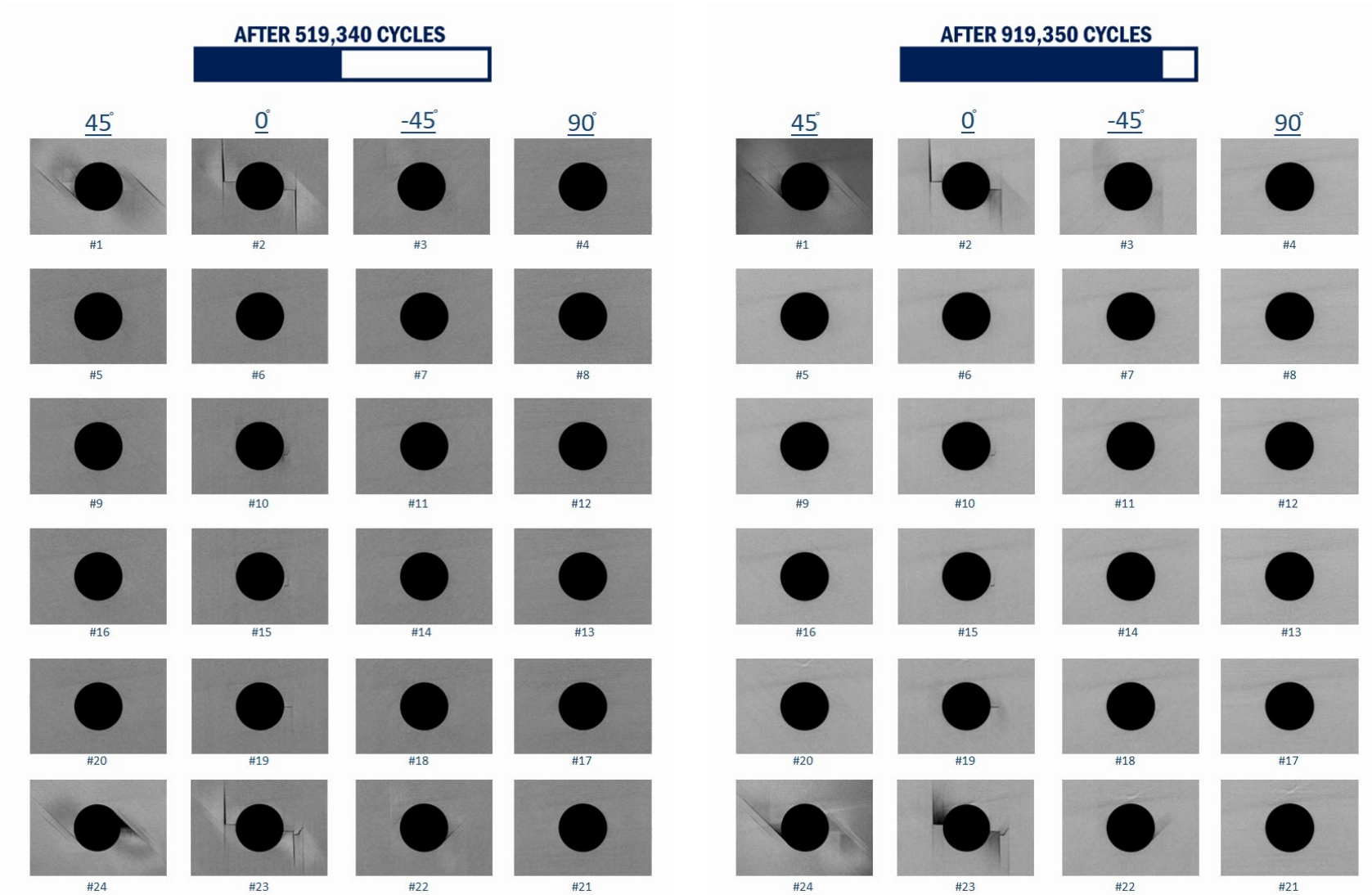


Figure B- 2. X-CT inspections of 24-Ply UNI-QI-OH Profile #5 (Specimen #25 at 519,340 and 919,350 Cycles) (LB 3 and 5)

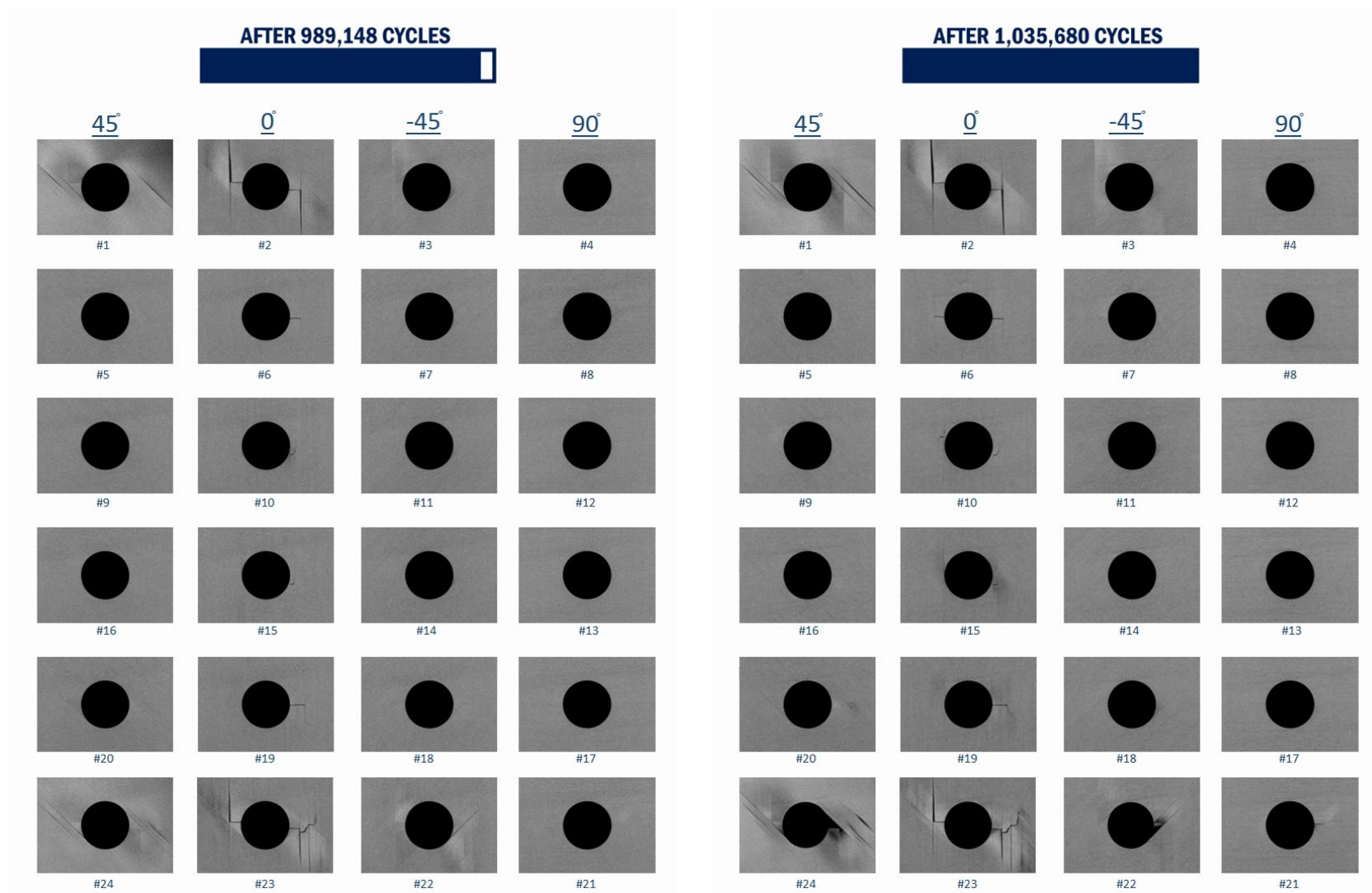


Figure B- 3. X-CT inspections of 24-Ply UNI-QI-OH Profile #5 (Specimen #25 at 989,148 and 1,012,414 Cycles) (LB 5)

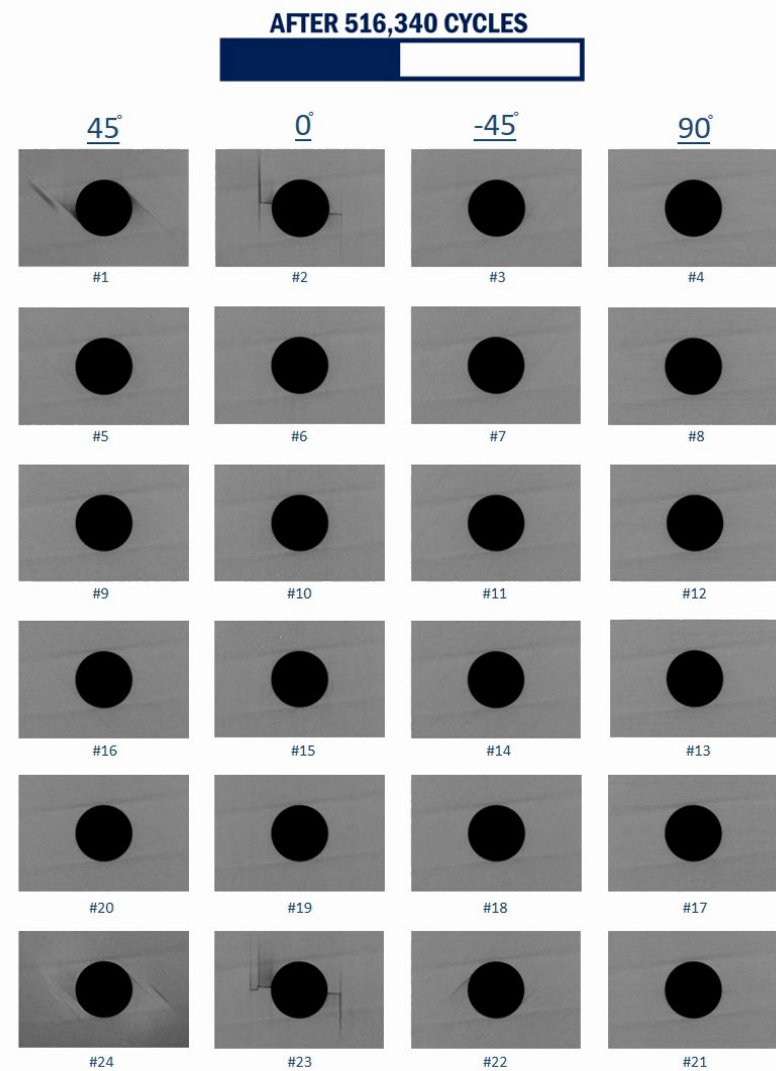
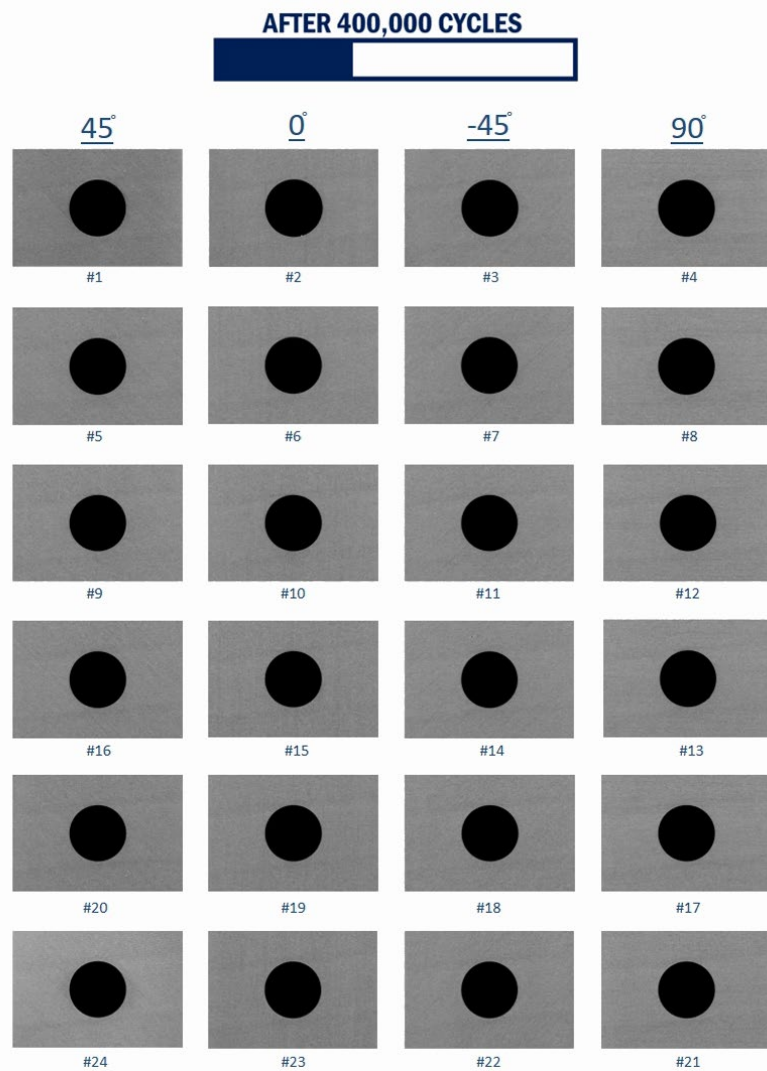


Figure B- 4. X-CT inspections of 24-Ply UNI-QI-OH Profile #6 (Specimen #26 at 400 K and 516,340 Cycles) (LB 1 and 2)

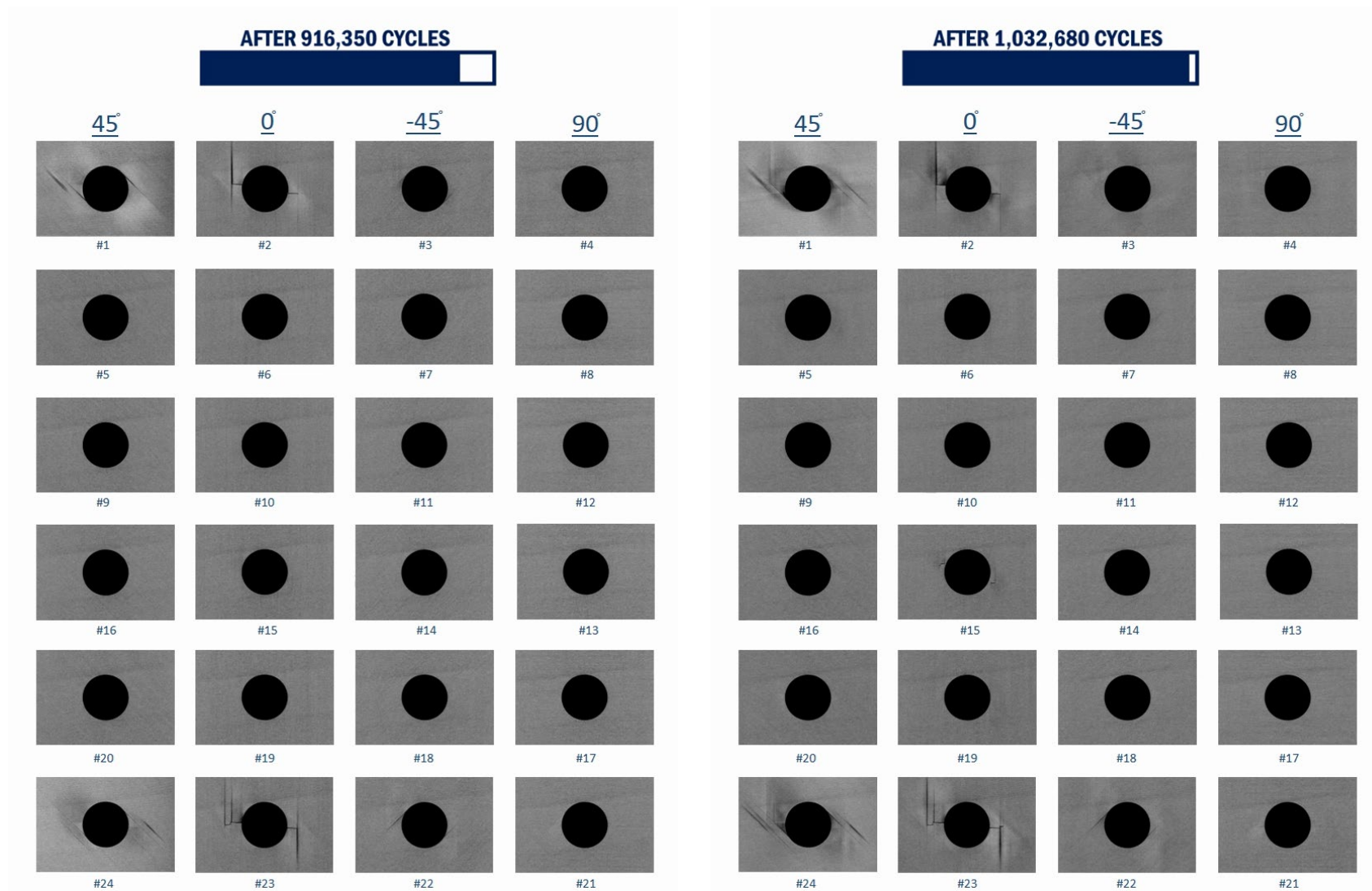


Figure B- 5. X-CT inspections of 24-Ply UNI-QI-OH Profile #6 (Specimen #26 at 916,350 and 1,032,680 Cycles) (LB 3 and 4)

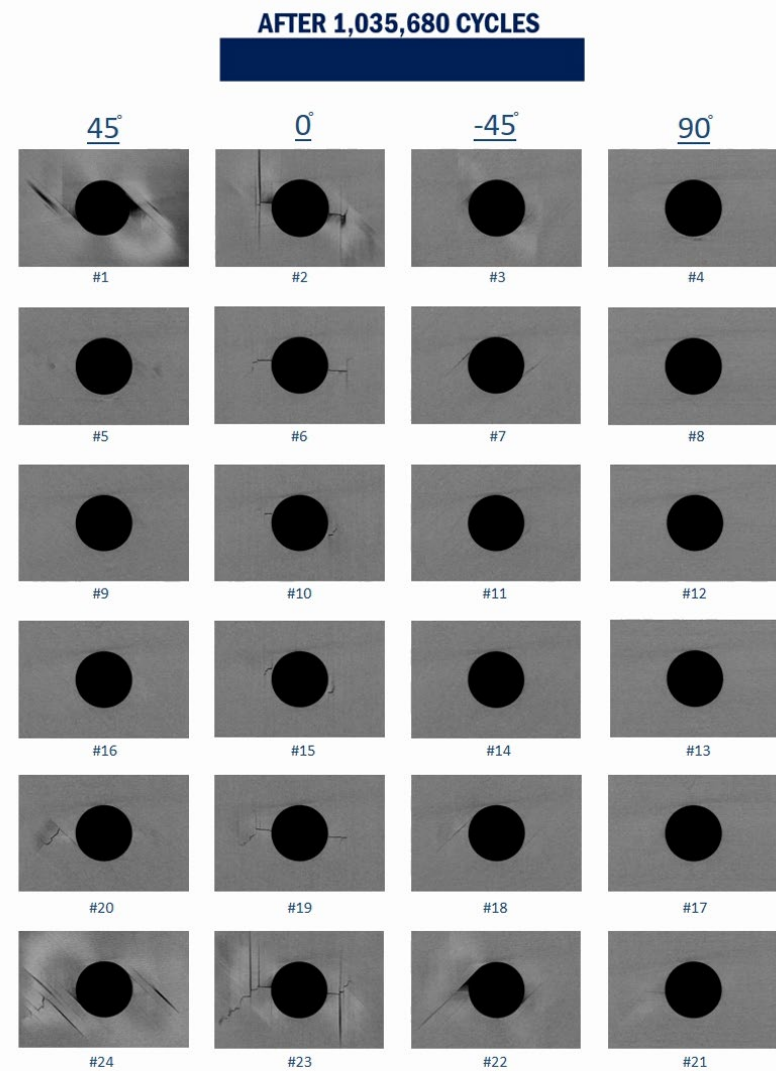
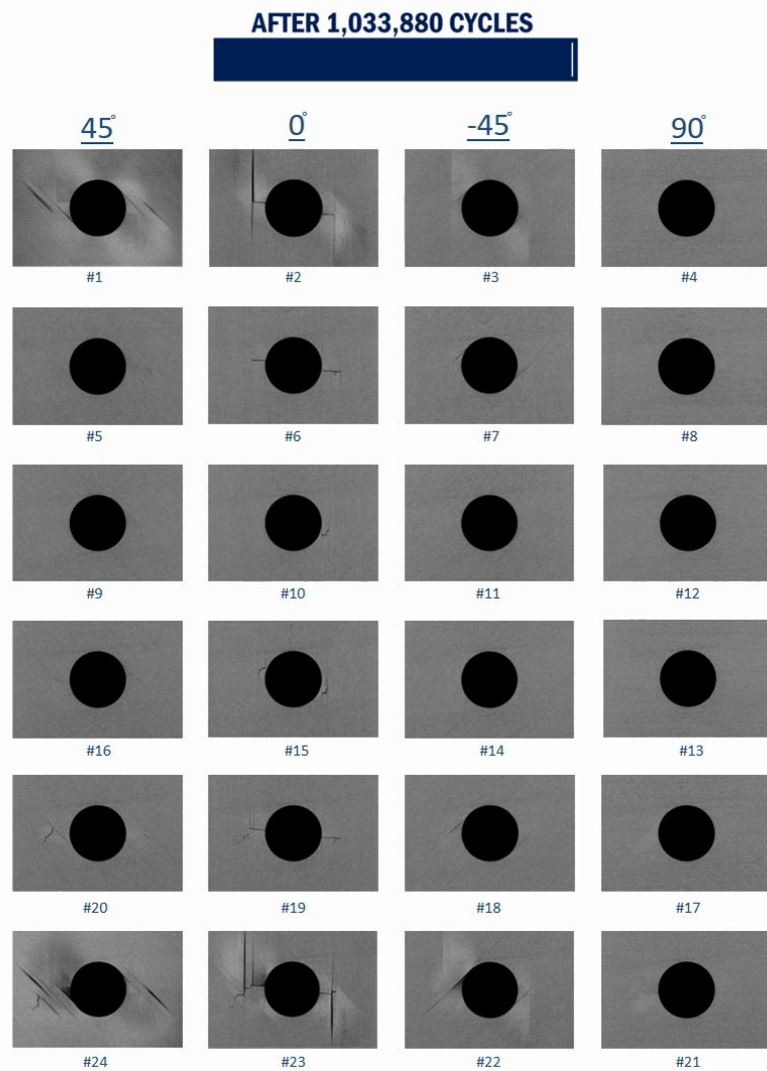


Figure B- 6. X-CT inspections of 24-Ply UNI-QI-OH Profile #6 (Specimen #26 at 1,033,880 and 1,035,680 Cycles) (LB 5)

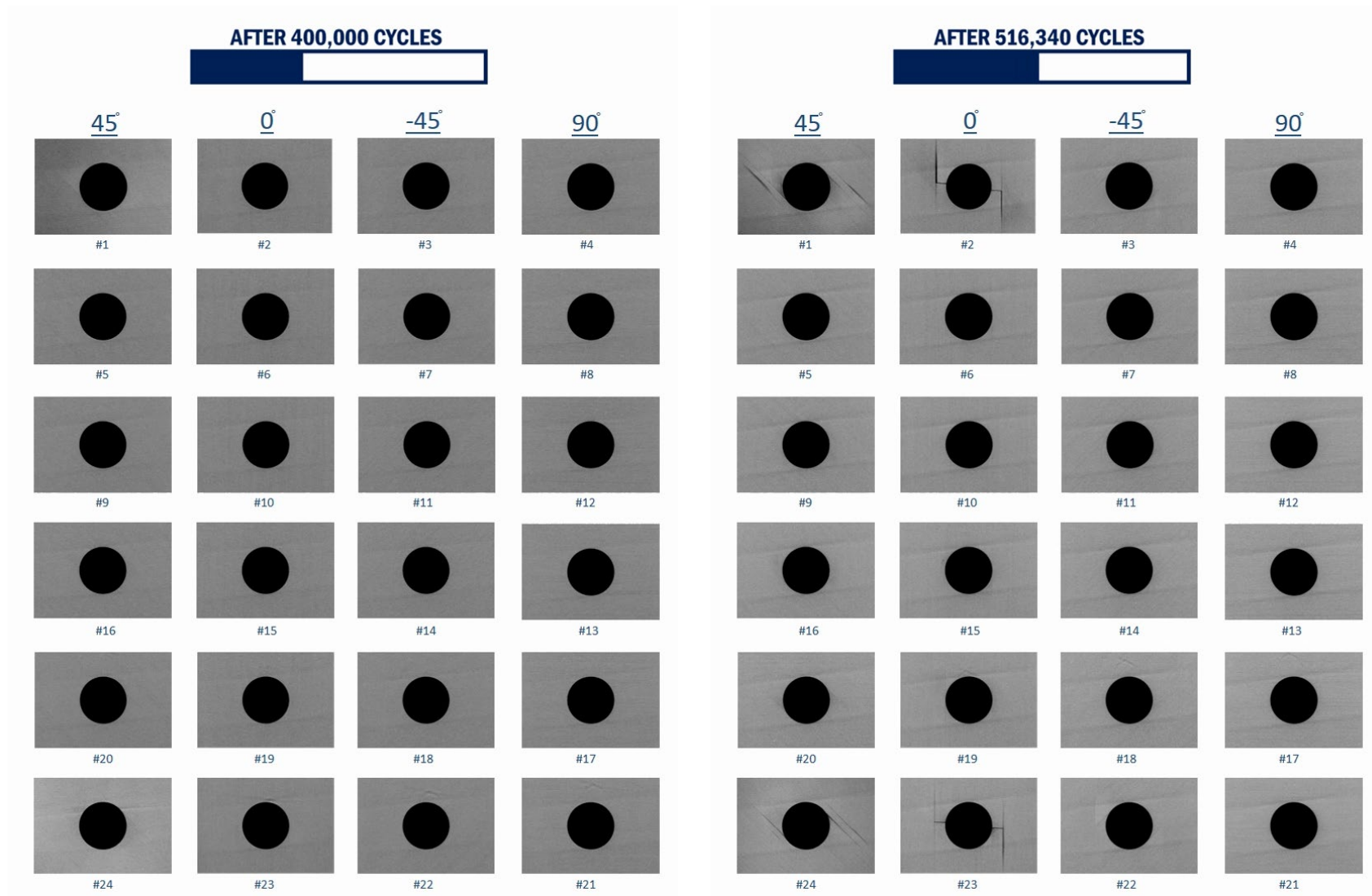


Figure B- 7. X-CT inspections of 24-Ply UNI-QI-OH Profile #3 (Specimen #24 at 400 K and 516,340 Cycles) (LB 1 and 2)

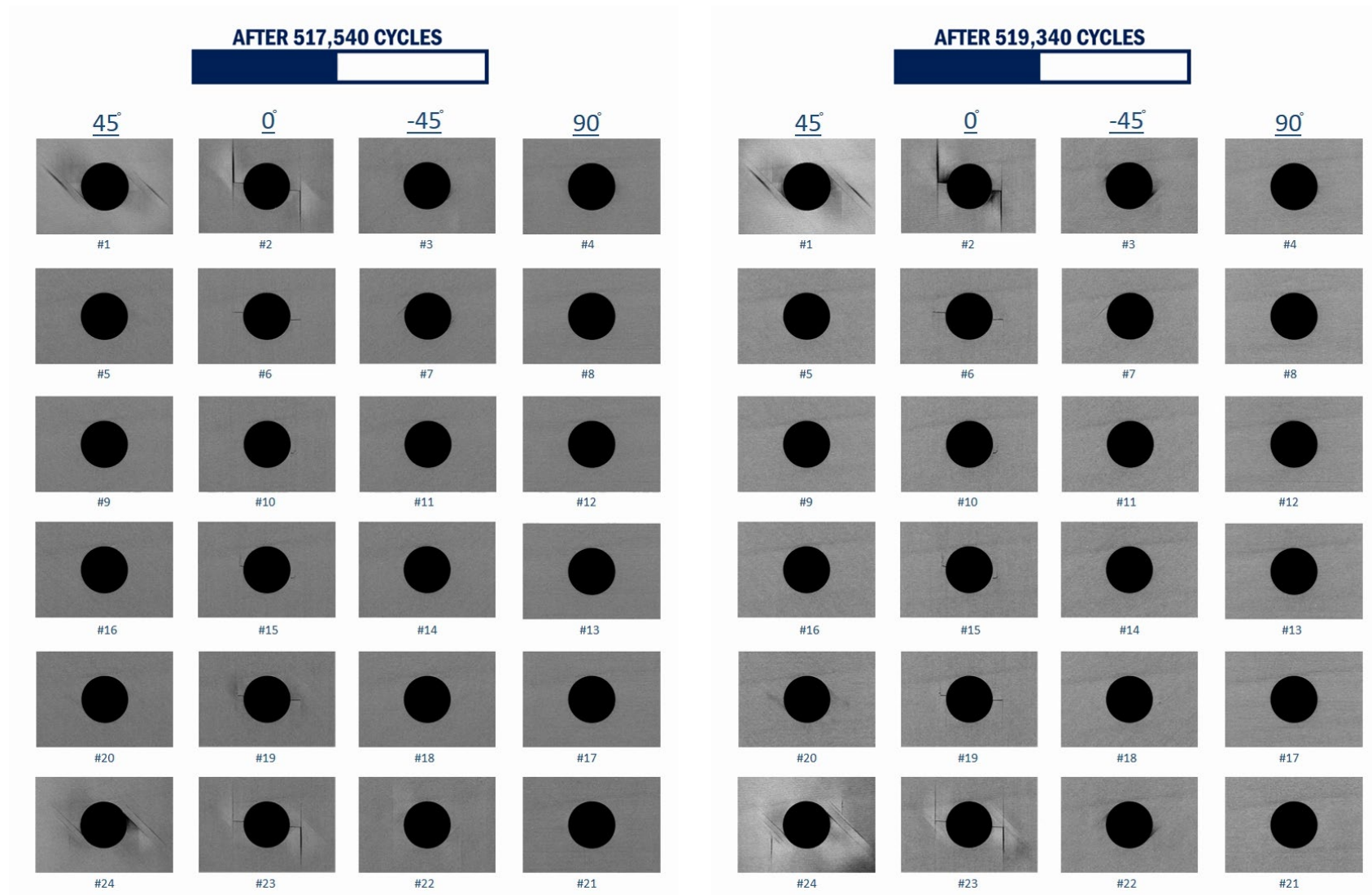


Figure B- 8. X-CT inspections of 24-Ply UNI-QI-OH Profile #3 (Specimen #24 at 517,540 and 519,340 Cycles) (LB 3)

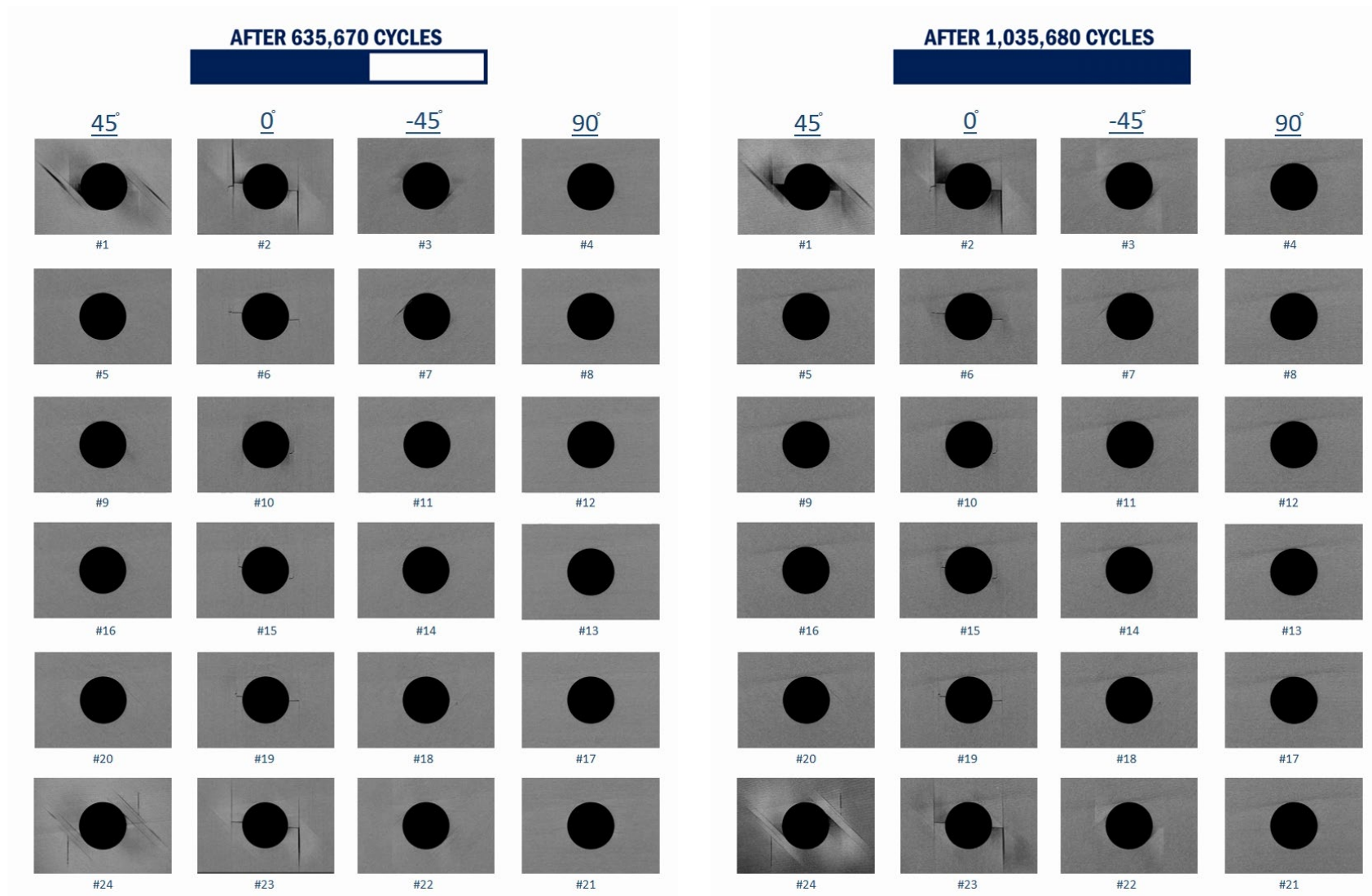


Figure B- 9. X-CT inspections of 24-Ply UNI-QI-OH Profile #3 (Specimen #24 at 635,670 and 1,035,680 Cycles) (LB 4 and 5)

C High-fidelity X-CT summary of constant and variable R-ratio spectra

Figure C- 1. X-CT inspections of 24-Ply UNI-QI-OH-P1 Specimen #7 (Spectrum R = 5 at 200 K and 220 K Cycles) (LB 1 and 2)	C-3
Figure C- 2. X-CT inspections of 24-Ply UNI-QI-OH-P1 Specimen #7 (Spectrum R = 5 at 222 K and 242 K Cycles) (LB 3 and 4)	C-4
Figure C- 3. X-CT inspections of 24-Ply UNI-QI-OH-P1 Specimen #7 (Spectrum R = 5 at 342 K and 442 K Cycles) (LB 5).....	C-5
Figure C- 4. X-CT inspections of 24-Ply UNI-QI-OH-P2 Specimen #27 (Spectrum R = -1 at 250 K and 275 K Cycles) (LB 1 and 2)	C-6
Figure C- 5. X-CT inspections of 24-Ply UNI-QI-OH-P2 Specimen #27 (Spectrum R = -1 at 276,500 and 277 K Cycles) (LB 3).....	C-7
Figure C- 6. X-CT inspections of 24-Ply UNI-QI-OH-P2 Specimen #27 (Spectrum R = -1 at 302 K and 552 K Cycles) (LB 4 and 5)	C-8
Figure C- 7. X-CT inspections of 24-Ply UNI-QI-OH-P2 Specimen #3 (Spectrum R = 5 and -1 at 200 K and 400 K Cycles) (LB 1 and 2)	C-9
Figure C- 8. X-CT inspections of 24-Ply UNI-QI-OH-P2 Specimen #3 (Spectrum R = 5 and -1 at 410 K and 415 K Cycles) (LB 3)	C-10
Figure C- 9. X-CT inspections of 24-Ply UNI-QI-OH-P2 Specimen #3 (Spectrum R = 5 and -1 at 420 K and 425 K Cycles) (LB 3 and 4)	C-11
Figure C- 10. X-CT inspections of 24-Ply UNI-QI-OH-P2 Specimen #8 (Spectrum R = -1 and 5 at 200 K and 400 K Cycles) (LB 1 and 2)	C-12
Figure C- 11. X-CT inspections of 24-Ply UNI-QI-OH-P2 Specimen #8 (Spectrum R = -1 and 5 at 410 K and 415 K Cycles) (LB 3).....	C-13
Figure C- 12. X-CT inspections of 24-Ply UNI-QI-OH-P2 Specimen #8 (Spectrum R = -1 and 5 at 420 K and 427,500 Cycles) (LB 4).....	C-14
Figure C- 13. X-CT inspections of 24-Ply UNI-QI-OH-P2 Specimen #8 (Spectrum R = -1 and 5 at 430 K and 432,500 Cycles) (LB 5).....	C-15

High-fidelity X-CT ply-level inspections conducted on fatigue coupons under constant and variable R-ratio spectrum profiles are presented here. The ply-level data presented were used to investigate damage mechanisms and damage progression in each ply for all CA fatigue scenarios. Four-dimensional (4D) X-CT video with all inspections can be furnished upon

request. Note that damage accumulation in the high-fidelity X-CT three-dimensional (3D) model along with the number of cycles (time) is identified as 4D.

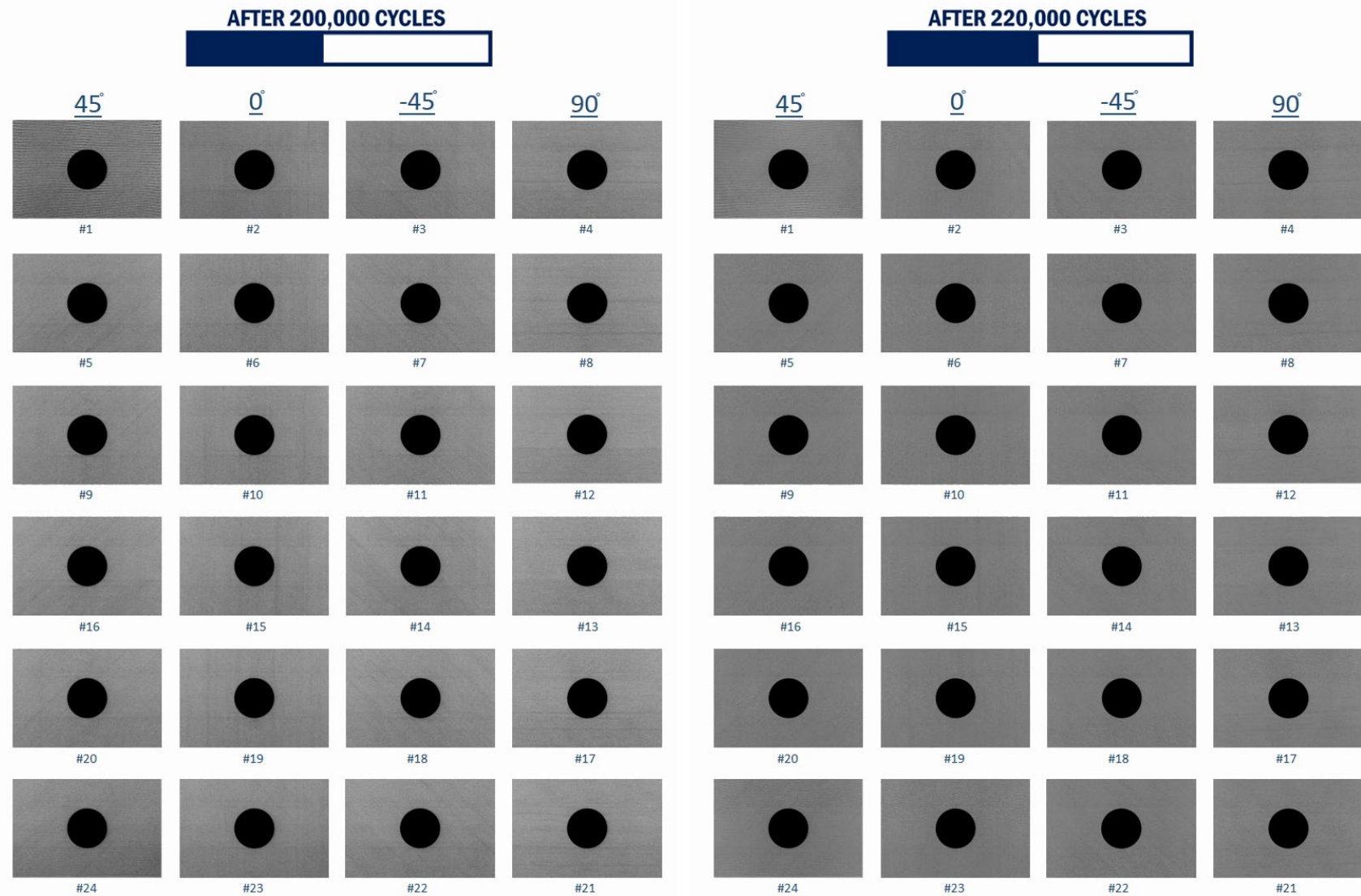


Figure C- 1. X-CT inspections of 24-Ply UNI-QI-OH-P1 Specimen #7 (Spectrum R = 5 at 200 K and 220 K Cycles) (LB 1 and 2)

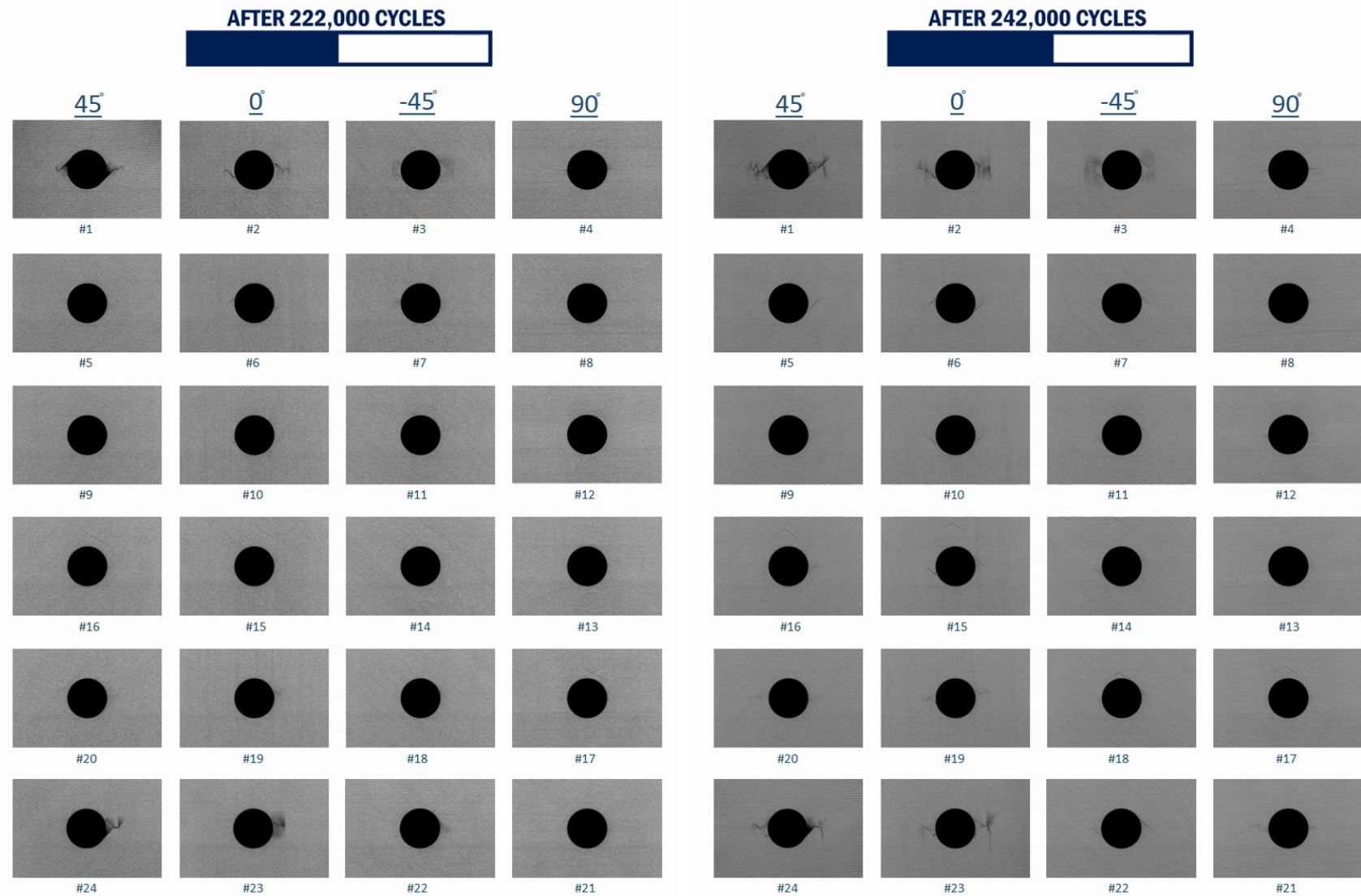


Figure C- 2. X-CT inspections of 24-Ply UNI-QI-OH-P1 Specimen #7 (Spectrum R = 5 at 222 K and 242 K Cycles) (LB 3 and 4)

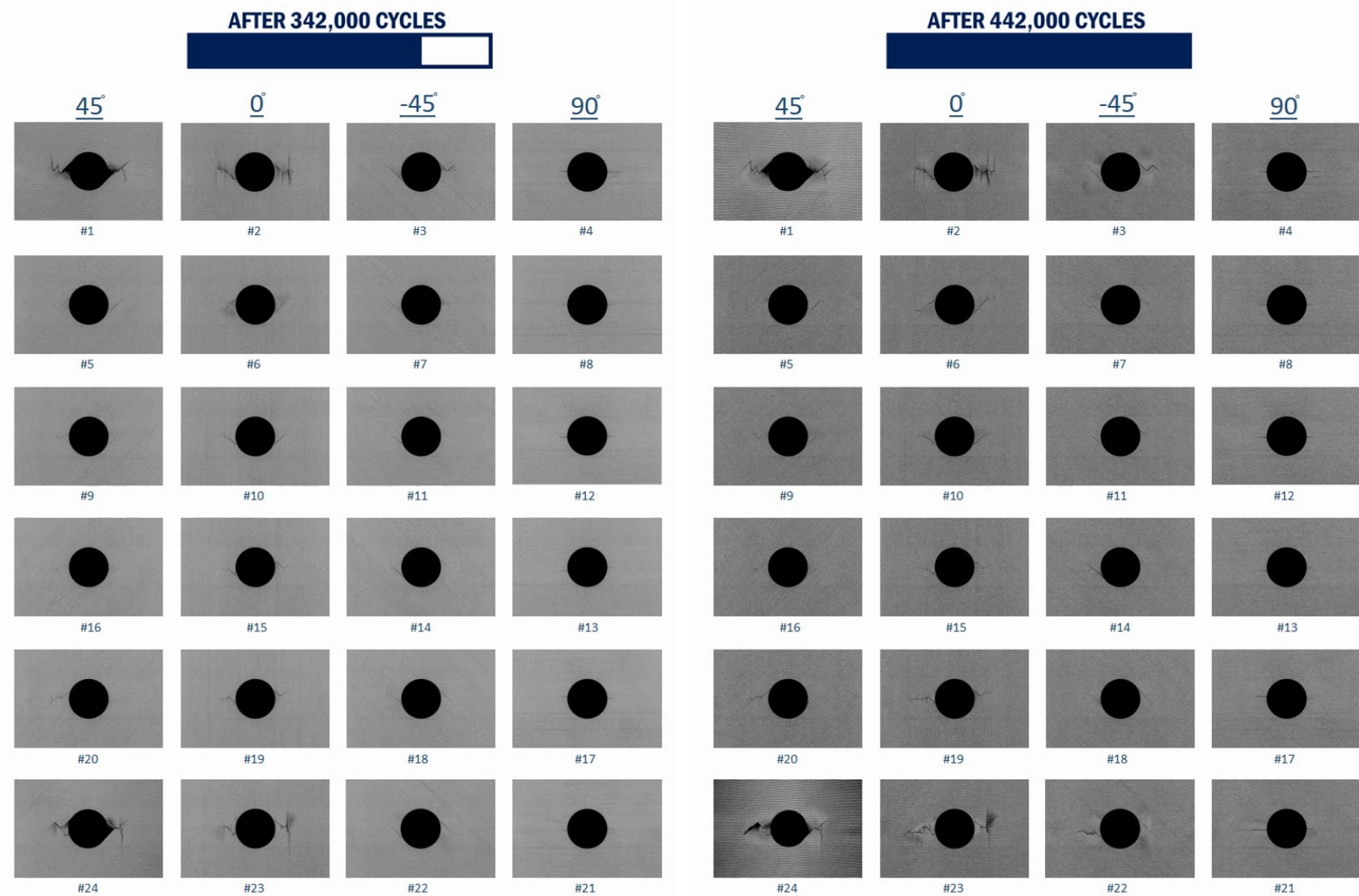


Figure C- 3. X-CT inspections of 24-Ply UNI-QI-OH-P1 Specimen #7 (Spectrum R = 5 at 342 K and 442 K Cycles) (LB 5)

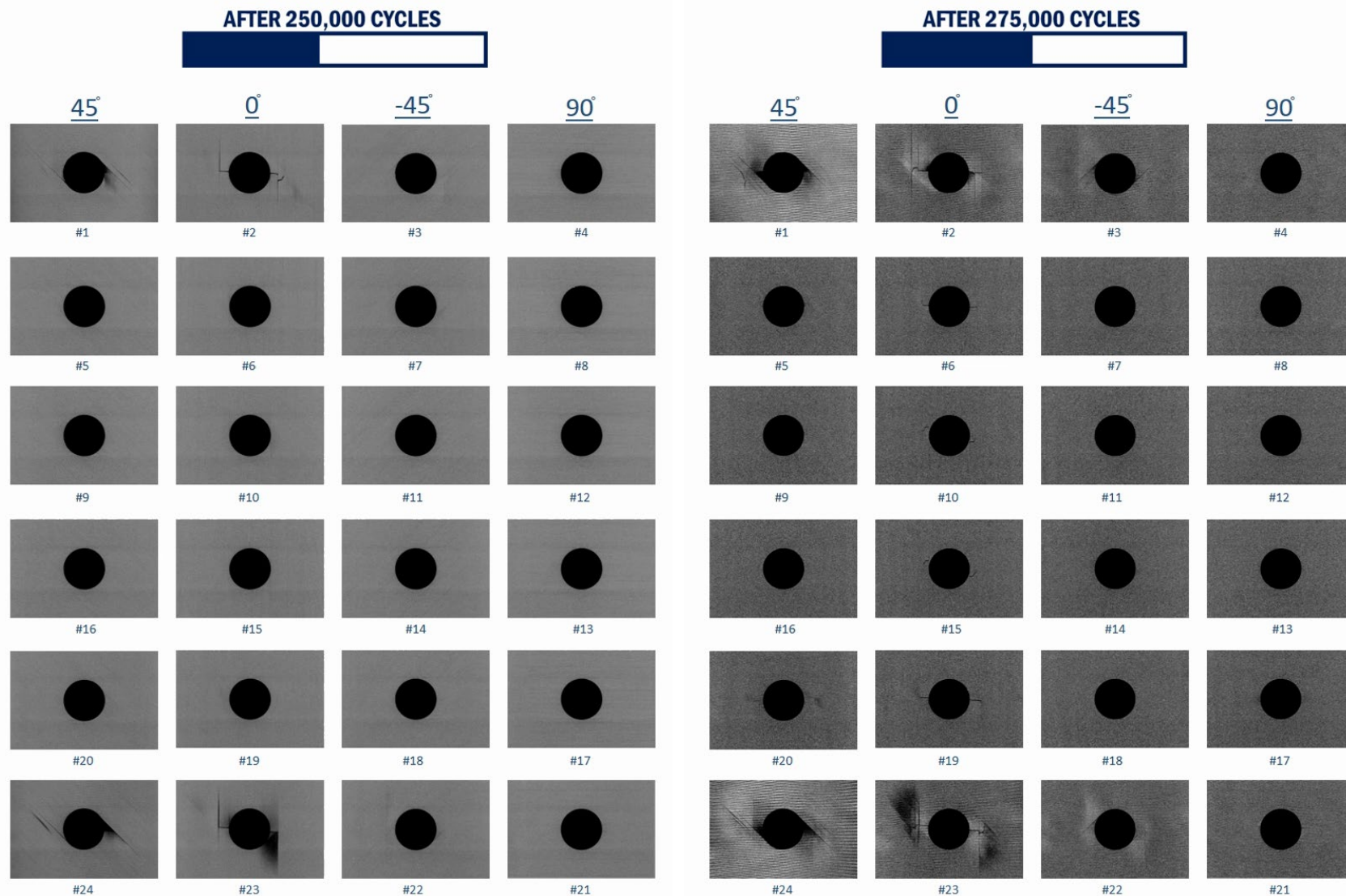


Figure C- 4. X-CT inspections of 24-Ply UNI-QI-OH-P2 Specimen #27 (Spectrum R = -1 at 250 K and 275 K Cycles) (LB 1 and 2)

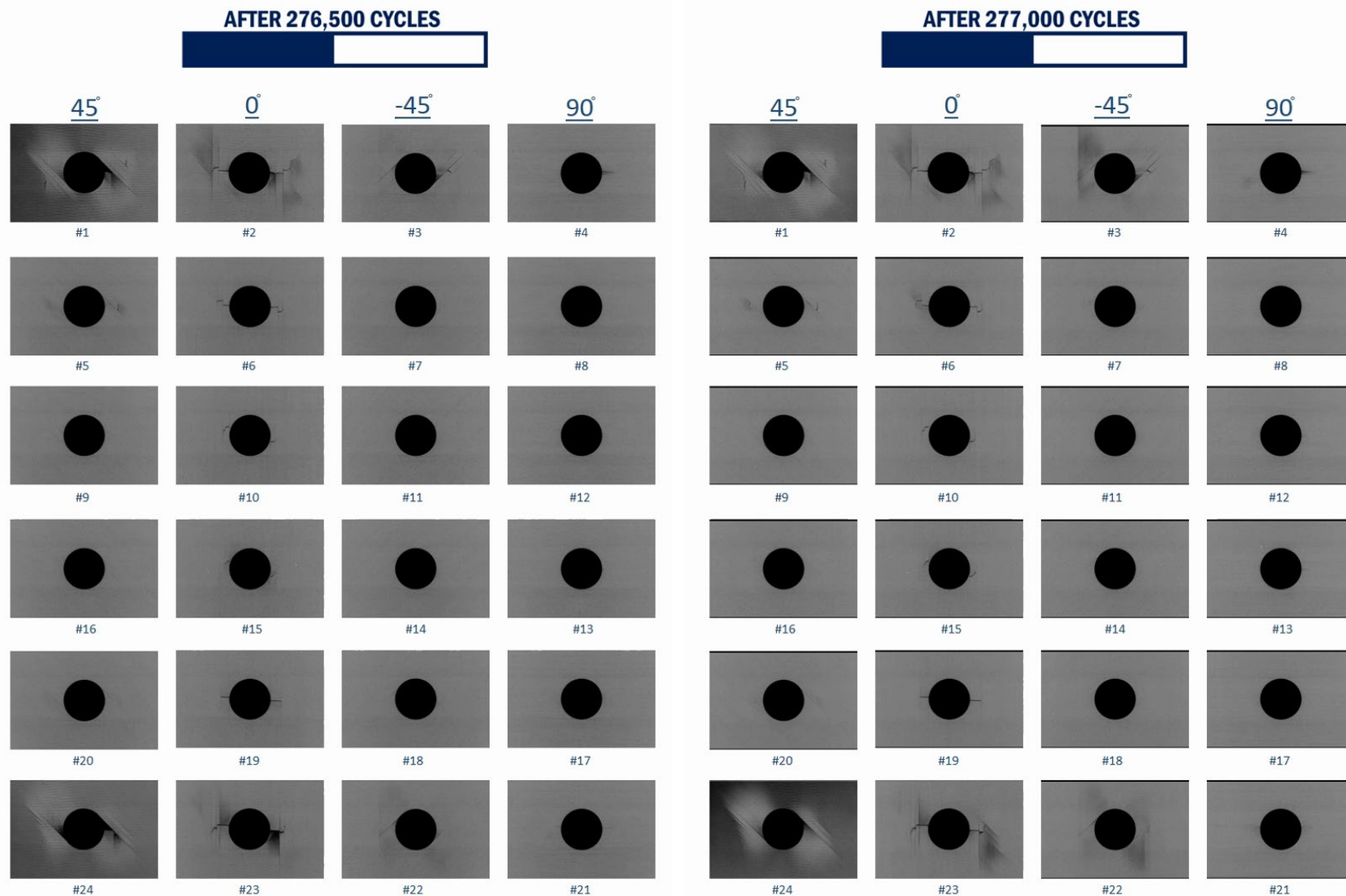


Figure C- 5. X-CT inspections of 24-Ply UNI-QI-OH-P2 Specimen #27 (Spectrum R = -1 at 276,500 and 277 K Cycles) (LB 3)

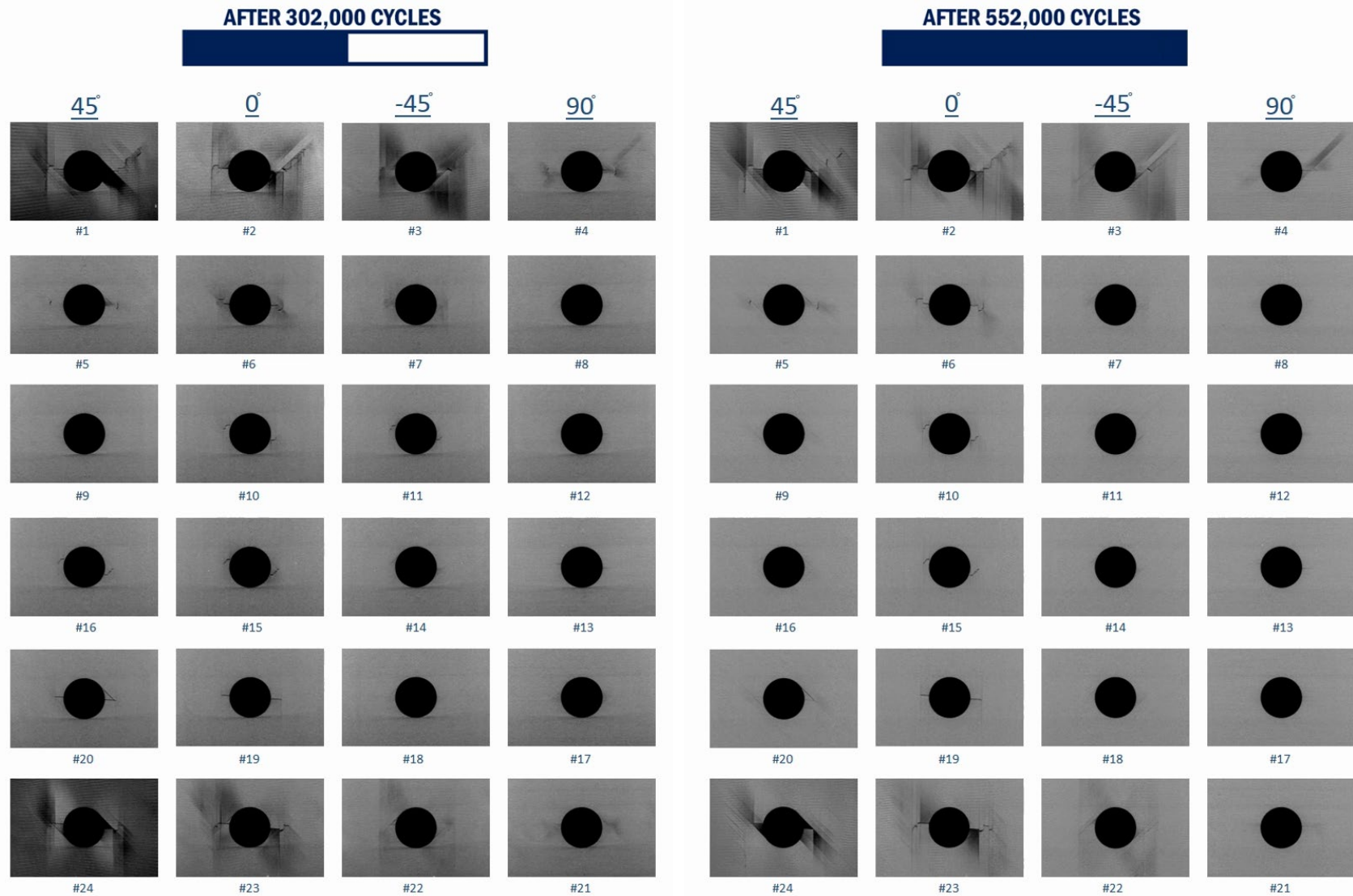


Figure C- 6. X-CT inspections of 24-Ply UNI-QI-OH-P2 Specimen #27 (Spectrum R = -1 at 302 K and 552 K Cycles) (LB 4 and 5)

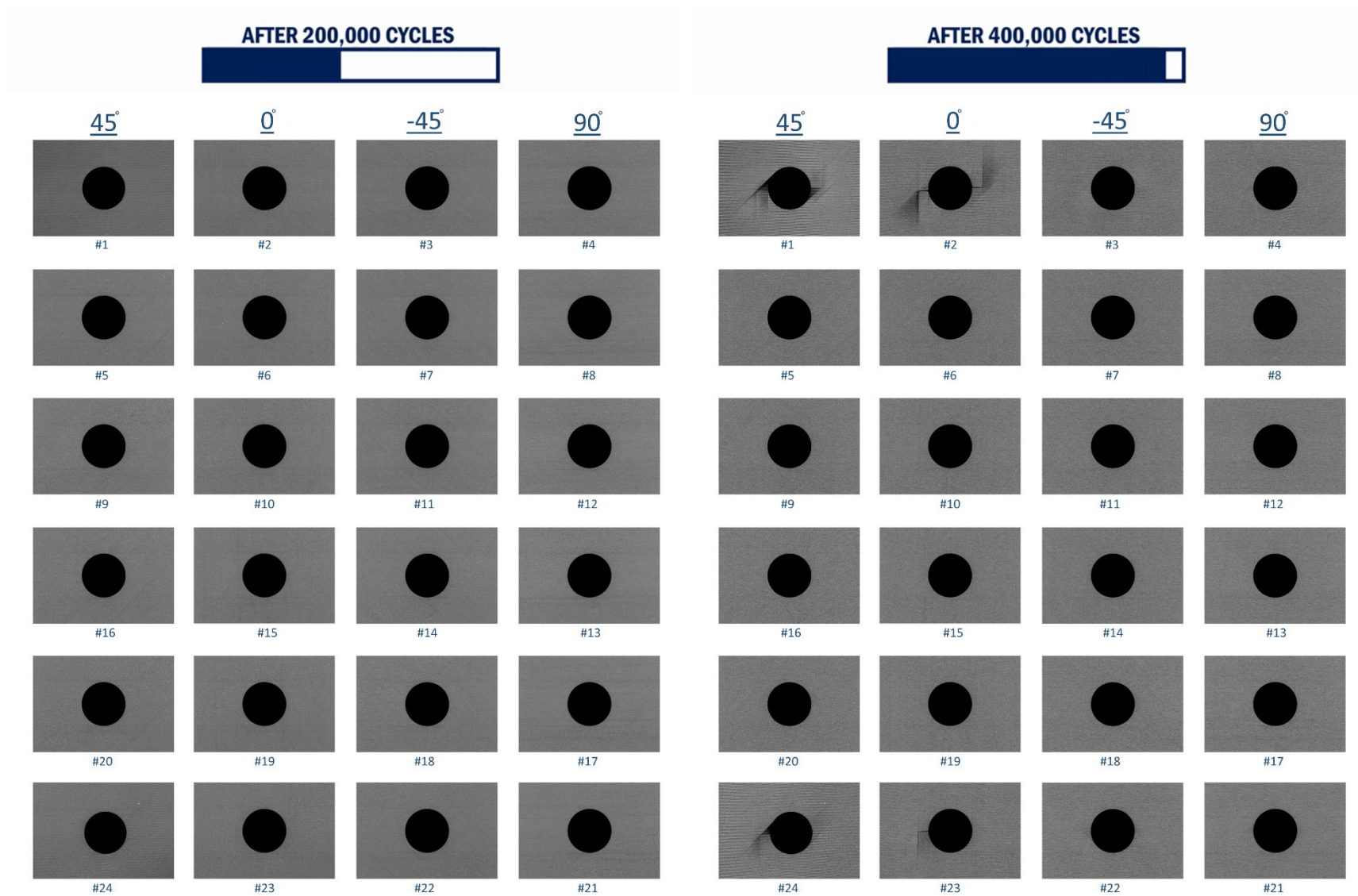


Figure C- 7. X-CT inspections of 24-Ply UNI-QI-OH-P2 Specimen #3 (Spectrum R = 5 and -1 at 200 K and 400 K Cycles) (LB 1 and 2)

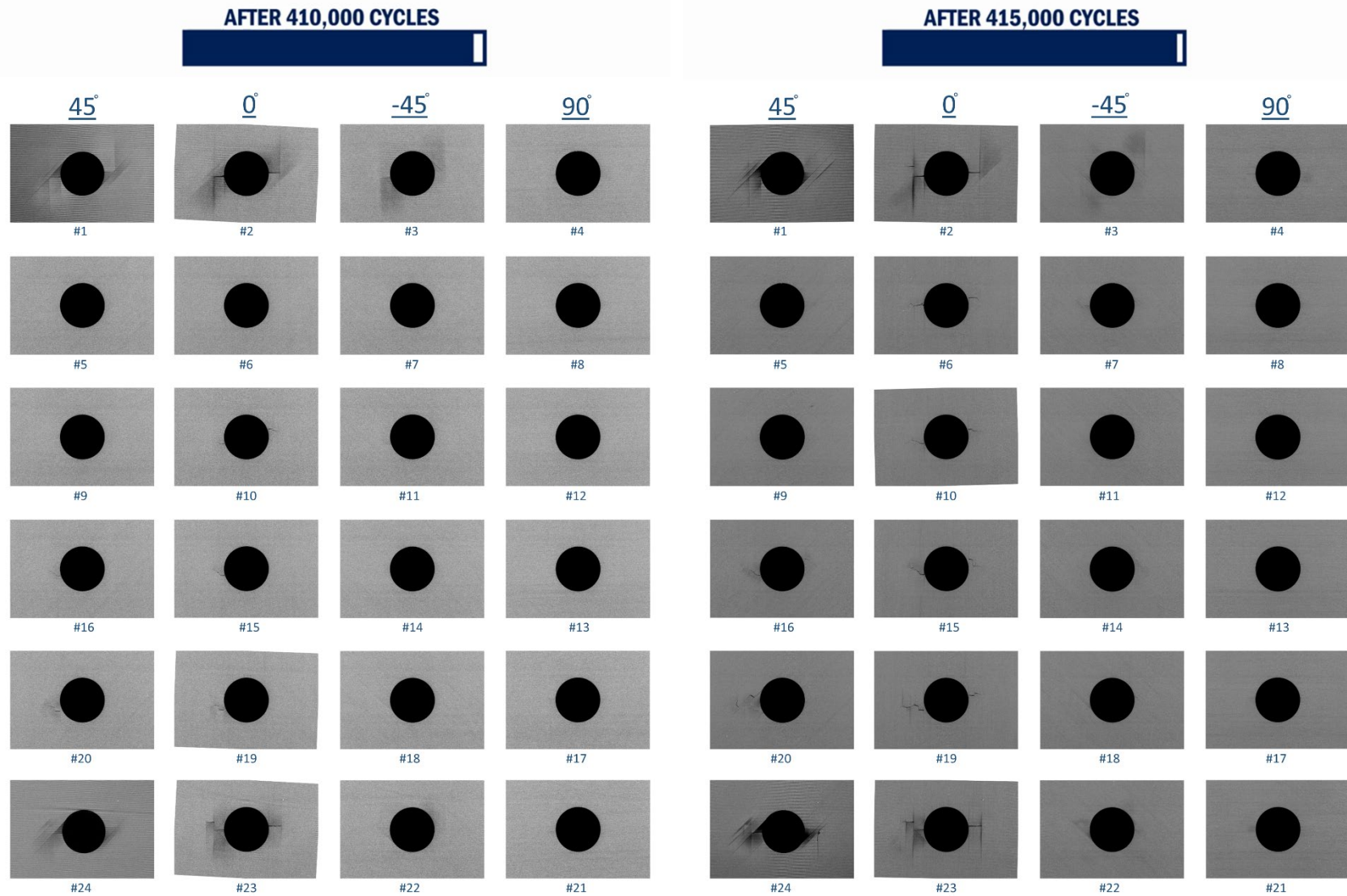


Figure C- 8. X-CT inspections of 24-Ply UNI-QI-OH-P2 Specimen #3 (Spectrum R = 5 and -1 at 410 K and 415 K Cycles) (LB 3)

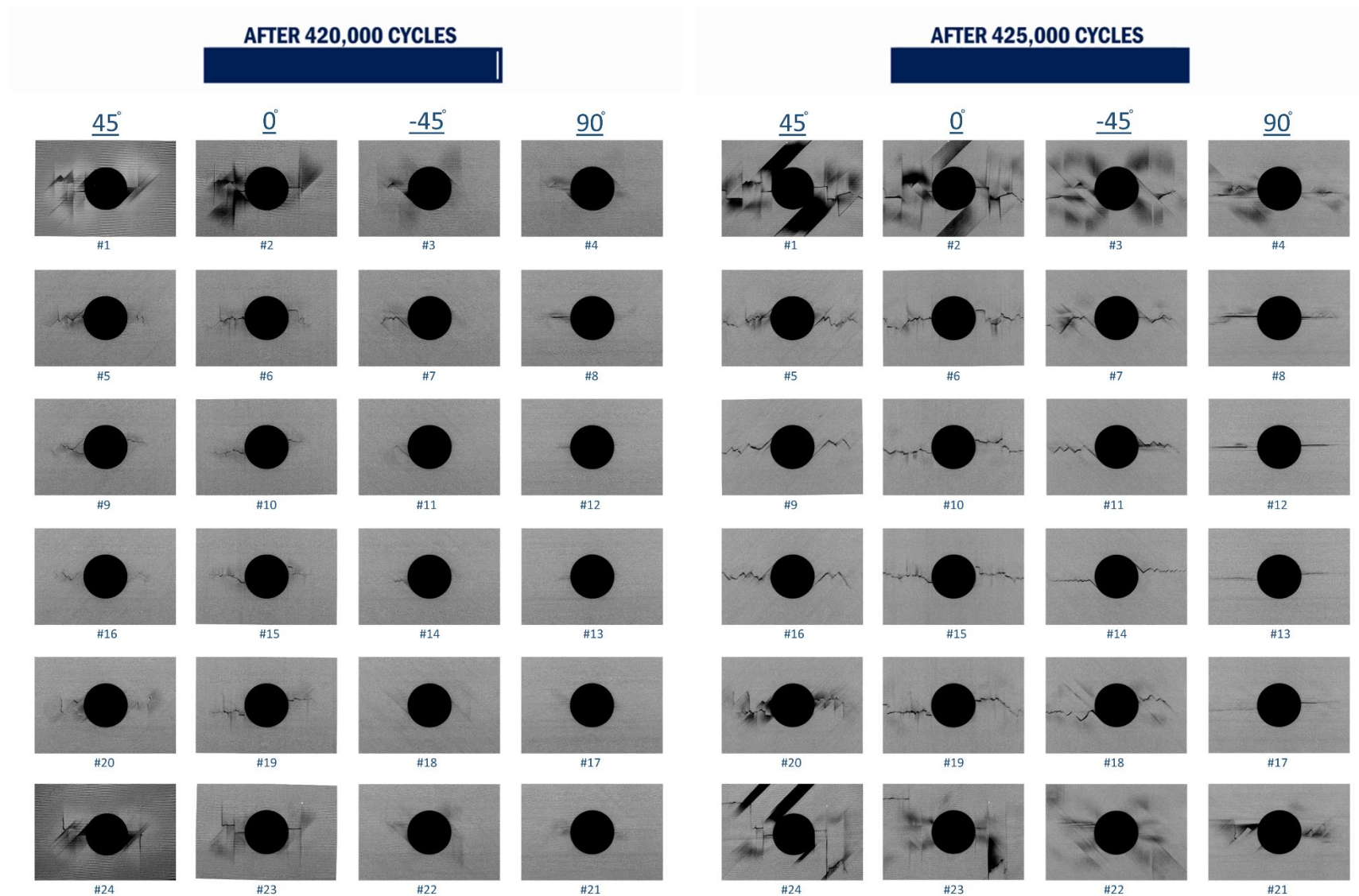


Figure C- 9. X-CT inspections of 24-Ply UNI-QI-OH-P2 Specimen #3 (Spectrum R = 5 and -1 at 420 K and 425 K Cycles) (LB 3 and 4)

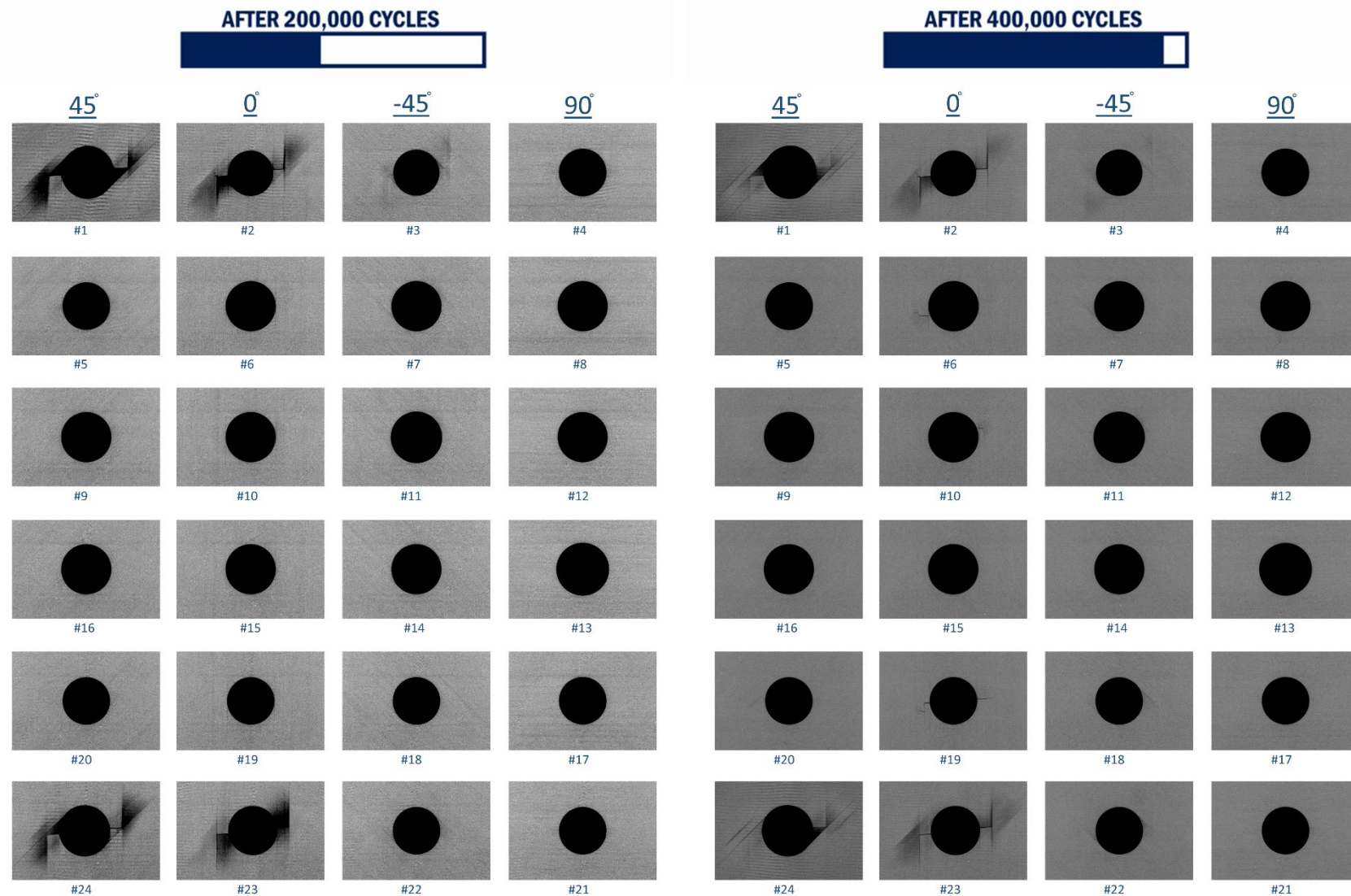


Figure C- 10. X-CT inspections of 24-Ply UNI-QI-OH-P2 Specimen #8 (Spectrum R = -1 and 5 at 200 K and 400 K Cycles) (LB 1 and 2)

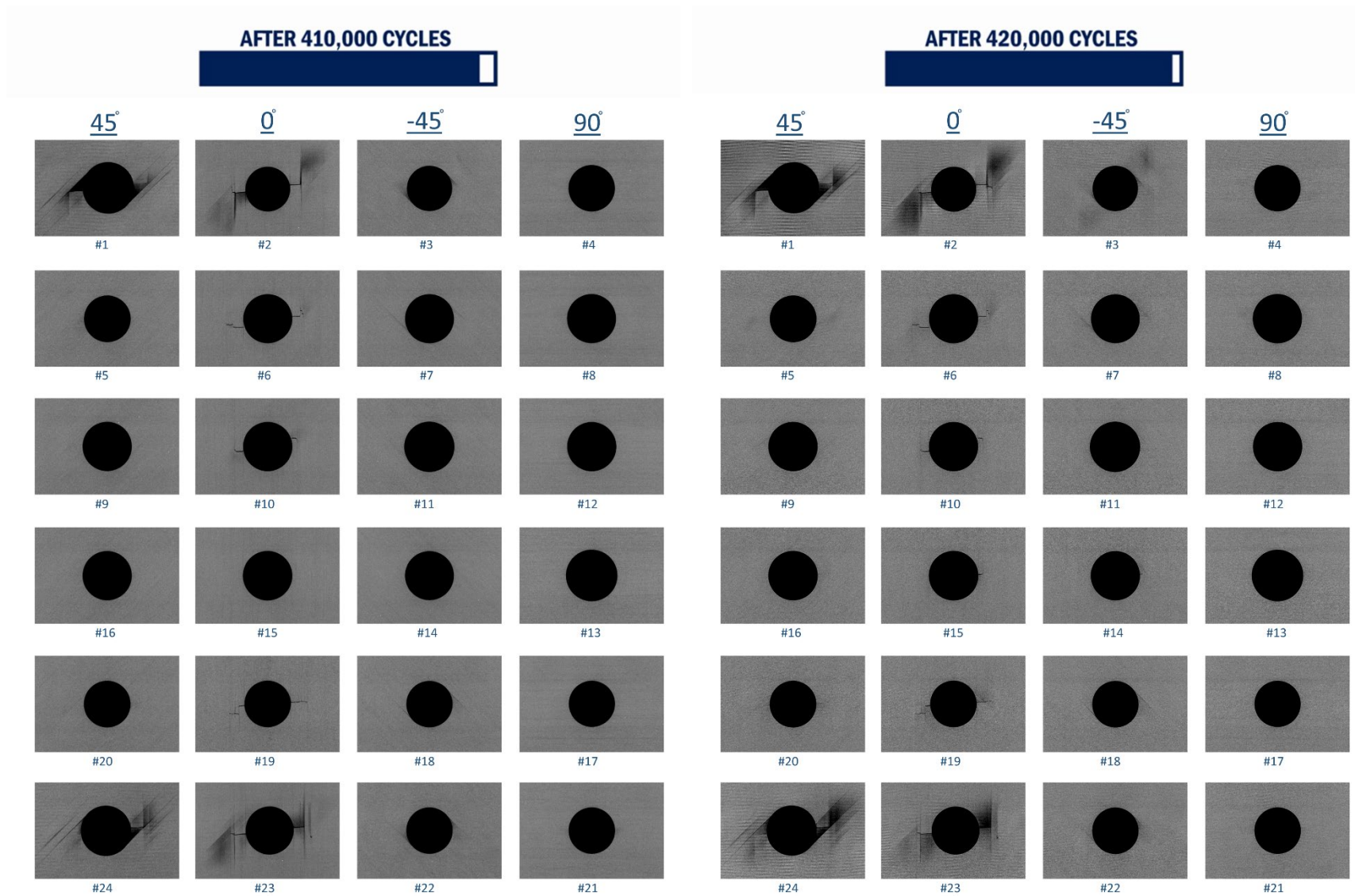


Figure C- 11. X-CT inspections of 24-Ply UNI-QI-OH-P2 Specimen #8 (Spectrum R = -1 and 5 at 410 K and 415 K Cycles) (LB 3)

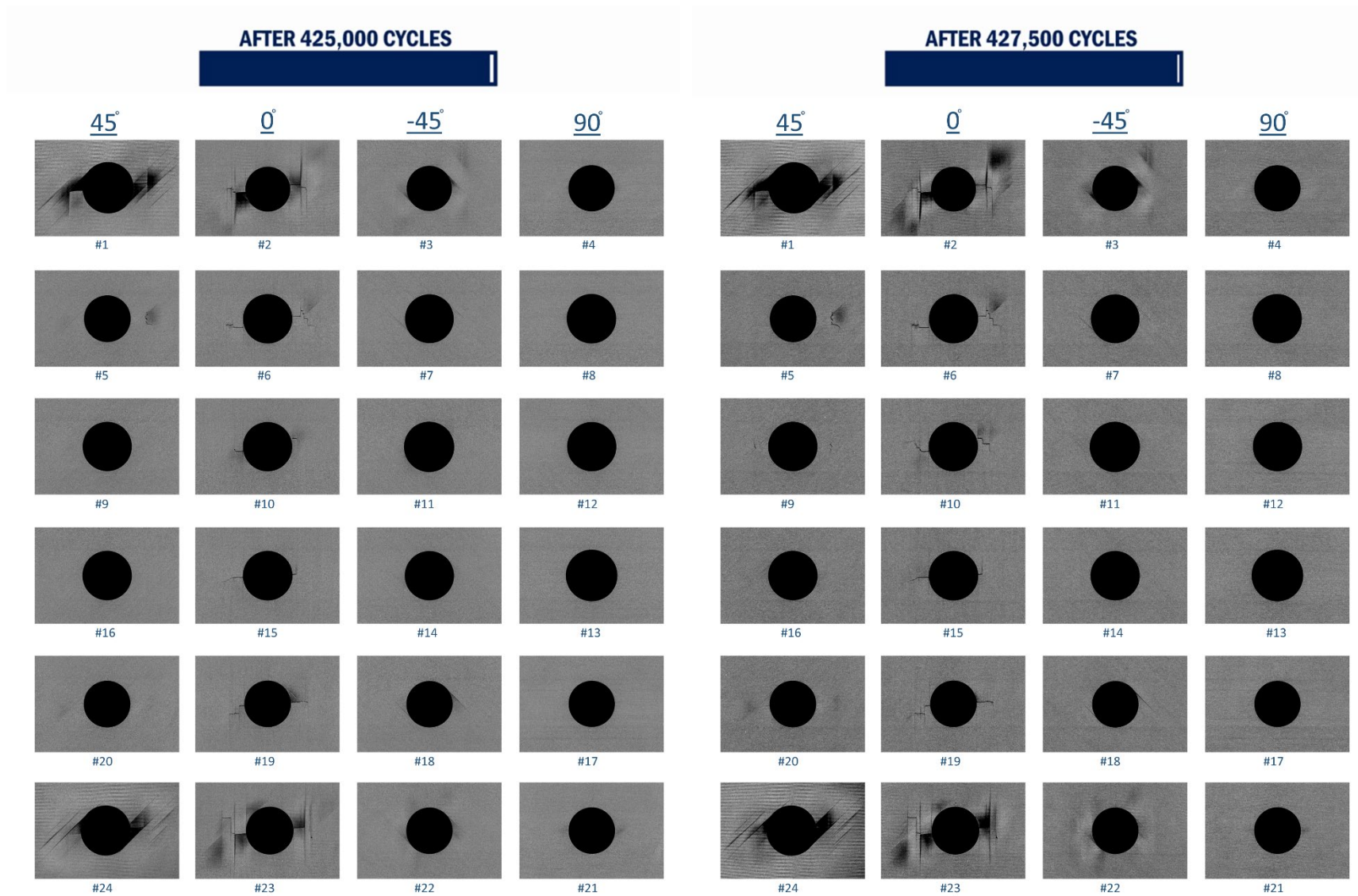


Figure C- 12. X-CT inspections of 24-Ply UNI-QI-OH-P2 Specimen #8 (Spectrum R = -1 and 5 at 420 K and 427,500 Cycles) (LB 4)

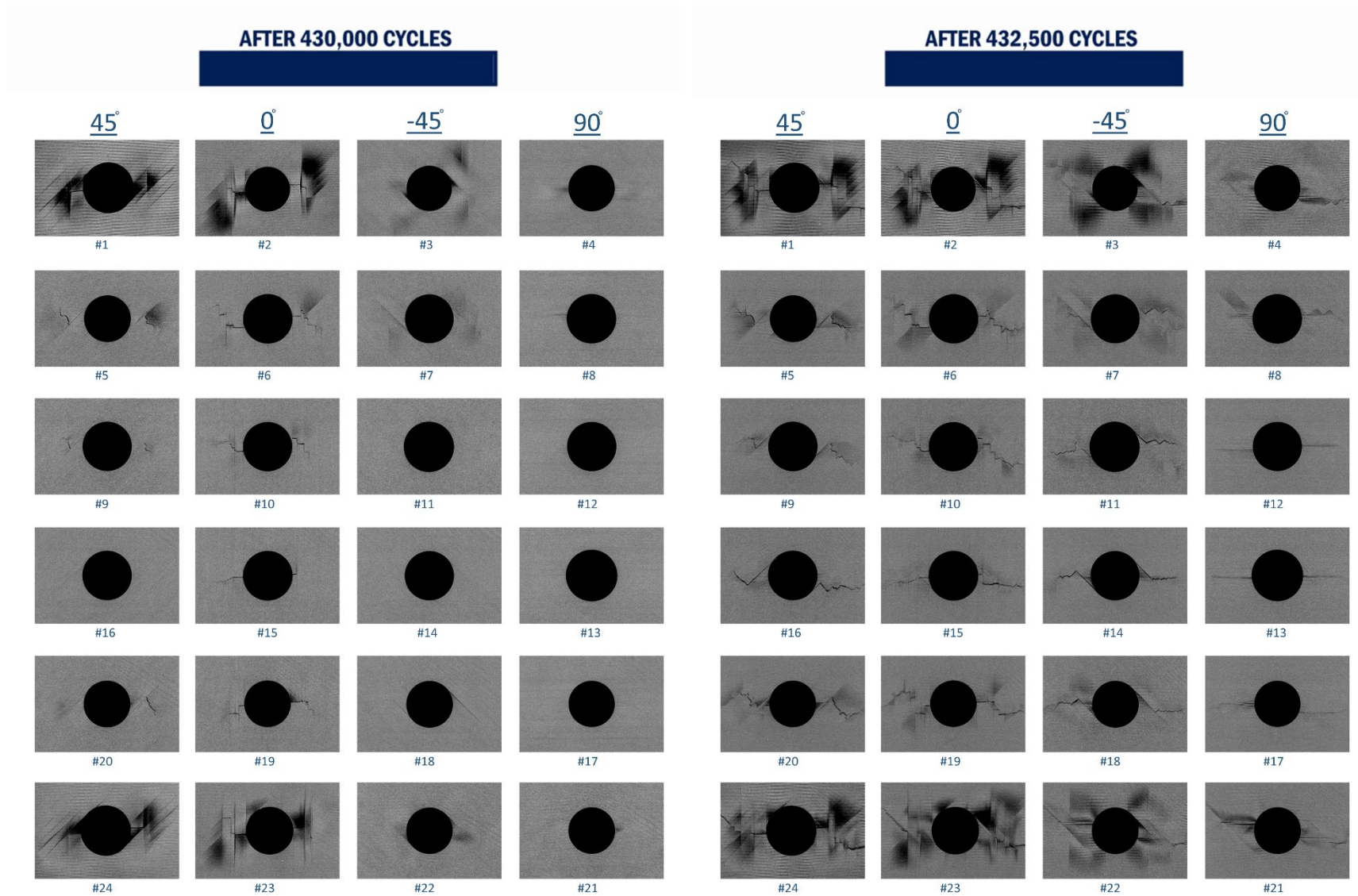


Figure C- 13. X-CT inspections of 24-Ply UNI-QI-OH-P2 Specimen #8 (Spectrum R = -1 and 5 at 430 K and 432,500 Cycles) (LB 5)